UNIVERSITÀ DEGLI STUDI
DI GENOVA

iit GRAPHENE
ISTITUTO ITALIANO
DI TECNOLOGIA

Doctorate school: Scienze e Tecnologie della Chimica e dei Materiali

Curriculum: Nanochemistry

XXXIV cycle

PhD Thesis

Design and characterization of doped Lithium Rich Layered Oxides for Lithium Ion Battery

Supervisor:
Dr. Vittorio Pellegrini
Dr. Liberato Manna
Prof. Daniele Marrè

Ph.D. Student:
Arcangelo Celeste

INDEX

ABSTRACT

Lithium-Rich Layered Oxides (LRLO) are opening new frontiers for high-capacity/high-voltage positive electrodes in Li-ion batteries to meet the challenges of green and safe transportation as well as cheap and sustainable stationary energy storage from renewable sources. LRLO exploit the extra-lithiation provided by the $Li_{1.2}TM_{0.8}O_2$ stoichiometries to disclose specific capacities beyond 200-250 $mAhg^{-1}$ and working potentials in the 3.4-3.8V vs Li. In my thesis, I demonstrated a novel doping strategy by the substitution of cobalt in the transition metal layer of the lattice with aluminum and lithium, resulting in new optimized layered materials, *i.e.* $Li_{1.2+x}Mn_{0.54}Ni_{0.13}Co_{0.13-x-y}Al_yO_2$, with outstanding electrochemical performance in full Li-ion batteries, improved environmental benignity and reduced manufacturing costs compared to the state-of-the-art. Furthermore, the last step deals the application of over-lithiation to demonstrate experimentally a Co-free over-lithiated LRLO material, *i.e.* $Li_{1.25}Mn_{0.625}Ni_{0.125}O_2$. After that, my research focused on a novel approach to investigate the structural complexity of pristine materials, involving the use of supercells, *i.e.* unit cells larger than the conventional ones, and FAULTS software, to take into account the staking faults defects. A combination of *ex situ* techniques has been used as a tool to understand the structural evolution of $Li_{1.28}Mn_{0.54}Ni_{0.13}Co_{0.02}Al_{0.03}O_2$. This part of the research identified that significant changes occurred during electrochemical cycling, showed the irreversible changes in the cell parameters and the presence of a new phase. Finally, innovative non-aqueous electrolytes for Li-ion batteries with superior safety features were investigated. Three ionic liquid, $Pyr_{1,n}TFSI$ with n=4,5,8, have been used as addditive to improve liquid electrolytes. These electrolyte formulations have been analyzed by comparing chemical-physical properties and electrochemical stability.

1 INTRODUCTION

1.1 LITHIUM-ION BATTERIES

An electrochemical cell is a device that can convert chemical energy in electrical energy and nowdays, in general, a battery is practically the synonym of electrochemical cell[1]. Batteries can be divided in: 1) primary batteries, *i.e.* batteries can be used and disposed, and 2) secondary batteries, batteries can be recharged and reused[2]. In particular, Lithium-ion Batteries (LIBs) belong to the second category of batteries.

LIBs are compact and light devices with an operation voltage of 3.8-4V and, today, with a specific energy around 200 $WhKg^{-1}$ [1,3]. Typically, Lithium-ion battery consists of three main components: 1) a positive electrode (cathode), 2) a negative electrode (anode) and 3) a membrane immersed in an electrolyte solution[4–6]. A pictorial representation of the components is shown in figure 1.1.

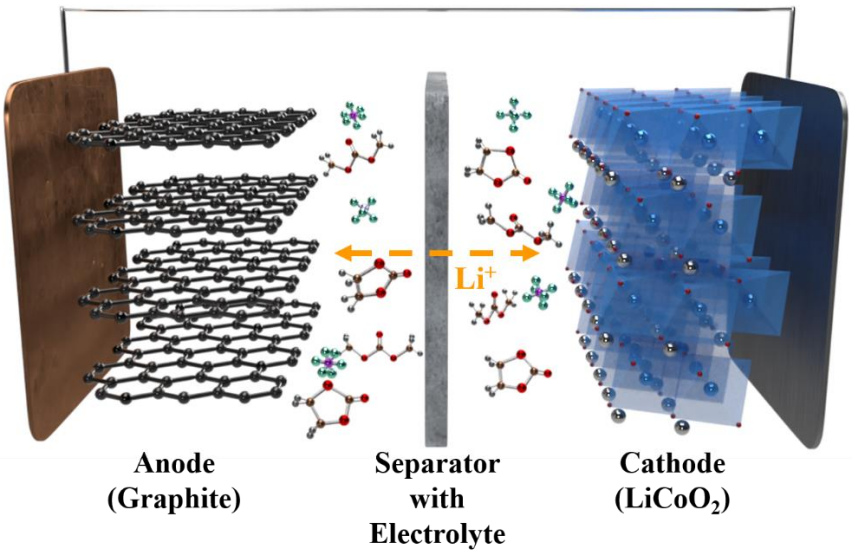

Figure 1.1: Main components of a typical lithium-ion battery.

The two electrodes are separated by the membrane, this allows to prevent electrical contacts between them while permitting the diffusion of Li ions during the charge and the discharge[7,8]. In a commercial LIBs, the active component of the cathode is a lithium metal oxide, in particular $LiCoO_2$[9], the active component of the anode is graphite[10] and the electrolyte is a solution of a lithium salt (e.g. $LiPF_6$) in a mixed organic solvent (e.g. ethylene carbonate-dimethyl carbonate,

EC-DMC)[11]. During the discharge, Li ions flow from the graphite anode to the cathode through the electrolyte solution. At the same time, electrons flow from the anode to the cathode through the external circuit, therefore the anode is oxidized while the metals in the cathode are reduced. During the charge, the energy is supplied through the external circuit to obtain the reverse reaction, where the Li ions come from the cathode to the anode. The electrode materials are able to reversibly incorporate the Li ions in the lattice host depending on the charge or discharge processes. The redox reactions involved can be describe as:

$$\text{Cathode: } LiCoO_2 \leftrightarrows Li_{(1-x)}CoO_2 + xLi^+ + xe^-$$

$$\text{Anode: } 6C + xLi^+ + xe^- \leftrightarrows Li_xC_6$$

LIBs can be used for very different applications and, today, represent the most important energy storage system available in the market. For these reasons, the development of more performing LIBs is a critical point to enable/support additional applications (stationary, automotive etc…), in particular with regard to energy density delivered, time life and safety.

Necessarily, the improvement of LIBs is related to the development of new materials and electrolytes or at least to their physical-chemical modifications. Regarding the anode, as explained before, graphite is the most used negative materials. Its specific capacity is 372 mAg^{-1} with a intercalation mechanism[12]. At the first lithium intercalation, a solid electrolyte interface (SEI) film is formed on the surface of the graphite due to the decomposition of the organic solvent at low negative potential[13]. The SEI allows Li^+ migration and contemporary prevent further decomposition of the solvent molecules. Novel negative materials have been developed in the last years. $Li_4Ti_5O_{12}$ (LTO) shows low reactivity with the electrolyte and better rate capability compared to graphite[6]. In fact, LTO has a high operation voltage that prevents lithium plating and SEI formation. Moreover, some elements can alloy with lithium ions, reaching very high specific capacities. For example, Si can be used as a negative electrode and is able to accommodate Li^+ with a theoretical specific capacity around 4000 $mAhg^{-1}$ [14,15]. Nevertheless, silicon suffers from a large volume change, leading to the pulverization of the electrode and poor electrochemical stability. Recently, Si nanoparticles wrapped by few-layer graphene flakes have been used to mitigate this drawback, showing very stable performance in cells[16].

On the positive component, several cathode materials have been proposed with different stoichiometries and structures. A more detailed discussion is reported in section 1.2. The cathode material is the key component for improving of the energy density of LIBs and further efforts are needed to develop new materials.

1.2 POSITIVE ELECTRODE MATERIALS

Fundamental characteristics for a cathode material are[17,18]:

- reversibility of electrochemical process;
- high cycle efficiency:
- no phase transition;
- electrochemical and thermal stability.

Since the commercialization of $LiCoO_2$, as a cathode material, by Sony[19], research on other types of cathode materials was pursued with different stoichiometry and structure. In the following sections, the most studied and popular cathode materials are described.

1.2.1 Layered structure compounds

The most important cathode materials are lithium metal-layered oxide ($LiMO_2$)[20–23]. In particular, $LiCoO_2$ (LCO) has been the most widely-used cathode material in commercialized LIBs because of its easy preparation and stable electrochemical performance[24–26]. LCO have an O3-type layered structure, which can be described in the R-3m space group[27]. Figure 1.2 shows the structure of $LiCoO_2$. The oxygen anions have a closed–packed arrangement in ABCABC stacking sequence. Lithium and transition metals form Li layers and transition metal layers stacked alternatively. An O3 structure is represented with a unit cell that has three transition metal oxide (CoO_2) slabs and the transition metals occupy the octahedral sites. In between the MO_2 slabs, Li atoms occupy the octahedral sites.

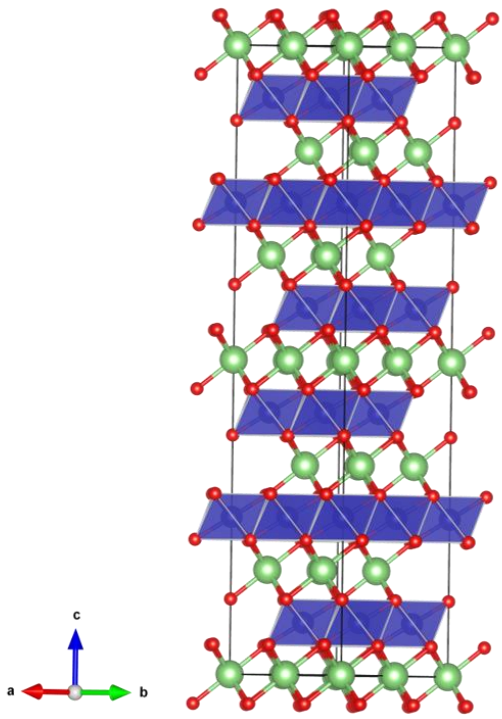

Figure 1.2: Structure of layered material $LiCoO_2$ (R-3m space group). Li is represented in green, Co in blue and O in red.

The theoretical specific capacity of LCO is 280 $mAhg^{-1}$ and the redox reactions are based on the couple Co^{4+}/Co^{3+} [28]. However, the practical specific capacity is limited to 140 $mAhg^{-1}$ because, for $x>0.5$ in $Li_{1-x}CoO_2$, the material undergoes irreversible structural change[29]. Furthermore, cobalt is expensive and toxic.

Significant research efforts have been made on the investigation of new layered materials[23,30], such as the isostructurals $LiNiO_2$ (LNO) and $LiMnO_2$ (LMO) in order to overcome the limits of $LiCoO_2$. LNO is particularly interesting because is cheap and shows high reversible capacity[31,32]. However, it is difficult to synthesize an ordered phase due to the cation mixing of Li^+ and Ni^{3+} in lithium planes and it can release oxygen exothermically in the charged state at elevated temperatures raising safety issues[33]. Layered $LiMnO_2$ (LMO) has also been studied due to its low cost and environmental compatibility[34,35]. As for LNO, its use in lithium cell is limited because it is not electrochemically stable due to an irreversible phase transition into a spinel structure during charge/discharge[36,37].

Two and three-component systems, combining the features of Nickel, Cobalt and Manganese, have also been explored[4,6,38]. $LiNi_xCo_{1-x}O_2$, in which the substitution of Co^{3+} ions with Ni^{3+} ions

decreases cation mixing, was extensively prepared but, when tested in lithium cell, showed capacity fading upon cycling[39]. The electrochemical stability was improved by the introduction of Al^{3+} ions in the structure obtaining the so-called NCA materials, with chemical formula $Li[Ni_xCo_yAl_{1-x-y}]O_2$ [40–42]. Nevertheless, it was found that after prolonged cycling in lithium cell, also NCA materials display a capacity fading due to surface reactions and degradation[23]. The combination of Ni, Co and Mn can lead to a group of compounds with different stoichiometry, the so-called NMC compounds[43,44]. Among the various members of this family, $Li[Ni_{1/3}Mn_{1/3}Co_{1/3}]O_2$ [45,46] has been studied extensively for its promising electrochemical performance, thanks to higher specific capacity. However, also in this case there are several issues, such as capacity fading and poor electrochemical performance at high voltage[47,48].

1.2.2 Spinel structure compounds

The most studied spinel structure material is $LiMn_2O_4$ due to its lower cost and toxicity[49,50]. $LiMn_2O_4$ belongs to the space group Fd3m where the oxygen anions have a closed–packed arrangement in ABCABC stacking sequence, while Li occupies tetrahedral sites and Mn octahedral sites[51]. Therefore, Li^+ can diffuse through vacant tetrahedral and octahedral interstitial sites in the three-dimensional structure. The structure of spinel $LiMn_2O_4$ is shown in figure 1.3.

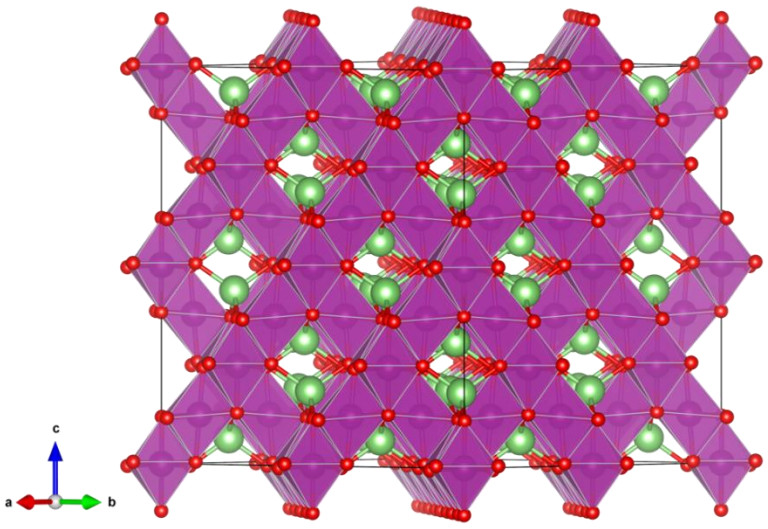

Figure 1.3: Representation of spinel $LiMn_2O_4$ (Fd3m space group). Li is represented in green, Mn in violet and O in red.

The theoretical specific capacity of $LiMn_2O_4$ is 148 $mAhg^{-1}$ but, experimentally, it is possible to achieve around 120 $mAhg^{-1}$ due to a nonreversible phase transition from cubic to tetragonal. It suffers from severe capacity fade, especially at elevated temperatures. This capacity fade is connected to many factors: irreversible reactions with electrolyte, Mn disproportion, Mn dissolution, and formation of tetragonal $Li_2Mn_2O_4$ [52,53].

In order to mitigate the problems of $LiMn_2O_4$, Mn has been partly replaced by other metals to obtain materials with general stoichiometry $LiTM_xMn_{2-x}O_4$ [51,54,55]. The substitution of Mn leads to an increase of its oxidation state and mitigates its disproportion. The result is a greater stability and enhanced life.

1.2.3 Olivine structure compounds

$LiFePO_4$ (LFP) is the most famous material that adopts an olivine structure with Pnma space group[56,57]. In M_2XO_4 olivine structure, 50% of octahedral sites are filled with M while 1/8 of tetrahedral sites in the hexagonal close packed oxygen are occupied by X [58]. The typical olivine structure of LFP is shown in figure 1.4.

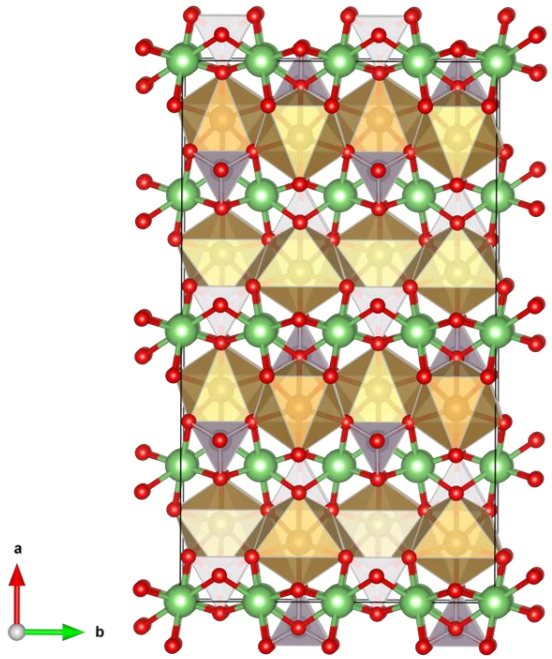

Figure 1.4: Olivine structure of LFP (Pnma space group). Li is represented in green, P in light grey, Fe in ochre and O in red.

During Li removal, the $FePO_4$ phase is formed and coexists with $LiFePO_4$. Upon charging the $FePO_4$ increases and $LiFePO_4$ decreases; as a consequence, the two phase gives a flat voltage curve at around 3.4V[59,60]. The theoretical specific capacity that LFP can achieve is 170 $mAhg^{-1}$, while the main drawbacks are the low average potential and low electrical and ionic conductivity[58].
Many authors studied several methods to improve the electrochemical performance of this material, such as carbon coating, doping with other metals or the decreasing of particle size, leading an experimental specific capacity of 165 $mAhg^{-1}$. This strategies lead to an increase of electronic conductivity and shorter diffusion lengths of Li^+.

1.3 LITHIUM RICH LAYERED OXIDES

Lithium Rich Layered Oxides (LRLOs) are the candidates to replace the common cathode materials presented in section 1.2[61–63]. LRLOs belong to the layered family compounds and they are able to deliver a specific capacity above 250 $mAhg^{-1}$ with high working voltage.
Ideally, LRLOs can be derived from classical layered materials when the latter have an excess of lithium in the stoichiometry. Therefore, Li ions fill the lithium layers and the excess is collocated in the TM layers. Li_2MnO_3 can be used an ideal example of LRLOs. In fact, the formula can be also written as $Li[Li_{1/3}Mn_{2/3}]O_2$ [64,65]. This formula shows well how 1/3 of the site of TM is actually occupied by Li ions.
Further investigations have expanded the amount of LRLOs explored and the following section is devoted to explain the main features of this class of compounds.

1.3.1 Notation and structure of LRLOs

In general, LRLOs are reported in literature with two different notations: 1) $xLi_2MnO_3 \cdot (1-x)LiTMO_2$ or 2) $Li_{1+x}TM_{1-x}O_2$ [66–69]. The two notations express different ways to see the composition. The first says that the materials are made up of domains of Li_2MnO_3 and $LiTMO_2$. The monoclinic Li_2MnO_3 (C2/m space group) and the rhombohedral $LiTMO_2$ (R-3m space group) coexist and the materials are represented as a nano-composite [70–72]. On the other hand, the second notation express simply the lithium excess into the material compared to normal layered compounds and Li_2MnO_3 and $LiTMO_2$ are deal as a solid solution[73–75]. Both the notations have

advantages and are used interchangeably in the literatures. Figure 1.5 shows the unit cells of both domains.

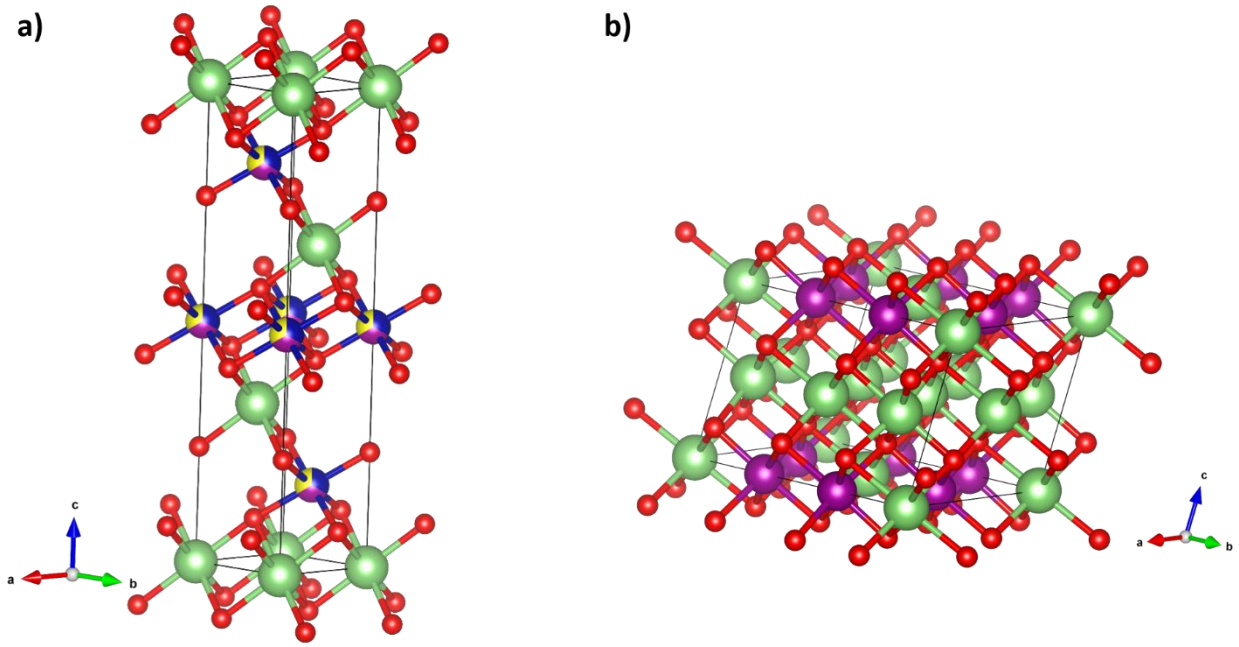

Figure 1.5: a) R-3m unit cell of $LiTMO_2$. b) C2/m structure of Li_2MnO_3. Li is represented in green, Mn in violet, Co in blue, Ni in yellow and O in red.

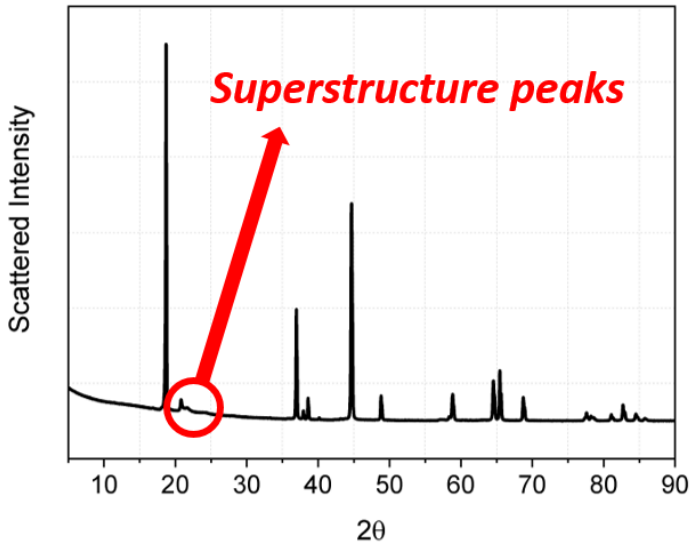

Figure 1.6: Example of experimental XRD pattern obtained for LRLOs.

The structure of LRLOs is still debated. The most relevant difference in the XRD pattern compared to other layered materials is the presence of extra peaks between 20°-35°. An example of a

representative XRD pattern is shown in figure 1.6. According to the nano-composite perspective, the extra peaks are due to the $LiMn_6$ cation ordering in the Li_2MnO_3 domains[76]. Regarding to the solid-solution perspective, superlattice peaks are related to long-range lithium ordering in the TM layers[77].

Up to now, it is possible to find many references to support one or the other theory. The X-Ray diffraction is not able to discriminate between nano-composite or solid solution structures. Rietveld refinement with two phase models leads to good fitting results[78,79] but, in many cases, the calculated lattice parameters follow the Vegard's rule[43,80], suggesting a solid solution. Moreover, the Neutron diffraction should help in the description of the structure due to the sensitivity to the light element like Li and the different scattering of transition metals. However, refinement with R-3m and C/2m unit cells or with two phase model lead to the same results[81–83]. Raman spectroscopy has been used to reveal the structure, the spectrum shows the features of both Li_2MnO_3 and $LiTMO_2$ but not just a simple combination of the two structures[54,69,81,84].

Also for TEM and ED analysis, the discussion is open, in fact, while many authors have found proofs of two coexisting phases[85–88], other references showed evidences of a single phase with huge amount of stacking faults[89–92]. Therefore, the question is also complicated by many defects within the materials. The presence of stacking faults seems to explain better these features compared to the long-range cationic ordering[87,93].

The difficulties of the structural description and the discordant results reported above depends on the method used to synthetize the materials, the annealing temperature, the precursors used, the transitional metals present in the stoichiometry and the amount of excess lithium in the TM layers.

1.3.2 Electrochemical behavior of LRLOs in lithium cell

The most important advantage of LRLOs is the high specific capacity, around 250 $mAhg^{-1}$. Figure 1.7 shows the potential profile of a well-known LRLO, $Li_{1.2}Mn_{0.54}Ni_{0.13}Co_{0.13}O_2$ [94–96]. Upon the first charge, the potential profile can be divided in two main parts: 1) a sloping part from the OCV to 4.5V and 2) a voltage plateau part around 4.5/4.6V[97–99]. This latter process is irreversible, as can be noted from the figure. The following charge/discharge profiles are different from the first one and they appear similar to the behavior observed in the other layered materials.

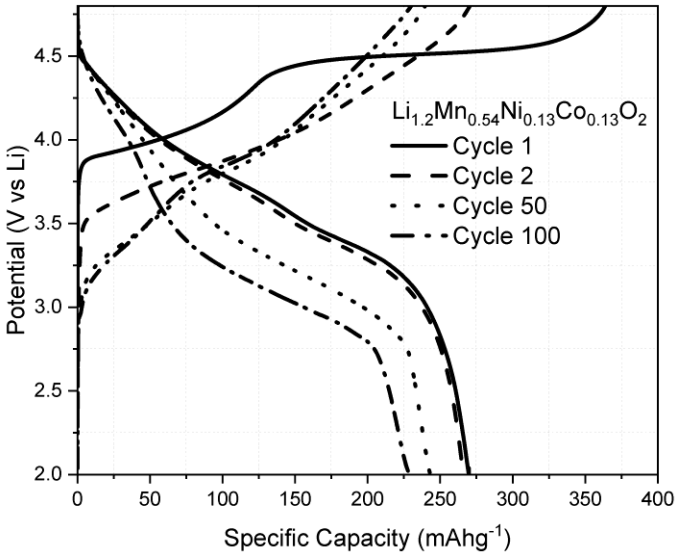

Figure 1.7: Typical potential profile of LRLOs.

The sloping region is usually connected to the oxidation of transition metals. For example, in the case of $Li_{1.2}Mn_{0.54}Ni_{0.13}Co_{0.13}O_2$ reported in figure 1.5, the oxidation states of metals are Mn^{4+}, Ni^{2+} and Co^{3+}. Therefore, the first process is due to the oxidation of nickel and cobalt to Ni^{4+} and Co^{4+} [61,97]. However, the large part of capacity is delivered during the second electrochemical process, observed in the figure as the high voltage plateau. Since the metals are already oxidized at lower voltages, in the slope part of voltage profile, that means that Li ions can be extracted beyond the cationic redox process. The reaction mechanism of this voltage plateau has been extensively investigated[38,99–101]. Many author proposed and then confirmed the occurrence of an anionic redox reactions, involving the lattice oxygen[61,62,102–105]. Therefore, the further lithium extraction is balanced by the activation of O^{2-}/O^{-} redox couple with O_2 release. A more detailed explanation of this anionic redox will be reported in chapter 3.

As mentioned before the potential profile changes drastically after the first charge, in fact, the reaction during the plateau is partially irreversible and disappears upon subsequent cycles. Therefore, a large irreversible capacity loss is connected to the molecular oxygen loss from the lattice. During the first discharge, Ni and Co are reduced and, moreover, Mn^{4+} is also available to be reduced. In the subsequent cycles, the potential profiles follow a slope both in charge and in discharge and it is possible to note a voltage decay upon cycling. The voltage decay is considered

the main drawback of LRLOs and it is associated to the reactions occurring during the first cycle and with a structural change from layered to spinel-like structure[67,106–108].

1.3.3 Strategy to improve the electrochemical performance of LRLOs in lithium cell

As outlined above, despite of high specific capacity and energy density, LRLOs displays the following relevant issues:

- Irreversible capacity lost during the first cycle;
- Working voltage fade;
- Poor rate capability;
- Poor understanding of pristine structure and its evolution upon cycling.

All these problems compromise so far the practical use of LRLOs in a commercial Lithium-Ion Battery. Different strategies are used in order to reduce or eliminate these issues. The adopted strategies included different synthetic processes, doping (cationic or anionic), surface coating, as well as the control of the composition and the electrolyte optimization[38,61,98,109–111].

For example, doping was shown to be able to reduce the voltage decay and the irreversible capacity loss during the first cycle. Nayal et al.[107] prepared a series of Al-doped lithium rich materials, $Li_{1.2}Ni_{0.16}Mn_{0.56-x}Al_xCo_{0.08}O_2$ (x= 0.02, 0.05, and 0.08) where aluminum is used to replace manganese in the structure leading to a doped material with x=0.05 showing a specific capacity of 200 $mAhg^{-1}$ and capacity retention of 98% after 100 cycles. Bao et al.[112] prepared a series of Yb doped lithium rich materials, $Li_{1.2}Ni_{0.13}Co_{0.13-x}Yb_xMn_{0.54}O_2$. The best materials obtained, with x=0.005, exhibited a discharge capacity of 250.3 and 219.8 $mAhg^{-1}$ at 0.2 and 1C, respectively. Capacity retentions were 87.3 and 84.4% after 50 cycles at 0.2 C and 100 cycles at 1C. Nayak et al.[108] proposed lithium rich material $Li_{1.2}Ni_{0.13+x}Mn_{0.54-x}Co_{0.13}O_2$ in which Mn ions are substituted by Ni ions to improve electrochemical performance. $Li_{1.2}Ni_{0.27}Mn_{0.40}Co_{0.13}O_2$ showed the best performance; indeed, it had a specific capacity of 210 $mAhg^{-1}$ and a discharge voltage of 3.5 V after 150 cycles. Kou et al.[113] prepared a series of Ti doped lithium rich, $Li_{1.167}Ni_{0.4-x}Mn_{0.383}Co_{0.05}Ti_xO_2$ (x = 0, 0.02, 0.04 and 0.08). Ti doping have an impact on electrochemical performance and doped material with x=0.04 showed the best performance. It has a discharge capacity of 187 $mAhg^{-1}$ with a capacity retention of 99.4% after 10 cycles at 0.1 C. Also anionic doping has been extensively used, Zhang et al.[114] used PO_4^{3-} polyanions doping in

$Li(Li_{0.17}Ni_{0.20}Co_{0.05}Mn_{0.58})O_2$ to partly replace oxygen. In particular, $Li(Li_{0.17}Ni_{0.20}Co_{0.05}Mn_{0.58})O_{1.95}$ $(PO_4^{3-})_{0.05}$ showed improvements in stability and in the discharge midpoint potential. Wang et al.[115] used coprecipitation method to obtain $Li(Li_{0.133}Ni_{0.20}Co_{0.2}Mn_{0.467})O_{1.95}F_{1.95}$ where the initial Coulombic efficiency, cycle performance, and voltage degradation have been improved. About the composition, Lee et al[102] synthetized a series of materials with different metals blend, demonstrating how the length of the high voltage plateau in the first charge depends on the composition and how to improve the initial efficiency.

Surface coating is also an important strategy to improve the electrochemical performance protecting the materials to the direct contact of the electrolyte and modifying the surface chemistry. Liu et al.[116] used a coating with 1wt.% Al_2O_3+ 1 wt.% RuO_2 on $Li_{1.2}Mn_{0.54}Ni_{0.13}Co_{0.13}O_2$, improving the initial coulombic efficiency and the capacity retention after 30 cycles. Recently, Liu et al.[117] prepared a perovskite-type $LaMnO_3$ modified layer on the surface of Li-rich Mn-based cathode, obtaining a very promising rate capability (155 $mAhg^{-1}$ at 5C) and a good cycle durability. Wang et al.[118] prepared an Al_2O_3-modified LRLO, via a low temperature melting impregnation method, with enhanced capacity retention after 300 cycles.

Moreover, different synthetic routes with different morphology can be used to improve the electrochemical behavior of LRLOs. For example, Ma et al.[119] used a modified coprecipitation method to synthetize microrods $0.5\ Li_2MnO_3 \cdot 0.5\ LiNi_{1/3}Co_{1/3}Mn_{1/3}O_2$. The 1D shape can provide a short distance for Li^+ ion diffusion, facilitating Li^+ ion movement and improving the performance. Furthermore, the modifications of the electrolytes have been performed to improve mainly the oxidation stability under high voltages. In this regard, it is possible to use different solvents, ionic liquids and additives[120–122]. Additives like bis(oxalate)borate (LiBOB)[123,124] and tri(hexafluoro-iso-propyl) phosphate $((C_3HF_6O)_3PO)$[125] were used to improve the cycling stability of LRLOs. Many authors have successfully demonstrated that also pure ionic liquids or their mixing with organic solvents can improve the interfacial stability, the capacity retention and reduce the side reaction between the electrode and the electrolyte[63,126,127]. The table 1.1 shows a summary of the example presented in the section.

Table 1.1: Examples of strategy used to improve the electrochemical performance of LRLOs.

Strategy	Compound	Specific Capacity ($mAhg^{-1}$)	Capacity retention (%)	Ref
Al Doping	$Li_{1.2}Ni_{0.16}Mn_{0.51}Al_{0.05}Co_{0.08}O_2$	210	96 (100 cycles)	107
Yb Doping	$Li_{1.2}Ni_{0.13}Co_{0.125}Yb_{0.005}Mn_{0.54}O_2$	250	87 (50 cycles)	112
Ti Doping	$Li_{1.167}Ni_{0.36}Mn_{0.383}Co_{0.05}Ti_{0.04}O_2$	187	99 (10 cycles)	113
Ni Doping	$Li_{1.2}Ni_{0.27}Mn_{0.40}Co_{0.13}O_2$	210	-	108
PO_4^{3-} Doping	$Li(Li_{0.17}Ni_{0.20}Co_{0.05}Mn_{0.58})O_{1.95}(PO_4^{3-})_{0.05}$	250	-	114
F Doping	$Li(Li_{0.133}Ni_{0.20}Co_{0.2}Mn_{0.467})O_{1.95}F_{1.95}$	236	92 (100 cycles)	115
Al_2O_3 + RuO_2 Surface Coating	$Li_{1.2}Mn_{0.54}Ni_{0.13}Co_{0.13}O_2$	280	94 (30 cycles)	116
Perovskite-$LaMnO_3$ Surface coating	$Li_{1.2}Mn_{0.54}Ni_{0.13}Co_{0.13}O_2$	230	85 (200 cycles)	117
Al_2O_3 Surface coating	$Li_{1.2}Mn_{0.56}Ni_{0.16}Co_{0.08}O_2$	233	89 (100 cycles)	118
Microrods morphology	$0.5Li_2MnO_3{\cdot}0.5LiNi_{1/3}Co_{1/3}Mn_{1/3}O_2$	221	95 (100 cycles)	119
4 wt.% LiBOB additive electrolyte	$Li_{1.2}Mn_{0.56}Ni_{0.16}Co_{0.08}O_2$	200	98 (100 cycles)	124
$P_{4444}IM_{14}$ Ionic Liquid	$Li_{1.2}Mn_{0.6}Ni_{0.2}O_2$	240	84 (100 cycles)	126
0.2LiTFSI-0.8EMIFS Ionic liquid	$Li_{1.2}Mn_{0.6}Ni_{0.2}O_2$	200	73 (100 cycles)	127

1.4 RESEARCH OBJECTIVES AND STRUCTURE OF THE THESIS

As highlighted before, the development of new materials is mandatory to satisfy the increasing demand for Li-ion battery systems delivering higher capacity, energy density, cycle life stability and safety. While in the case of anode, the research has led already to the identification of a new generation of anode materials, such as Silicon (3500 $mAhg^{-1}$), that are much more performing compared to graphite (≈370 $mAhg^{-1}$) and do offer a promising route for substituting graphite, the real bottleneck remains the cathode side. Therefore, current substantial efforts are devoted to the design and optimization of positive electrode materials displaying large capacity values (>200 mAhg-1) and/or high average voltages.

In this context, Li-Rich Layered Oxides (LRLOs) have attracted much attention recently due to their superior high specific capacity and high working voltage. As explained above there are still some challenges for Li-rich cathode materials to overcome before practical application. First of all, a fundamental understanding of the pristine structure is still not available, as well as the electrochemical reaction mechanisms and the crystal structure evolution is still not completely understood. Moreover, another important element to be considered is the compatibility of these materials with the large-scale production. Among the major requirements there are the costs and the environmental impact of raw materials and manufacture. Cobalt represents the main issue due to its high cost and high toxicity.

This thesis aims to develop new high capacity Li-rich Layered Oxides cathode materials for LIBs that are able to offer high capacity and stable cycling with a reduced amount of cobalt. The thesis is structured in the following way:

Chapter 2 is devoted to the doping and the replacement of cobalt within the structure of $Li_{1.2}Mn_{0.54}Ni_{0.13}Co_{0.13}O_2$. The impact of cobalt substitution by other metals on the structure and the electrochemical performance is investigated. In particular, the replacement by Li is discussed, showing improvements in the electrochemical behavior.

Chapter 3 reports the analysis of reaction mechanism of the developed $Li_{1.28}Mn_{0.54}Ni_{0.13}Co_{0.02}Al_{0.03}O_2$ upon cycling, in particular at different points of first two cycles and after ten cycles. Synchrotron X-Ray Diffraction and Raman Spectroscopy are used for this purpose.

Chapter 4 focuses on the pristine structure of LRLOs. A combination of synchrotron X-Ray Diffraction and Neutron Diffraction allowed to prove supercells and investigate defects into the material, in particular stacking faults and Li-TM mixing in TM layers.

Chapter 5 is dedicated to the improvement of the standard organic electrolyte with the use of ionic liquids. LRLOs work in a very wide range of voltage, therefore it is important to have an electrolyte with a wider stability window. Different ionic liquids and lithium salts are investigated.

REFERENCES

1. Goodenough, J. B. & Park, K. S. The Li-ion rechargeable battery: A perspective. *Journal of the American Chemical Society* **135**, 1167–1176 (2013).
2. Yoshino, A. The birth of the lithium-ion battery. *Angewandte Chemie - International Edition* **51**, 5798–5800 (2012).
3. Armand, M. & Tarascon, J.-M. Building better batteries. *Nature* **451**, 652–657 (2008).
4. Choi, N. S. *et al.* Challenges facing lithium batteries and electrical double-layer capacitors. *Angewandte Chemie - International Edition* **51**, 9994–10024 (2012).
5. Tarascon, J. M. & Armand, M. Issues and challenges facing rechargeable lithium batteries. *Nature* **414**, 359–367 (2001).
6. Nitta, N., Wu, F., Lee, J. T. & Yushin, G. Li-ion battery materials: Present and future. *Materials Today* **18**, 252–264 (2015).
7. Lee, H., Yanilmaz, M., Toprakci, O., Fu, K. & Zhang, X. A review of recent developments in membrane separators for rechargeable lithium-ion batteries. *Energy and Environmental Science* **7**, 3857–3886 (2014).
8. Yang, M. & Hou, J. Membranes in lithium ion batterie. *Membranes* **2**, 367–383 (2012).
9. Lyu, Y. *et al.* An Overview on the Advances of $LiCoO_2$ Cathodes for Lithium-Ion Batteries. *Advanced Energy Materials* **11**, (2021).
10. Wu, Y. P., Rahm, E. & Holze, R. *Carbon anode materials for lithium ion batteries*.
11. Zhang, S. S. A review on electrolyte additives for lithium-ion batteries. *Journal of Power Sources* **162**, 1379–1394 (2006).
12. Dahn, J. R., Zheng, T., Liu, Y. & Xue, J. S. Mechanisms for Lithium Insertion in Carbonaceous Materials. *Science (80-.).* **270**, 590–593 (1995).
13. Andersson, A. M. & Edström, K. Chemical Composition and Morphology of the Elevated Temperature SEI on Graphite. *J. Electrochem. Soc.* **148**, A1100 (2001).
14. Yao, Y. *et al.* Interconnected silicon hollow nanospheres for lithium-ion battery anodes with long cycle life. *Nano Lett.* **11**, 2949–2954 (2011).
15. Franco Gonzalez, A., Yang, N. H. & Liu, R. S. Silicon Anode Design for Lithium-Ion Batteries: Progress and Perspectives. *J. Phys. Chem. C* **121**, 27775–27787 (2017).

16. Abouali, S. *et al.* From scaled-up production of silicon-graphene nanocomposite to the realization of an ultra-stable full-cell Li-ion battery. *2D Mater.* **8**, (2021).
17. Huggins, R. A. *Advanced batteries: Materials science aspects*. *Advanced Batteries: Materials Science Aspects* (Springer US, 2009). doi:10.1007/978-0-387-76424-5
18. Ozawa, K. *Lithium ion rechargeable batteries*. (Wiley-VCH, 2009).
19. Li, M., Lu, J., Chen, Z. & Amine, K. 30 Years of Lithium-Ion Batteries. *Advanced Materials* **30**, 1800561 (2018).
20. Manthiram, A. An Outlook on Lithium Ion Battery Technology. *ACS Cent. Sci.* **3**, 1063–1069 (2017).
21. Radin, M. D. *et al.* Narrowing the Gap between Theoretical and Practical Capacities in Li-Ion Layered Oxide Cathode Materials. *Advanced Energy Materials* **7**, (2017).
22. Shobana, M. K. Metal oxide coated cathode materials for Li ion batteries – A review. *Journal of Alloys and Compounds* **802**, 477–487 (2019).
23. Chakraborty, A. *et al.* Layered Cathode Materials for Lithium-Ion Batteries: Review of Computational Studies on $LiNi_{1-x-y}Co_xMn_yO_2$ and $LiNi_{1-x-y}Co_xAl_yO_2$. *Chem. Mater.* **32**, 915–952 (2020).
24. Cho, J., Kim, Y. J. & Park, B. Novel $LiCoO_2$ cathode material with Al_2O_3 coating for a Li ion cell. *Chem. Mater.* **12**, 3788–3791 (2000).
25. Peng, Z. S., Wan, C. R. & Jiang, C. Y. *Synthesis by sol-gel process and characterization of LiCoO 2 cathode materials*. *Journal of Power Sources* **72**, (1998).
26. Montoro, L. A., Abbate, M., Almeida, E. C. & Rosolen, J. M. Electronic structure of the transition metal ions in $LiCoO_2$, $LiNiO_2$ and $LiCo_{0.5}Ni_{0.5}O_2$. *Chem. Phys. Lett.* **309**, (1999).
27. Yang, J. H., Kim, H. & Ceder, G. Insights into layered oxide cathodes for rechargeable batteries. *Molecules* **26**, (2021).
28. Antolini, E. LiCoO2: Formation, structure, lithium and oxygen nonstoichiometry, electrochemical behaviour and transport properties. *Solid State Ionics* **170**, 159–171 (2004).
29. Reimers, J. N. & Dahn, J. R. Electrochemical and In Situ X-Ray Diffraction Studies of Lithium Intercalation in Li_xCoO_2. *J. Electrochem. Soc.* **139**, 2091 (1992).
30. Erickson, E. M. *et al.* Review—Recent Advances and Remaining Challenges for Lithium Ion Battery Cathodes. *J. Electrochem. Soc.* **164**, A6341–A6348 (2017).
31. Dahn, J. R., Von Sacken, U. & Michal, C. A. Structure and electrochemistry of $Li_{1\pm y}NiO_2$

and a new Li_2NiO_2 phase with the $Ni(OH)_2$ structure. *Solid State Ionics* **44**, (1990).

32. Dahn, J. R. & Al-Janaby, H. Rechargeable $LiNiO_2$/carbon cells. *J. Electrochem. Soc.* **138**, 2207 (1991).
33. Arai, H., Okada, S., Sakurai, Y. & Yamaki, J.-I. Thermal behavior of $Li_{1-y}NiO_2$ and the decomposition mechanism. *Solid State Ionics* **109**, (1998).
34. Armstrong, A. R. & Bruce, P. Synthesis of layered $LiMnO_2$ as an electrode for rechargeable lithium batteries. *Nature* **381**, 499–500 (1996).
35. Armstrong, A. R., Paterson, A. J., Robertson, A. D. & Bruce, P. G. Nonstoichiometric layered $Li_xMn_yO_2$ with a high capacity for lithium intercalation/deintercalation. *Chem. Mater.* **14**, 710–719 (2002).
36. Mishra, S. K. & Ceder, G. *Structural stability of lithium manganese oxides*.
37. Croguennec, L., Deniard, P. & Brec, R. Electrochemical Cyclabilily of Orthorhombic $LiMnO_2$. *Journal of the Electrochemical Society* **144**, (1997).
38. Rozier, P. & Tarascon, J. M. Review—Li-Rich Layered Oxide Cathodes for Next-Generation Li-Ion Batteries: Chances and Challenges. *J. Electrochem. Soc.* **162**, A2490–A2499 (2015).
39. Rougier, A., Saadoune, I., Gravereau, P., Willmannb, F. & Delmas, C. Effect of cobalt substitution on cationic distribution in $LiNi_{1-y}Co_yO$ electrode materials. *Solid State Ionics* **90**, (1996).
40. Yudha, C. S. *et al.* Synthesis of $LiNi_{0.85}Co_{0.14}Al_{0.01}O_2$ cathode material and its performance in an NCA/graphite full-battery. *Energies* **12**, (2019).
41. Leifer, N. *et al.* $LiNi_{0.8}Co_{0.15}Al_{0.05}O_2$ Cathode Material: New Insights via 7Li and 27Al Magic-Angle Spinning NMR Spectroscopy. *Chem. Mater.* **28**, 7594–7604 (2016).
42. Purwanto, A. *et al.* NCA cathode material: Synthesis methods and performance enhancement efforts. *Materials Research Express* **5**, (2018).
43. Lu, Z., MacNeil, D. D. & Dahn, J. R. Layered $Li[Ni_xCo_{1-2x}Mn_x]O_2$ cathode materials for lithium-ion batteries. *Electrochem. Solid-State Lett.* **4**, (2001).
44. Myung, S. T. *et al.* Nickel-Rich Layered Cathode Materials for Automotive Lithium-Ion Batteries: Achievements and Perspectives. *ACS Energy Letters* **2**, 196–223 (2017).
45. Ngala, J. K. *et al.* The synthesis, characterization and electrochemical behavior of the layered $LiNi_{0.4}Mn_{0.4}Co_{0.2}O_2$ compound. *J. Mater. Chem.* **14**, 214–220 (2004).

46. Belharouak, I., Sun, Y. K., Liu, J. & Amine, K. $Li(Ni_{1/3}Co_{1/3}Mn_{1/3})O_2$ as a suitable cathode for high power applications. *J. Power Sources* **123**, 247–252 (2003).
47. Shaju, K. M., Rao, G. V. S. & Chowdari, B. V. R. Performance of layered $Li(Ni_{1/3}Co_{1/3}Mn_{1/3})O_2$ as cathode for Li-ion batteries. *Electrochim. Acta* **48**, 145–151 (2002).
48. Yang, X. *et al.* Mechanism of cycling degradation and strategy to stabilize a nickel-rich cathode. *J. Mater. Chem. A* **6**, 16149–16163 (2018).
49. Yi, T. F., Hao, C. L., Yue, C. B., Zhu, R. S. & Shu, J. A literature review and test: Structure and physicochemical properties of spinel $LiMn_2O_4$ synthesized by different temperatures for lithium ion battery. *Synth. Met.* **159**, 1255–1260 (2009).
50. Thackeray, M. M., David, W. I. F., Bruce, P. G. & Goodenough, J. B. Lithium insertion into manganese spinels. *Mater. Res. Bull.* **18**, 461–472 (1983).
51. Shigemura, H. *et al.* Structure and Electrochemical Properties of $LiFe_xMn_{2-x}O_4$ ($0 \leq x \leq 0.5$) Spinel as 5 V Electrode Material for Lithium Batteries. *J. Electrochem. Soc.* **148**, A730 (2001).
52. Shin, Y. & Manthiram, A. Influence of the lattice parameter difference between the two cubic phases formed in the 4 V region on the capacity fading of spinel manganese oxides. *Chem. Mater.* **15**, 2954–2961 (2003).
53. Shin, Y. & Manthiram, A. Factors Influencing the Capacity Fade of Spinel Lithium Manganese Oxides. *J. Electrochem. Soc.* **151**, A204 (2004).
54. Wei, Y., Nam, K. W., Kim, K. B. & Chen, G. Spectroscopic studies of the structural properties of Ni substituted spinel LiMn2O4. *Solid State Ionics* **177**, 29–35 (2006).
55. Wei, Y., Kim, K. B. & Chen, G. Evolution of the local structure and electrochemical properties of spinel $LiNi_xMn_{2-x}O_4$ ($0 \leq x \leq 0.5$). *Electrochim. Acta* **51**, 3365–3373 (2006).
56. Padhi, A. K., Nanjundaswamy, K. 5 & Goodenough, J. B. Phospho-olivines as positive-electrode materials for rechargeable lithium batteries. *J. Electrochem. Soc.* **144**, 16 (1997).
57. Okada, S. *et al.* Cathode properties of phospho-olivine $LiMPO_4$ for lithium secondary batteries. *J. Power Sources* **97**, 430–432 (2001).
58. Zhang, W. J. Structure and performance of $LiFePO_4$ cathode materials: A review. *Journal of Power Sources* **196**, 2962–2970 (2011).
59. Ramana, C. V., Mauger, A., Gendron, F., Julien, C. M. & Zaghib, K. Study of the Li-

insertion/extraction process in $LiFePO_4/FePO_4$. *J. Power Sources* **187**, 555–564 (2009).

60. Andersson, A. S. & Thomas, J. O. The source of first-cycle capacity loss in $LiFePO_4$. *J. Power Sources* **97**, 498–502 (2001).
61. Wang, J. *et al.* Lithium- and Manganese-Rich Oxide Cathode Materials for High-Energy Lithium Ion Batteries. *Adv. Energy Mater.* **6**, (2016).
62. Susai, F. A. *et al.* Horizons for Li-Ion Batteries Relevant to Electro-Mobility: High-Specific-Energy Cathodes and Chemically Active Separators. *Advanced Materials* **30**, (2018).
63. Tan, S., Ji, Y. J., Zhang, Z. R. & Yang, Y. Recent progress in research on high-voltage electrolytes for lithium-ion batteries. *ChemPhysChem* **15**, 1956–1969 (2014).
64. Yu, D. Y. W., Yanagida, K., Kato, Y. & Nakamura, H. Electrochemical Activities in Li_2MnO_3. *J. Electrochem. Soc.* **156**, A417 (2009).
65. Armstrong, A. R., Robertson, A. D. & Bruce, P. G. Overcharging manganese oxides: Extracting lithium beyond $Mn4^+$. in *Journal of Power Sources* **146**, 275–280 (2005).
66. Thackeray, M. M., Kang, S. H., Johnson, C. S., Vaughey, J. T. & Hackney, S. A. Comments on the structural complexity of lithium-rich $Li_{1+x}M_{1-x}O_2$ electrodes (M = Mn, Ni, Co) for lithium batteries. *Electrochem. commun.* **8**, 1531–1538 (2006).
67. Mohanty, D. *et al.* Neutron diffraction and magnetic susceptibility studies on a high-voltage $Li_{1.2}Mn_{0.55}Ni_{0.15}Co_{0.10}O_2$ lithium ion battery cathode: Insight into the crystal structure. *Chem. Mater.* **25**, 4064–4070 (2013).
68. Qiu, B. *et al.* Temperature dependence of the initial coulombic efficiency in Li-rich layered $Li[Li_{0.144}Ni_{0.136}Co_{0.136}Mn_{0.544}]O_2$ oxide for lithium-ions batteries. *J. Power Sources* **268**, 517–521 (2014).
69. Lanz, P., Villevieille, C. & Novák, P. Ex situ and in situ Raman microscopic investigation of the differences between stoichiometric $LiMO_2$ and high-energy $xLi_2MnO_3 \cdot (1-x)LiMO_2$ (M = Ni, Co, Mn). *Electrochim. Acta* **130**, 206–212 (2014).
70. Gummow, R. J., Sharma, N., Feng, R., Han, G. & He, Y. High Performance Composite Lithium-Rich Nickel Manganese Oxide Cathodes for Lithium-Ion Batteries. *J. Electrochem. Soc.* **160**, A1856–A1862 (2013).
71. Yu, H. *et al.* High-energy 'composite' layered manganese-rich cathode materials via controlling Li_2MnO_3 phase activation for lithium-ion batteries. *Phys. Chem. Chem. Phys.*

14, 6584–6595 (2012).

72. Wen, J. G. *et al.* Analytical electron microscopy of $Li_{1.2}Co_{0.4}Mn_{0.4}O_2$ for lithium-ion batteries. *Solid State Ionics* **182**, 98–107 (2011).
73. Bréger, J. *et al.* High-resolution X-ray diffraction, DIFFaX, NMR and first principles study of disorder in the Li_2MnO_3-$Li[Ni_{1/2}Mn_{1/2}]O_2$ solid solution. *J. Solid State Chem.* **178**, 2575–2585 (2005).
74. Ohzuku, T., Nagayama, M., Tsuji, K. & Ariyoshi, K. High-capacity lithium insertion materials of lithium nickel manganese oxides for advanced lithium-ion batteries: Toward rechargeable capacity more than 300 $mAhg^{-1}$. *J. Mater. Chem.* **21**, 10179–10188 (2011).
75. Kikkawa, J. *et al.* Real-space observation of Li extraction/Insertion in $Li_{1.2}Mn_{0.4}Fe_{0.4}O_2$ positive electrode material for Li-ion batteries. *Electrochem. Solid-State Lett.* **11**, (2008).
76. Johnson, C. S. *et al.* The significance of the Li_2MnO_3 component in 'composite' $xLi_2MnO_3{\cdot}(1 - x)LiMn_{0.5}Ni_{0.5}O_2$ electrodes. *Electrochem. commun.* **6**, 1085–1091 (2004).
77. West, W. C. *et al.* Electrochemical Behavior of Layered Solid Solution $Li_2MnO_3{-}LiMO_2$ (M = Ni, Mn, Co) Li-Ion Cathodes with and without Alumina Coatings. *J. Electrochem. Soc.* **158**, A883 (2011).
78. Yu, H. & Zhou, H. High-energy cathode materials (Li_2MnO_3-$LiMO_2$) for lithium-ion batteries. *Journal of Physical Chemistry Letters* **4**, 1268–1280 (2013).
79. Boulineau, A. *et al.* Evolutions of $Li_{1.2}Mn_{0.61}Ni_{0.18}Mg_{0.01}O_2$ during the initial charge/discharge cycle studied by advanced electron microscopy. *Chem. Mater.* **24**, 3558–3566 (2012).
80. Lu, Z., MacNeil, D. D. & Dahn, J. R. Layered cathode materials $Li[Ni_xLi_{(1/3-2x/3)}Mn_{(2/3-x/3)}]O_2$ for lithium-ion batteries. *Electrochem. Solid-State Lett.* **4**, A191 (2001).
81. Koga, H. *et al.* $Li_{1.20}Mn_{0.54}Co_{0.13}Ni_{0.13}O_2$ with different particle sizes as attractive positive electrode materials for lithium-ion batteries: Insights into their structure. *J. Phys. Chem. C* **116**, 13497–13506 (2012).
82. Mohanty, D. *et al.* Unraveling the voltage-fade mechanism in high-energy-density lithium-ion batteries: Origin of the tetrahedral cations for spinel conversion. *Chem. Mater.* **26**, 6272–6280 (2014).
83. Amalraj, F. *et al.* Synthesis of Integrated Cathode Materials $xLi_2MnO_3{\cdot}(1{-}x)LiMn_{1/3}Ni_{1/3}Co_{1/3}O_2$ (x=0.3, 0.5, 0.7) and Studies of Their Electrochemical

Behavior. *J. Electrochem. Soc.* **157**, S19 (2010).

84. Wu, Q. *et al.* A Raman-Based Investigation of the Fate of Li_2MnO_3 in Lithium- and Manganese-Rich Cathode Materials for Lithium Ion Batteries . *J. Electrochem. Soc.* **162**, A1255–A1264 (2015).
85. Yu, H. *et al.* Direct Atomic-Resolution Observation of Two Phases in the $Li_{1.2}Mn_{0.567}Ni_{0.166}Co_{0.067}O_2$ Cathode Material for Lithium-Ion Batteries . *Angew. Chemie* **125**, 6085–6089 (2013).
86. Yu, X. *et al.* Understanding the rate capability of high-energy-density Li-rich layered $Li_{1.2}Ni_{0.15}Co_{0.1}Mn_{0.55}O_2$ cathode materials. *Adv. Energy Mater.* **4**, (2014).
87. Shukla, A. K. *et al.* Effect of composition on the structure of lithium- and manganese-rich transition metal oxides. *Energy Environ. Sci.* **11**, 830–840 (2018).
88. Amalraj, F. *et al.* Integrated Materials $xLi_2MnO_3{\cdot}(1-x)LiMn_{1/3}Ni_{1/3}Co_{1/3}O_2$ (x=0.3, 0.5, 0.7) Synthesized. *J. Electrochem. Soc.* **157**, A1121 (2010).
89. Bareño, J. *et al.* Long-range and local structure in the layered oxide $Li_{1.2}Co_{0.4}Mn_{0.4}O_2$. *Chem. Mater.* **23**, 2039–2050 (2011).
90. Jarvis, K. A., Deng, Z., Allard, L. F., Manthiram, A. & Ferreira, P. J. Atomic structure of a lithium-rich layered oxide material for lithium-ion batteries: Evidence of a solid solution. *Chem. Mater.* **23**, 3614–3621 (2011).
91. Gu, M. *et al.* Nanoscale phase separation, cation ordering, and surface chemistry in pristine $Li_{1.2}Ni_{0.2}Mn_{0.6}O_2$ for Li-ion batteries. *Chem. Mater.* **25**, 2319–2326 (2013).
92. Fujiia, H., Ozawa, K. & Mochiku, T. Electron diffraction and high-resolution electron microscopy studies on layered $Li_{2-\delta}(Mn_{1-x}Co_x)_{1+\delta}O_3$. *J. Solid State Chem.* **203**, 345–352 (2013).
93. Shunmugasundaram, R., Arumugam, R. S. & Dahn, J. R. A Study of Stacking Faults and Superlattice Ordering in Some Li-Rich Layered Transition Metal Oxide Positive Electrode Materials. *J. Electrochem. Soc.* **163**, A1394–A1400 (2016).
94. Zhao, L., Wu, Q. & Wu, J. Improving rate performance of cathode material $Li_{1.2}Mn_{0.54}Co_{0.13}Ni_{0.13}O_2$ via niobium doping. *J. Solid State Electrochem.* **22**, 2141–2148 (2018).
95. Venkateswara Rao, C. *et al.* Investigations on electrochemical behavior and structural stability of $Li_{1.2}Mn_{0.54}Ni_{0.13}Co_{0.13}O_2$ lithium-ion cathodes via in-situ and ex-situ Raman

spectroscopy. *J. Phys. Chem. C* **118**, 14133–14141 (2014).

96. Sun, Y., Wu, Q. & Zhao, L. A new doping element to improve the electrochemical performance of $Li_{1.2}Mn_{0.54}Ni_{0.13}Co_{0.13}O_2$ materials for Li-ion batteries. *Ceram. Int.* **45**, 1339–1347 (2019).
97. Zhao, S., Yan, K., Zhang, J., Sun, B. & Wang, G. Reaction Mechanisms of Layered Lithium-Rich Cathode Materials for High-Energy Lithium-Ion Batteries. *Angewandte Chemie - International Edition* **60**, 2208–2220 (2021).
98. Pan, H. *et al.* Li- and Mn-rich layered oxide cathode materials for lithium-ion batteries: A review from fundamentals to research progress and applications. *Molecular Systems Design and Engineering* **3**, 748–803 (2018).
99. Assat, G., Iadecola, A., Delacourt, C., Dedryvère, R. & Tarascon, J. M. Decoupling Cationic-Anionic Redox Processes in a Model Li-Rich Cathode via Operando X-ray Absorption Spectroscopy. *Chem. Mater.* **29**, 9714–9724 (2017).
100. Assat, G. *et al.* Fundamental interplay between anionic/cationic redox governing the kinetics and thermodynamics of lithium-rich cathodes. *Nat. Commun.* **8**, (2017).
101. Strehle, B. *et al.* The Role of Oxygen Release from Li- and Mn-Rich Layered Oxides during the First Cycles Investigated by On-Line Electrochemical Mass Spectrometry. *J. Electrochem. Soc.* **164**, A400–A406 (2017).
102. Lee, E. S. & Manthiram, A. Smart design of lithium-rich layered oxide cathode compositions with suppressed voltage decay. *J. Mater. Chem. A* **2**, 3932–3939 (2014).
103. Li, X. *et al.* Direct Visualization of the Reversible O^{2-}/O^{-} Redox Process in Li-Rich Cathode Materials. *Adv. Mater.* **30**, (2018).
104. Buchholz, D. *et al.* X-ray Absorption Spectroscopy Investigation of Lithium-Rich, Cobalt-Poor Layered-Oxide Cathode Material with High Capacity. *ChemElectroChem* **2**, 85–97 (2015).
105. Assat, G., Delacourt, C., Corte, D. A. D. & Tarascon, J.-M. Editors' Choice—Practical Assessment of Anionic Redox in Li-Rich Layered Oxide Cathodes: A Mixed Blessing for High Energy Li-Ion Batteries. *J. Electrochem. Soc.* **163**, A2965–A2976 (2016).
106. Croy, J. R., Gallagher, K. G., Balasubramanian, M., Long, B. R. & Thackeray, M. M. Quantifying Hysteresis and Voltage Fade in $xLi_2MnO_3\bullet(1\text{-}x)LiMn_{0.5}Ni_{0.5}O_2$ Electrodes as a Function of Li_2MnO_3 Content . *J. Electrochem. Soc.* **161**, A318–A325 (2014).

107. Nayak, P. K. *et al.* Al Doping for Mitigating the Capacity Fading and Voltage Decay of Layered Li and Mn-Rich Cathodes for Li-Ion Batteries. *Adv. Energy Mater.* **6**, (2016).
108. Kumar Nayak, P. *et al.* Remarkably Improved Electrochemical Performance of Li- and Mn-Rich Cathodes upon Substitution of Mn with Ni. *ACS Applied Materials and Interfaces* **9**, 4309–4319 (2017).
109. Zuo, W. *et al.* Li-rich cathodes for rechargeable Li-based batteries: Reaction mechanisms and advanced characterization techniques. *Energy and Environmental Science* **13**, 4450–4497 (2020).
110. Ji, X. *et al.* A review on progress of lithium-rich manganese-based cathodes for lithium ion batteries. *Journal of Power Sources* **487**, (2021).
111. Zheng, J. *et al.* Li- and Mn-Rich Cathode Materials: Challenges to Commercialization. *Advanced Energy Materials* **7**, (2017).
112. Bao, L. *et al.* The Effects of Trace Yb Doping on the Electrochemical Performance of Li-Rich Layered Oxides. *ChemSusChem* **12**, 2294–2301 (2019).
113. Kou, Y., Han, E., Zhu, L. Z., Liu, L. & Zhang, Z. The effect of Ti doping on electrochemical properties of $Li_{1.167}Ni_{0.4}Mn_{0.383}Co_{0.05}O_2$ for lithium-ion batteries. *Solid State Ionics* **296**, 154–157 (2016).
114. Zhang, H. Z., Qiao, Q. Q., Li, G. R. & Gao, X. P. PO_4^{3-} polyanion-doping for stabilizing Li-rich layered oxides as cathode materials for advanced lithium-ion batteries. *J. Mater. Chem. A* **2**, 7454–7460 (2014).
115. Wang, Y. *et al.* Suppressing Mn Reduction of Li-Rich Mn-Based Cathodes by F-Doping for Advanced Lithium-Ion Batteries. *J. Phys. Chem. C* **122**, 27836–27842 (2018).
116. Liu, J. & Manthiram, A. Functional surface modifications of a high capacity layered $Li[Li_{0.2}Mn_{0.54}Ni_{0.13}Co_{0.13}]O_2$ cathode. *J. Mater. Chem.* **20**, 3961–3967 (2010).
117. Wei, H. *et al.* Lithium-rich manganese-based cathode materials with highly stable lattice and surface enabled by perovskite-type phase-compatible layer. *Nano Energy* **88**, 106288 (2021).
118. Wang, T., Huang, Z., Cai, M. & Shi, S. High performance lithium-rich cathode modified with Al_2O_3 by melting impregnation method. *Mater. Lett.* **279**, (2020).
119. Ma, G. *et al.* A General and Mild Approach to Controllable Preparation of Manganese-Based Micro- and Nanostructured Bars for High Performance Lithium-Ion Batteries.

Angew. Chemie **128**, 3731–3735 (2016).

120. Li, J. *et al.* Tris(trimethylsilyl)borate as an electrolyte additive for improving interfacial stability of high voltage layered lithium-rich oxide cathode/carbonate-based electrolyte. *J. Power Sources* **285**, 360–366 (2015).
121. Wang, L. *et al.* Influence of fluoroethylene carbonate as co-solvent on the high-voltage performance of $LiNi_{1/3}Co_{1/3}Mn_{1/3}O_2$ cathode for lithium-ion batteries. *Electrochim. Acta* **191**, 8–15 (2016).
122. Li, H. F., Sun, G. B., Wang, Q., Sun, L. N. & Jiang, F. Bin. Improving Safe Properties of PIR13TFSI Based Electrolyte for High-Voltage Graphite/$Li[Li_{0.2}Mn_{0.54}Ni_{0.13}Co_{0.13}]O_2$ Battery. *Adv. Mater. Res.* **1094**, 209–213 (2015).
123. Lee, S. J. *et al.* Effect of Lithium Bis(oxalato)borate Additive on Electrochemical Performance of $Li_{1.17}Ni_{0.17}Mn_{0.5}Co_{0.17}O_2$ Cathodes for Lithium-Ion Batteries . *J. Electrochem. Soc.* **161**, A2012–A2019 (2014).
124. Nayak, P. K., Grinblat, J., Levi, M. & Aurbach, D. Understanding the Effect of Lithium Bis(oxalato) Borate (LiBOB) on the Structural and Electrochemical Aging of Li and Mn Rich High Capacity $Li_{1.2}Ni_{0.16}Mn_{0.56}Co_{0.08}O_2$ Cathodes. *J. Electrochem. Soc.* **162**, A596–A602 (2015).
125. Zhao, J. *et al.* Interphase Engineering by Electrolyte Additives for Lithium-Rich Layered Oxides: Advances and Perspectives. *ACS Energy Letters* **6**, 2552–2564 (2021).
126. Wu, F. *et al.* A novel phosphonium ionic liquid electrolyte enabling high-voltage and high-energy positive electrode materials in lithium-metal batteries. *Energy Storage Mater.* **42**, 826–835 (2021).
127. Brutti, S. *et al.* Ionic liquid electrolytes for high-voltage, lithium-ion batteries. *J. Power Sources* **479**, (2020).

2 DOPING AND COBALT REPLACEMENT OF LRLO

The aim of chapter 2 is the study of the effect of doping and the simultaneous reduction of cobalt content in LRLOs. The replacement was studied step by step and co-doping by Li (over-lithiation) and Al or Mn was proved to be an excellent strategy to reduce Co and obtain very high electrochemical performance.

2.1 INTRODUCTION

In the last 20 years research efforts have been made about new layered materials, in order to overcome the limits of $LiCoO_2$[1]. Multimetal systems[2,3], combining the features of Nickel, Cobalt and Manganese, have been explored, such as $LiNi_xMn_{1-x}O_2$, $Li[Ni_{1/3}Mn_{1/3}Co_{1/3}]O_2$ or $Li[Ni_xCo_yAl_{1-x-y}]O_2$[4,5]. However, their specific capacity and electrochemical stability are still not enough to satisfy the growing energy demand of power application (e.g. vehicles). Recently, lithium-rich transition metal oxides (LRLOs) have been widely explored as alternative cathode materials thanks to their high operating voltage and large specific capacity, exceeding 200 $mAhg^{-1}$ [6,7]. Lithium-rich materials have a complex layered structure. Two different hypothesis have been proposed to describe this kind of structures: a nanocomposite[8], $xLi_2MnO_3 \cdot (1-x)LiNi_aCo_bMn_cO_2$, or single phase solid solution[9], $Li_{(1+x)}M_{(1-x)}O_2$ (where M = Ni, Mn and Co). LRLOs work in the range 2-4.8 V vs Li and the large capacity observed during the first delithiation is attributed only partly to the oxidation of Co and Ni, but the majority of the exchanged charge is associated with the activation of the "Li_2MnO_3" component[10,11]. Nevertheless, large irreversible capacity loss in the first cycle, poor rate capability, mean working potential decay upon cycling and cobalt content are still major drawbacks that are hindering commercialization[12]. Several efforts to reduce these problems have been made, including the development of different synthetic strategies, doping[13,14] and surface modification[15]. The most, widely explored, chemical strategy to mitigate the voltage decay and structural degradation in LRLO is the optimization of the transition metal blend. As an example, incorporation of redox inactive metals, such as Al, Zr, Ti, has been proposed in order to stabilize the lattice[16–18] as well as the partial replacement of lithium ions with other alkali cations, e.g. K and Na[19]; or doping the oxygen anion sublattice[20].

In order to make these materials up scalable to industrial production it is also important to consider the reduction of costs and the toxicity of raw materials, in particular cobalt[21,22]. Cobalt reduction has been identified as major driver to improve the environmental benignity of batteries and the sustainability of the overall production-consumption-recycling lifecycle[23,24]. Furthermore, cobalt is a strategic commodity traded with rising prices on the international markets and therefore its minimization in a battery formulation substantially leads to the reduction of energy storage costs, in terms of $ Wh^{-1} Kg^{-1} [21,22].

This chapter illustrates our approach in the realization of a new class of doped Lithium Rich layered oxide materials. In particular, here we focus on the reduction of Cobalt content, by investigating step by step the modifications on the chemical-physical and electrochemical properties of synthetized samples. In the first section, we study the impact of Al introduction within the structure. We synthetized and characterized a set of materials with general formula $Li_{1.2}Mn_{0.54}Ni_{0.13}Co_{0.13-x}Al_xO_2$, x=0.03, 0.06, 0.09, and, once found the best compromise between Al amount and electrochemical performance, we further replaced cobalt with other metals, in particular Mn, Ni and Li. The doping with Li, called over-lihiation in the chapter, and the co-doping with Al seem to reduce the drawbacks by stabilizing the performance compared to Co-rich phases. Finally, the last section is devoted to the investigation of the over-lithiation and Mn-doping to obtain a Co-free material. Here we demonstrate that Mn can be used in the place of Al which is electrochemically inactive.

The chapter presents an extensive characterization of samples, using X-Ray diffraction, Scanning electron Microscopy, Transmission Electron Microscopy, X-Ray Absorption Spectroscopy, X-Ray Photoelectron Spectroscopy and Raman Spectroscopy. Electrochemical properties have been evaluated by Galvanostatic cycling and Cyclic Voltammetry.

2.2 MATERIALS AND METHODS

Synthesis: $Li_{1.2+x}Mn_{0.54}Ni_{0.13}Co_{0.13-x-y}Al_yO_2$ was synthesized by sol-gel method. Basically, stoichiometric amount of $Mn(CH_3COO)_2{\cdot}4H_2O$ (manganese (II) acetate tetrahydrate, Sigma-Aldrich), $Ni(CH_3COO)_2{\cdot}4H_2O$ (Nickel (II) acetate tetrahydrate, Sigma-Aldrich), $Co(CH_3COO)_2{\cdot}4H_2O$ (Cobalt (II) acetate tetrahydrate, Sigma-Aldrich), $(HO)_2Al(CH_3COO)$ (Aluminum acetate dibasic, Sigma-Aldrich) and 5% excess $LiCH_3COO{\cdot}2H_2O$ (lithium acetate

dihydrate, Sigma-Aldrich) were dissolved in ultrapure water. An aqueous solution of $C_2H_2O_4$ (oxalic acid, Sigma-Aldrich) around 0.38 M, acting as chelating agent, was added to the metal-acetate solution in order to have chelating agent/metals molar ratio of 1.5/1 and left under stirring. The pH in the mixture was kept at 8 by the addition of ammonia solution (NH_4OH 32%, Sigma-Aldrich) dropwise. Then, the solution was heated at 80 °C in an oil bath to form a gel. The as obtained gel was finally completely dried at 200° C, calcined at 450°C for 2 hours and at 900°C for 12 hours.

*Materials Characterization***:** The composition of the materials was confirmed by inductively coupled plasma optical emission spectrometry (ICP-OES) analysis, carried out on an iCAP 7600 DUO Thermo Fisher Scientific. The structure was characterized by XRD using a Malvern PANalytical Empyrean with Cu Kα radiation source in the range of 2θ degree of 10°−90°. Deeper structural analysis has been performed by synchrotron diffraction, carried out at Elettra MCX beamline using a wavelength of 1.2 Å (~10 KeV) in the range between $10° \leq 2\theta \leq 90°$. Diffractograms were analyzed by Rietveld Refinement program GSAS-II[25].

Morphology and composition of the materials were investigated by a JEOL JSM-7500FA scanning electron microscope (SEM), with a cold-field emission gun, equipped with an energy-dispersive X-ray spectroscopy (EDX) system based on an Oxford X-Max silicon-drift detector (80 mm^2 active area).

X-ray absorption spectra at the Mn and Ni K-edges were measured in the transmission mode at the XAFS beamline of the ELETTRA synchrotron radiation facility. A Si(111) double crystal monochromator with an energy resolution of 0.8 eV at 7 keV was used. The intensity of the monochromatic X-ray beam was measured by three consecutive ionization chambers (Oxford) filled with suitable gas mixtures. Pelletized samples using polyethylene as dispersing agent was placed in an evacuated sample chamber: the homogeneity of pellets have been checked before running the experiment. Reference spectra on Mn_2O_3 (Sigma Aldrich, 99%), MnO_2 (Sigma Aldrich, 99%) NiO (Sigma Aldrich, 99%) and $LiNiO_2$ (synthesized from a stoichiometric mixture of Li_2O and NiO at 700°C for 12 h in air and checked by XRD) have been recorded as well in the same experimental conditions.

XANES spectra have been analyzed and fitted using the Athena XAS data processing software. X-Ray absorption spectra at the Mn, Ni and Co L-edges have been measured at the advanced photoelectric effect high-energy (APE-HE) beamline at the ELETTRA synchrotron radiation

source. The XANES spectra have been acquired using the Total Electron Yield (TEY) detection mode, allowing a probing depth of ~ 5 nm. The energy resolution of these spectra is about 0.1 eV. The samples, in the form of powders, have been glued on the sample holder using conductive silver paste and then loaded on the manipulator of the APE-HE chamber (in UHV conditions). The sample was oriented at 45° with respect to the incident beam, probing an area of ≈150 μm^2. X-ray photoemission spectra of the samples were performed exploiting a conventional non monochromatized X-Ray source (Mg Kα= 1254 eV) with a hemispherical electron energy analyzer, in a dedicated chamber of the NFFA UHV MBE-cluster system. Also in this case, the powders were glued on the sample holder using a conductive silver paste. The samples were positioned at 45°with respect to the incident beam, probing an area of ≈1 mm^2 and a depth of ≈1 nm. The Mn 2p spectra have been acquired using a pass energy of 50 and a dwell time of 2000 ms; they have been aligned using the Au VB spectra of a reference Au foil positioned just above the sample. Raman spectroscopy was carried out using a Dilor Labram instrument equipped with a He-Ne laser source at 632.7 nm and a CCD cooled detector and Si as calibrating standard for the energy scale. Micrographs of the electrodes before and after cycling were acquired by a Zeiss Auriga Field Emission High Resolution Scanning Electron Microscope.

Electrochemical Characterization: Electrochemical charge-discharge data were acquired assembling Al-coated CR2032 coin cells and using a voltage of 2 and 4.8 V. Working electrodes were prepared by mixing the active material (80 wt.%), Super P Carbon (10 wt.%), and polyvinylidine fluoride (PVDF) binder (10 wt.%); the powder slurry, obtained by the addition of N-methyl pyrrolidinone, was casted onto an aluminum current collector and cut into electrodes of 10 mm diameter with a mass loading of 2-2.2 mg/cm. The coin cells were assembled in an argon-filled glovebox, with metallic lithium disks as counter electrode (Sigma Aldrich). The electrolyte solution was 1M Lithium hexafluorophosphate in Ethylene Carbonate:Dimethyl Carbonate (1:1 vol.%, Solvionic). A Biologic BCS-805 battery cycler was used for electrochemical tests. Cyclic voltammograms curves were measured using a Biologic VMP3 multichannel potentiostat in a potential range of 2.0 V to 5 V at a scan rate of 0.5 mV s^{-1}. Complete lithium-ion cells were assembled using graphite (PI-KEM) as negative electrode and tested using a MACCOR S4300 system in a voltage range from 2.2 to 4.7 V using a current density of 230 $mAg^{-1}$for 300 cycles. The balance between anode and cathode was done considering the full initial capacity of graphite; the cathode/anode mass ratio was set at 1.75.

2.3 OVER-LITHIATED ALUMINUM DOPED SAMPLES

2.3.1 Effect of Al doping

In order to evaluate the effect of the substitution of cobalt with aluminum into the $Li_{1.2}Mn_{0.54}Ni_{0.13}Co_{0.13}O_2$ structure, 3 materials with general formula $Li_{1.2}Mn_{0.54}Ni_{0.13}Co_{0.13-x}Al_xO_2$ where x=0, 0.03, 0.06, 0.09 (samples S01-S04) were synthetized and characterized in terms of structure and electrochemical properties.

Before any characterization, all samples were analyzed by OES-ICP to verify their chemical composition. As can be seen from table 2.1, the actual compositions are very close to the nominal compositions.

Table 2.1: The chemical compositions of the obtained samples examined by ICP-OES analysis.

Formula			Li	Mn	Co	Ni	Al
S01	$Li_{1.2}Mn_{0.54}Ni_{0.13}Co_{0.13}O_2$	**Theoretical**	1.20	0.540	0.130	0.130	/
		Actual	1.21	0.504	0.101	0.131	/
S02	$Li_{1.2}Mn_{0.54}Ni_{0.13}Co_{0.1}Al_{0.03}O_2$	**Theoretical**	1.20	0.540	0.100	0.130	0.030
		Actual	1.20	0.531	0.108	0.131	0.031
S03	$Li_{1.2}Mn_{0.54}Ni_{0.13}Co_{0.07}Al_{0.06}O_2$	**Theoretical**	1.20	0.540	0.070	0.130	0.060
		Actual	1.18	0.566	0.080	0.138	0.051
S04	$Li_{1.2}Mn_{0.54}Ni_{0.13}Co_{0.04}Al_{0.09}O_2$	**Theoretical**	1.20	0.540	0.040	0.130	0.090
		Actual	1.2	0.542	0.044	0.133	0.082

The experimental XRD patterns obtained for the synthesized samples are shown in figure 1.1. The diffraction patterns show crystalline samples with no particular differences. All the peaks, except for some extra peaks observed between 20° and 30°, could be indexed with an rhombohedral cell[26], space group R-3m, according to the reference pattern (PDF: 04-013-4592) also shown in figure 1.1. The appearance of these extra peaks between 20°-30° can be explained considering an ordering between Li, Mn, Co and Ni in the transition metals planes, similar to the structural ordering in the monoclinic Li_2MnO_3[27,28] (see reference pattern PDF 01-085-6632).

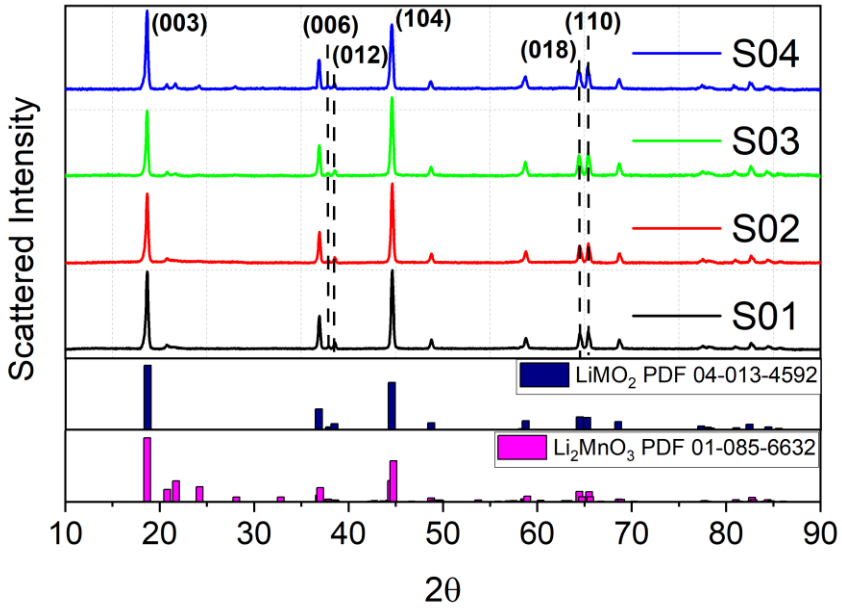

Figure 1.1: XRD pattern of $Li_{1.2}Mn_{0.54}Ni_{0.13}Co_{0.13-x}Al_xO_2$ series.

Moreover, taking a careful look of the patterns, it can be found that the (006)/(012) and (018)/(110) peaks are well split, confirming a well-defined layered structure, and that a higher (003) peak can be observed over the (104) peak in each sample. The intensity ratio between (003) and (104) peaks can be used as a measure of the degree of cation mixing in the layered: the higher the ratio, the lower is the cation mixing. Therefore, the aluminum doping does not change the crystal structure or cause impurity phases and retain the layered structure. Moreover, the (003) peak actually shifts slightly to a smaller angle when the Al amount increases, indicating the success of doping within the structure.

Regarding the morphology, scanning electron micrographs are shown in figure 2.2. The micrographs indicate that all samples consist of particles with a size distribution in the range of 200-400 nm. The particles appear fused together, in particular for doped materials, to form agglomerates.

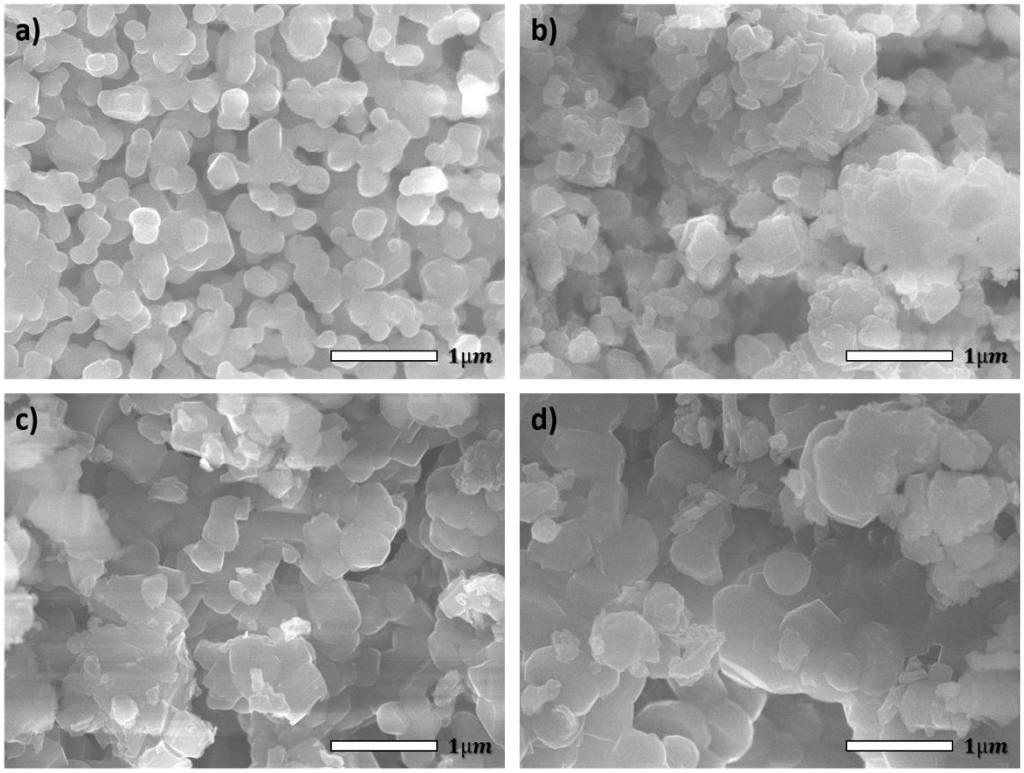

Figure 2.1: SEM images of a)S01, b)S02, c)S03 and d)S04.

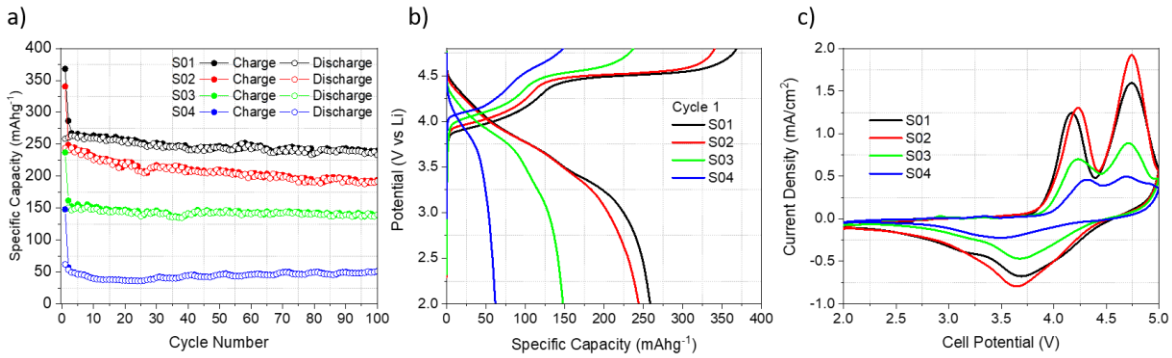

Figure 2.3: Electrochemical characterization of $Li_{1.2}Mn_{0.54}Ni_{0.13}Co_{0.13-x}Al_xO_2$ series. a) Specific capacity vs cycle number. b) First potential profile. c) Cyclic voltammetry.

To investigate if the presence of Al has an impact on the electrochemical performance, all samples have been tested in lithium half cells and the results are shown in figure 2.3.

Looking at the cycling performance in figure 2.3a, it is evident that the replacement of the cobalt by Al leads to a marked decrease in the specific capacity. Regarding the performance of the sample without any doping (S01), it reaches a specific capacity of 368 $mAhg^{-1}$during the first charge and, then, is able to exchange 260 $mAhg^{-1}$during the first discharge. Finally, its capacity decreases to

233 $mAhg^{-1}$ after 100 cycles. All doped materials exhibit smaller specific capacity (Cap) following the order $Cap_{S02} > Cap_{S03} > Cap_{S04}$, obtaining respectively at the end of first charge 341, 237 and 148 $mAhg^{-1}$. The introduction of a small quantity of Al into the structure slightly decreases the electrochemical performance. However, when the Al replaces half of the Cobalt in the pristine material, the performance drops quickly. In fact, the specific capacities at the end of the first cycle are 243, 148 and 61 $mAhg^{-1}$ for S02, S03 and S04. After 100 cycles, the discharge capacities are 191, 139, 49 $mAhg^{-1}$ for S02, S03 and S04. Therefore, S03 and S04 show a stable performance during the test but the specific capacities are unsatisfactory.

In figure 2.3b, we show the potential profiles obtained for the 4 samples in the first charge/discharge cycle. During the initial charge, the voltage gradually increases up to 4.4V with a sloping profile in which the Co and Ni are oxidized[29] and, then, a plateau begins in which the extra lithium ions are removed from the lattice by the oxidation of O^{2-} [30,31]. It is interesting to notice that all samples show a similar profile. Due to the addition of aluminum and the reduced amount of cobalt all the processes are shorter, thus the overall specific capacities are smaller. During the first discharge, the voltage decreases down to 2V without any plateau, confirming the irreversibility of the oxygen redox within these structures.

Cyclic voltammetries have been performed to investigate the electrochemical process. The graph in figure 2.3c shows the first cycle in which, during the first anodic scan, we can observe two peaks around 4.2 and 4.7 V. The peak at lower voltage can be associated with the oxidation of Ni^{2+} to Ni^{4+} and Co^{3+} to Co^{4+}, whereas the one at higher voltage can be attributed to the anionic redox reaction of oxygen[32]. The main difference between the samples is the intensity of the peak around 4.7V, associated to the oxygen redox. The decrease of this high voltage process is induced by the removal of cobalt: in fact The O^{2-}/O^{-} arises from a bonding band originated by the overlap of the Co t_{2g} band and the O^{2-} 2p band[33,34].

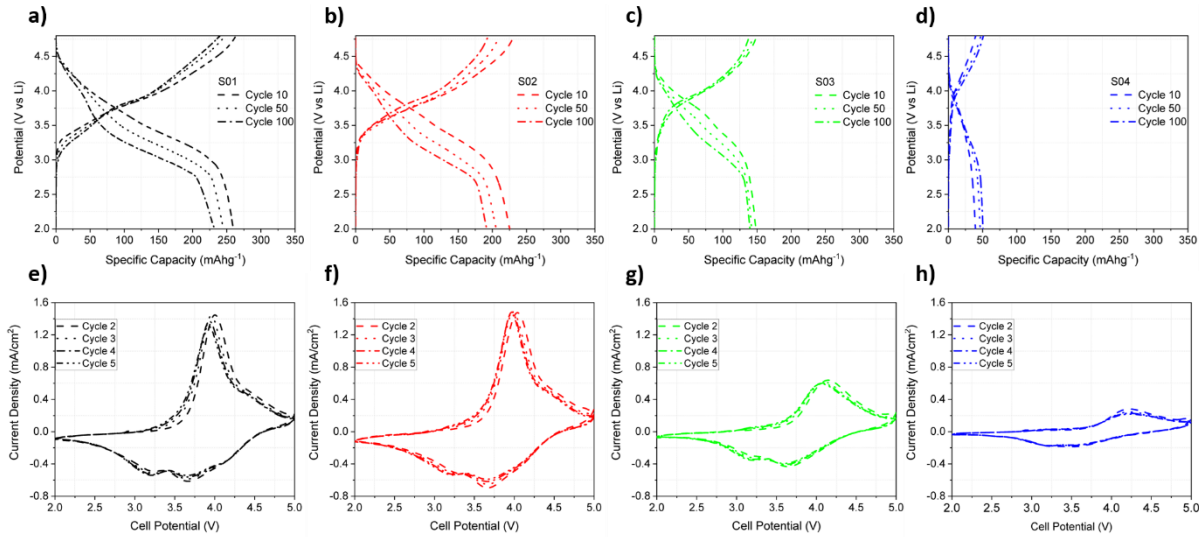

Figure 2.4: a-d) Potential profile of S01, S02, S03 and S04. e-h) Cyclic voltammetries S01, S02, S03 and S04.

Selected potential profiles are reported in the figure 2.4 for all samples. Figures 2.4a-d report a plot of the changes in voltage as a function of capacity under constant current and, in general, show a slope both in charge and in discharge. Changes in the potential profiles could give some information about changes in the redox mechanism because the curves shape is influenced by the reactions occurring within the cell. It can be noted the absence of plateau after the first cycles and a monotonic shift of the potential profiles towards lower voltages upon cycling. The doping with Al seems to stabilize this phenomenon, despite the drop in the specific capacities. In figure 2.4e-h, we can see the cyclic voltammetry cycles after the first cycle. In the anodic scan, only one peak around 3.8V can be observed, in agreement with the galvanostatic cycling. On the contrary, in the cathodic scan, an additional electroactive process around 3.1V can be observed, associated to the redox couple Mn^{4+}/Mn^{3+}.

The electrochemical characterization suggests that the optimal content of Al is between 0.03-0.05, in fact the performance drop for larger Al doping.

2.3.2 Further replacing of Co by Mn, Ni or Li

The analysis reported above reveals that a larger substitution of cobalt with aluminum leads to a remarkable decrease of performance in lithium cells. Nevertheless, the doping with small amount of aluminum, *i.e.* when x=0.03, seems to mitigate the voltage decay responsible of the capacity drop upon cycling. For this reason, we further modify the S02 sample, decreasing the amount of cobalt by the addition of Mn, Ni or Li. Table 2.2 reports the 3 obtained samples.

According to elemental analysis by ICP-OES technique, the compositions of the materials are very close to the targeted compositions. The elemental analysis results are given in table 2.2.

Table 2.2: The chemical compositions of the obtained samples examined by ICP-OES analysis.

Formula			Li	Mn	Co	Ni	Al
S05	$Li_{1.2}Mn_{0.57}Ni_{0.13}Co_{0.07}Al_{0.03}O_2$	**Theoretical**	1.20	0.570	0.070	0.130	0.030
		Actual	1.20	0.563	0.076	0.125	0.027
S06	$Li_{1.2}Mn_{0.54}Ni_{0.16}Co_{0.07}Al_{0.03}O_2$	**Theoretical**	1.20	0.540	0.070	0.160	0.030
		Actual	1.19	0.521	0.078	0.155	0.028
S07	$Li_{1.23}Mn_{0.54}Ni_{0.13}Co_{0.07}Al_{0.03}O_2$	**Theoretical**	1.23	0.540	0.070	0.130	0.030
		Actual	1.22	0.512	0.056	0.129	0.028

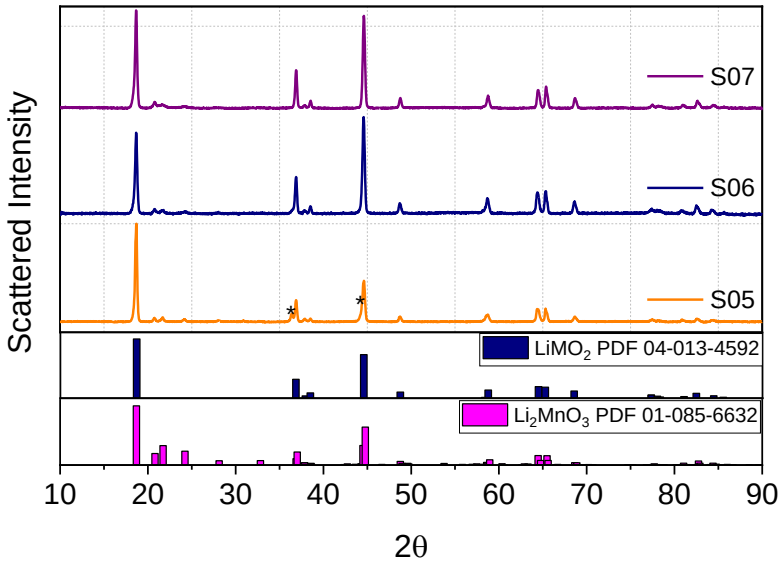

Figure 2.5: XRD pattern of S05, S06 and S07.

X-Ray diffraction patterns are shown in figure 2.5. All sample patterns match the R-3m space group, except for the weak diffraction peaks at 2θ values between 21° and 25°. As mentioned before, these peaks are due to the Li_2MnO_3 phase and indicate a super lattice ordering of Li and TM in the transition metal layers. Only S05 pattern shows traces of impurities, indicated with asterisks.

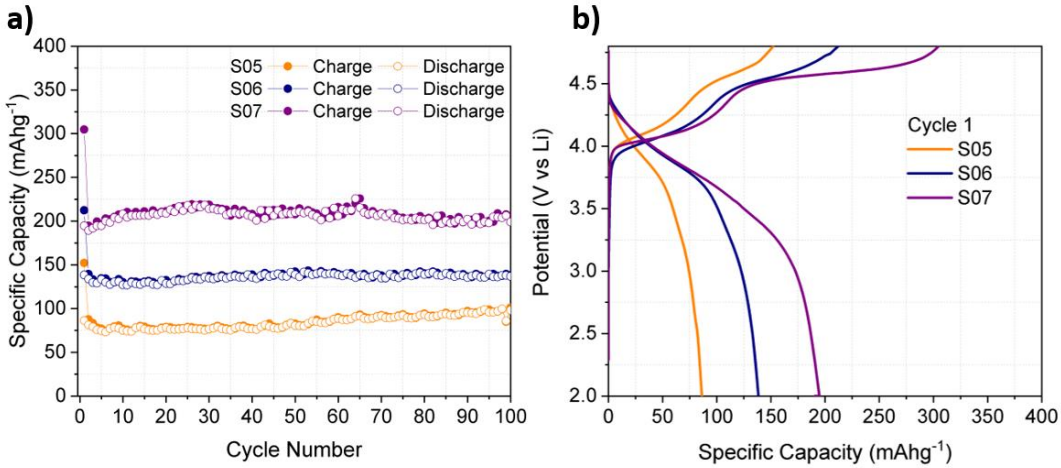

Figure 2.6 a) Charge-Discharge test and b) first potential profile of S05, S06 and S07.

The samples have been tested by galvanostatic cycling in lithium half-cell between 2 and 4.8V at a current of ≈40 mA/g (C/10). Figure 2.6 displays the specific capacity vs cycle number (a) and the first potential profile (b) for S05, S06 and S07. The first charge potential profiles consist of a slope up to 4.4V and a subsequent plateau. This plateau disappears during the discharge step due to the irreversibility of the oxygen redox, in line with all S01-S04 samples. Despite the same amount of Co, the plateau is shorter for S05 and S06 with respect sample S07. In fact, the specific capacities at the end of the first charge are 152.2, 212.3 and 304.8 $mAhg^{-1}$, respectively for S05, S06 and S07. After the first cycle, only the sample S07 has a high capacity of 194.7 $mAhg^{-1}$, while samples S05 and S06 suffer poor electrochemical performance. Furthermore, S07 sample exhibits a slightly activated specific capacity trend, reaching a capacity value of 199 $mAhg^{-1}$ after 100 cycles, while the capacities for S05 and S06 are 98.1 and 136.9, respectively. As expected, also in this case we observed the deterioration of the electrochemical performance as consequence of the reduction of cobalt content. However, the S07 sample, $Li_{1.23}Mn_{0.54}Ni_{0.13}Co_{0.07}Al_{0.03}O_2$, still maintains high capacity values (>200 $mAhg^{-1}$) and good cycle life stability. This suggests that the

over-lithiation to replace the Co can be a viable way to preserve high performance despite the smaller content of cobalt.

2.3.3 Strategy of over-lithiation

Once identified the optimal concentration range for aluminum in the section 2.3.1 and proved that lithium substitution is a valuable way to replace cobalt in the section 2.3.2 preserving performance, we synthetized a new series of lithium-rich materials in which the cobalt was partially replaced by growing amount of lithium. All the stoichiometries explored in this thesis are reported in table 2.3 with the elemental composition analyzed by ICP-OES. According to the elemental analysis, the composition of the materials is very close to the theoretical one.

Table 2.3: The chemical compositions of the obtained samples examined by ICP-OES analysis.

Formula			Li	Mn	Co	Ni	Al
S08	$Li_{1.26}Mn_{0.54}Ni_{0.13}Co_{0.04}Al_{0.03}O_2$	**Theoretical**	1.26	0.540	0.040	0.130	0.030
		Actual	1.24	0.545	0.036	0.136	0.030
S09	$Li_{1.26}Mn_{0.54}Ni_{0.13}Co_{0.02}Al_{0.05}O_2$	**Theoretical**	1.26	0.540	0.020	0.130	0.050
		Actual	1.28	0.523	0.023	0.13	0.047
S10	$Li_{1.28}Mn_{0.54}Ni_{0.13}Co_{0.02}Al_{0.03}O_2$	**Theoretical**	1.28	0.540	0.020	0.130	0.030
		Actual	1.25	0.548	0.024	0.132	0.031

All structures were checked by Synchrotron X-Ray diffraction and results are shown in figure 2.7, where S01 was added for comparison. All doped materials are crystalline and the diffraction lines appear sharp and intense. No differences can be highlighted compared to S01; in fact, the main phase consists of the rhombohedral phase (space group R-3m) and additional peaks are again visible between 2θ of 16°-25°, corresponding to the monoclinic phase with space group C2/m. The replacement of cobalt by the increase of Li beyond 1.2 and the introduction of Al doesn't change the patterns, indicating that the crystal structures are almost the same without segregation of other phases. The collected patterns have been analysed by Rietveld refinement to obtain further information. The analysis has been carried out using a R-3m unit cell. The detailed Rietveld refinement results are shown in figure 2.8 while the lattice parameter values are compared in figure 2.9.

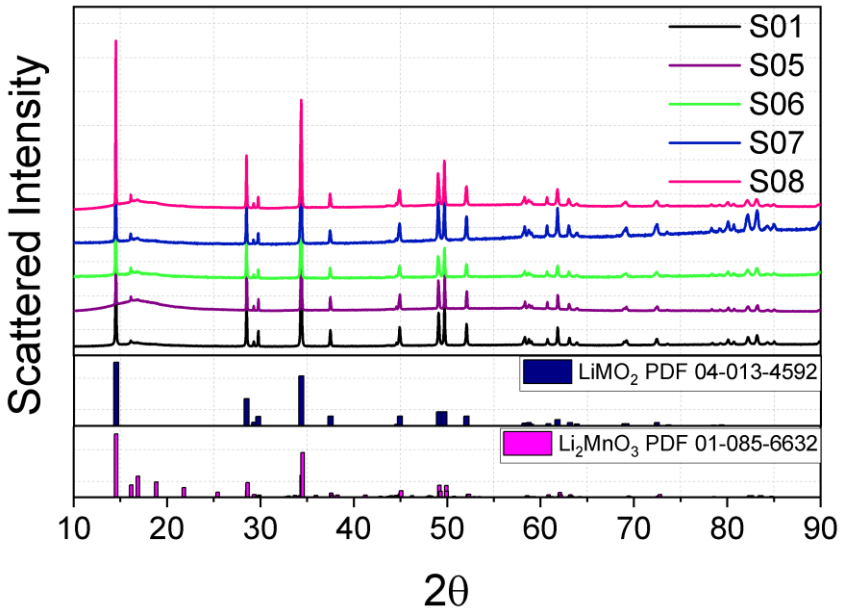

Figure: 2.7 XRD patterns of $Li_{1.23}Mn_{0.54}Ni_{0.13}Co_{0.07}Al_{0.03}O_2$ (Purple line), $Li_{1.26}Mn_{0.54}Ni_{0.13}Co_{0.04}Al_{0.03}O_2$ (Dark Cyan line), $Li_{1.26}Mn_{0.54}Ni_{0.13}Co_{0.02}Al_{0.05}O_2$ (Olive line) and $Li_{1.28}Mn_{0.54}Ni_{0.13}Co_{0.02}Al_{0.03}O_2$ (Orange line). S01 is added for comparison.

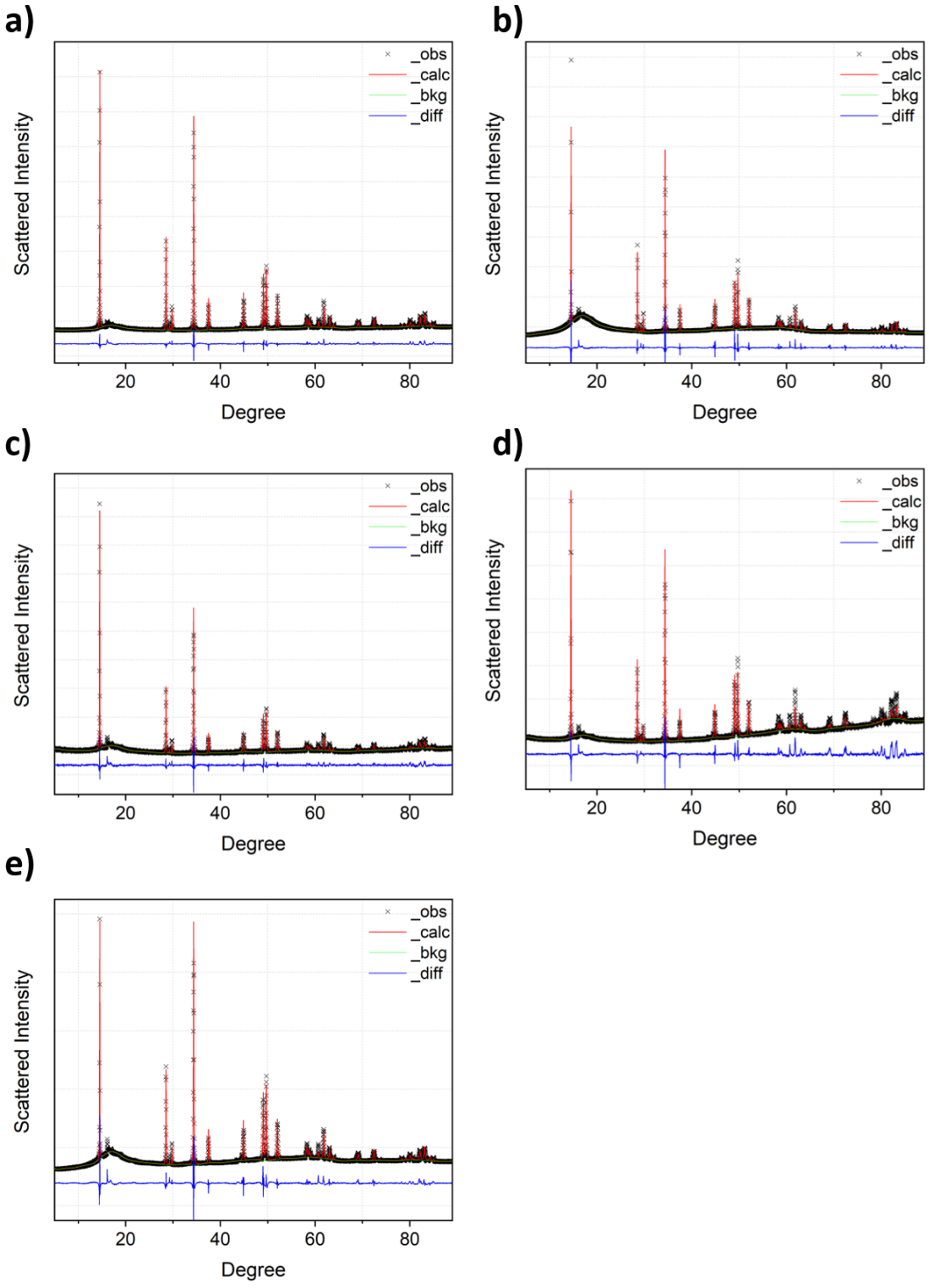

Figure 2.8: Rietveld Refinement of a) S01, b) S07, c) S08, d) S09 and e) S10.

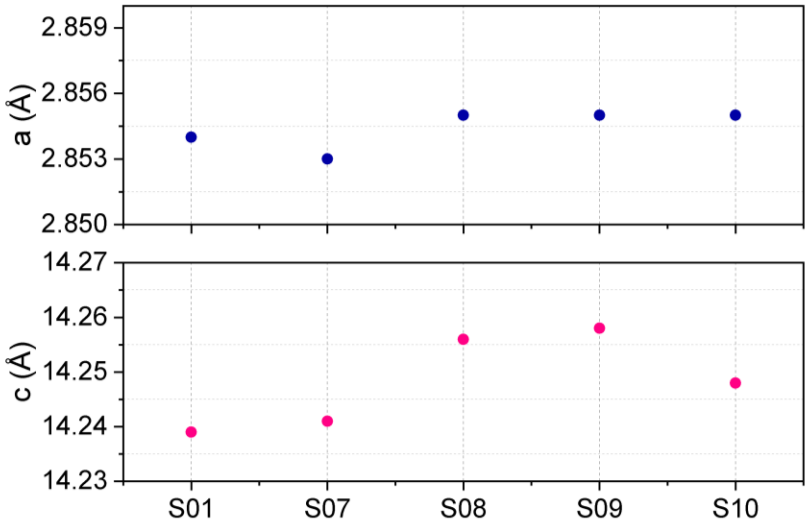

Figure 2.9: Lattice parameters of S01, S07, S08, S09 and S10.

In general, the lattice parameters increase along the series, mainly, due to the substitution of smaller Co^{3+} (0.54 Å) ions for bigger Li^{+} (0.76 Å) ions[35].

Lithium doping expands the cell mainly along the direction c, in fact the parameter *a* seems to have limited changes unlike the parameter *c*. All changes in the lattice parameters suggest that Li and Al have been incorporated into the structure and, probably, the expansion of the cell can alter the diffusion of Li^{+} within the structure during the electrochemical activity.

Turning to morphology, scanning electron microscopies are presented in figure 2.10. All samples, including S01, consist of particles with a size distribution in the range of 200-400 nm. The particles appear fused together, in particular for doped materials, to form agglomerates. From EDX maps, the Al has been detected in S07, S08, S09 and S10 samples and the distribution of elements is homogenous throughout, EDX maps of S07 sample are reported in figure 2.11 as an example. The metals signals are uniformly dotted in the entire particles, suggesting that no metals segregation occur.

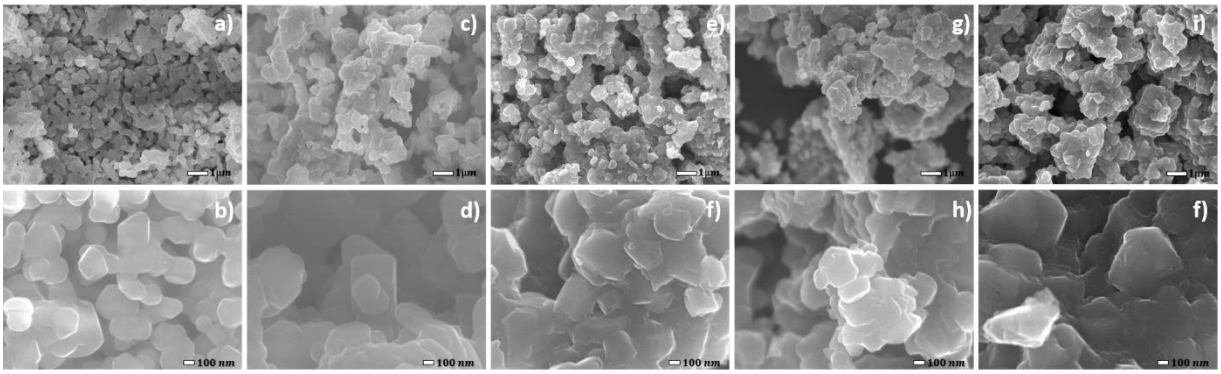

Figure 2.10: SEM images of a-b) S01, c-d) S07, e-f) S08, g-h) S09 and i-f) S10.

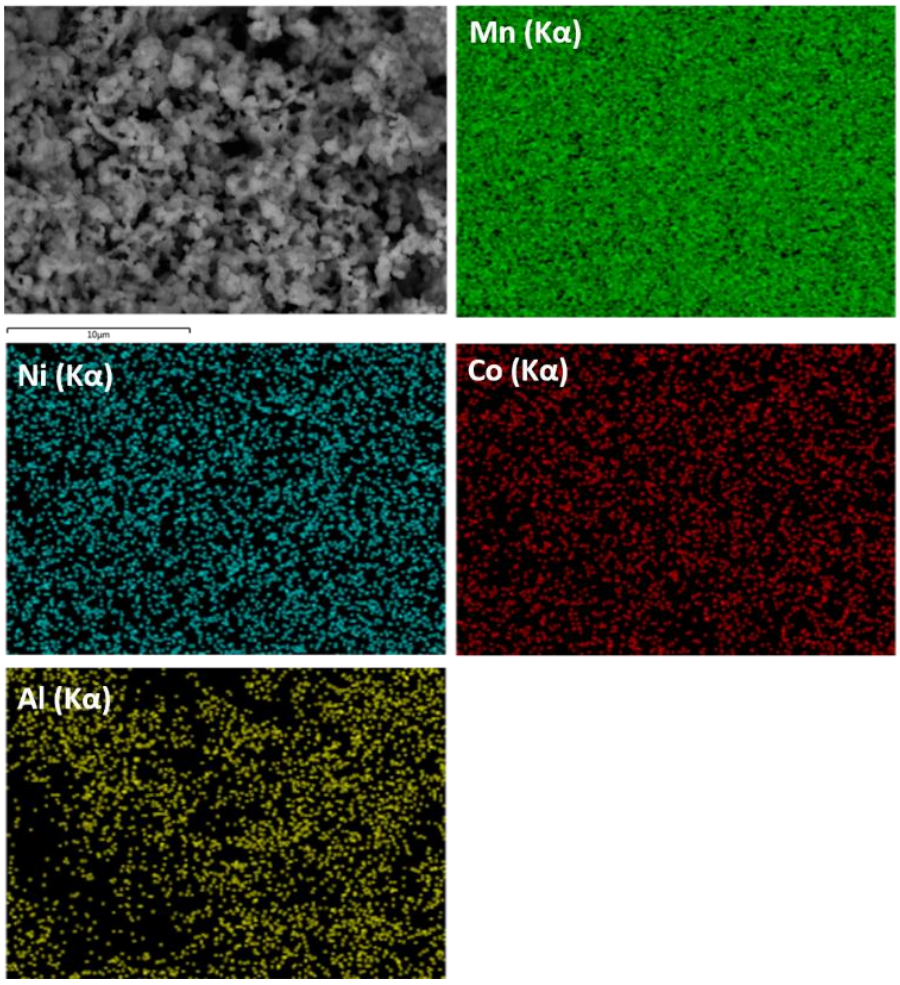

Figure 2.11: EDX maps of S07.

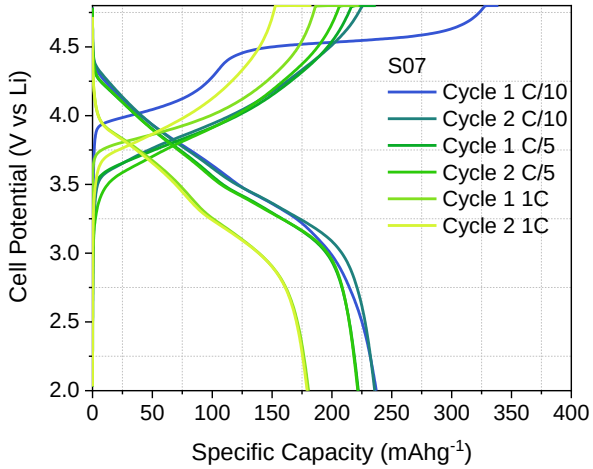

Figure 2.12: Activation potential profile of S07 sample.

All materials have been tested in lithium half cells to investigate their electrochemical properties. All electrodes have been activated following a standard procedure consisting of galvanostatic steps at C/10-C/5-1C (1C=377 mAg^{-1}) between 2-4.8V with potentiostatic steps at 4.8V using a current cut-off of C/20. The procedure can be used in order to provide a more stable cathode electrolyte interphase layer (at high potential) and prevent the consumption of electrolyte and lithium ions.

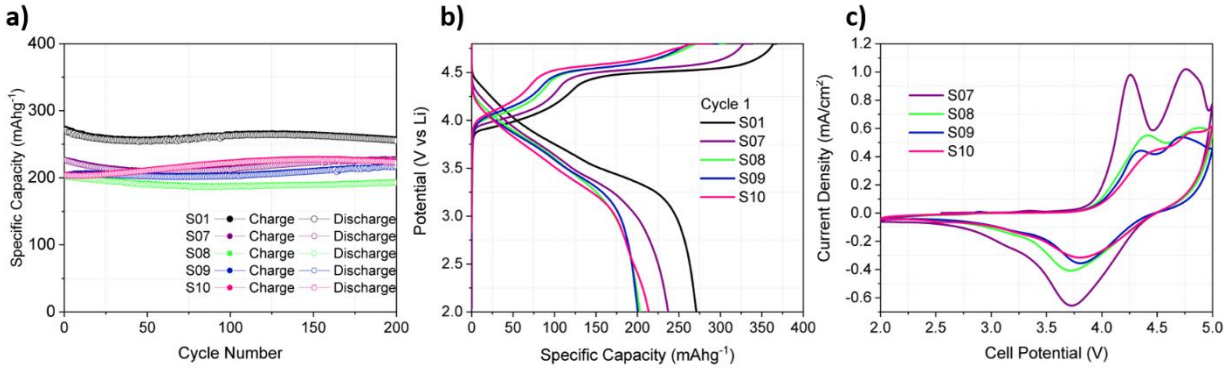

Figure 2.13: Electrochemical characterization of $Li_{1.2+x}Mn_{0.54}Ni_{0.13}Co_{0.13-x-y}Al_yO_2$ series.

The typical activation voltage profile is shown for S07 material in figure 2.12 as an example. In figure 2.13 we report the galvanostatic cycling tests carried out for all samples, where the sample S01 is added as a benchmark. The amount of cobalt has been significantly reduced along the series, nevertheless, the electrochemical performance are very promising. In fact, during the first discharge, the samples are able to deliver a specific capacity of 226, 203, 205 and 204 $mAhg^{-1}$,

respectively for S07, S08, S09 and S10. At the end of the galvanostatic cycling, after 200 cycles, the specific capacity is still high, 225 for S07, 193 for S08, 217 for S09 and 223 for S10.

In general, the doped materials exhibit very stable specific capacity values during the galvanostatic cycling, reaching a capacity value that exceed 200 $mAhg^{-}1$ in all cases. On the contrary, S01 is able to achieve higher specific capacity, 270 $mAhg^{-1}$ in the first discharge, but it decreases faster than the doped material until 255 $mAhg^{-1}$ after 200 cycles. In fact, for example, the capacity retention of S01 after 200 cycles is 94% but, for S07, it is beyond 99%. Figure 2.13b shows the comparison of the $Li_{1.2+x}Mn_{0.54}Ni_{0.13}Co_{0.13-x-y}Al_yO_2$ electrode potential profiles during the first cycle. All samples show the typical voltage profile already reported for this type of materials. In charge, it is possible to identify two electrochemical processes: a first slope around 3.8V followed by a long plateau at 4.5 V. The first slope accounts for the oxidation of Co^{4+}/Co^{3+} and Ni^{4+}/Ni^{2+}; while the process above 3.8 V is due to the oxidation of oxygen ions to O^- or to release of molecular oxygen, thus forming vacancies[30,31,36,37]. Compared to the benchmark, over-lithiated samples exhibit relevant differences. First of all, the first electrochemical oxidation occurs at slightly higher potentials than S01. Furthermore, a remarkable shortening to the plateau at 4.5V is observed, mostly for S08, S09 and S10. While during the discharge process, no relevant differences are underlined, apart from the specific capacities. The length of plateau in the first charge is found to be correlated to the amount of cobalt and thus the plateau decreases when the cobalt is replaced by aluminum and lithium[33,38]. The irreversibility of this high-voltage process can be clearly seen in the cyclic voltammetry (figure 2.13c). During the anodic scan, active materials show two oxidation peaks due to the oxidation of transition metals at around 4.2 V as well as the oxygen redox at around 4.7 V. Both peaks are shifted to higher potentials with the reduction of cobalt and, moreover, the latter peak, associated with the oxygen redox, is less intense compared to the pristine material (see figure 2.13c), in agreement with the first cycle. As for the reduction peaks, we found only the peak related to the reduction of the metals whereas the oxygen release process disappeared.

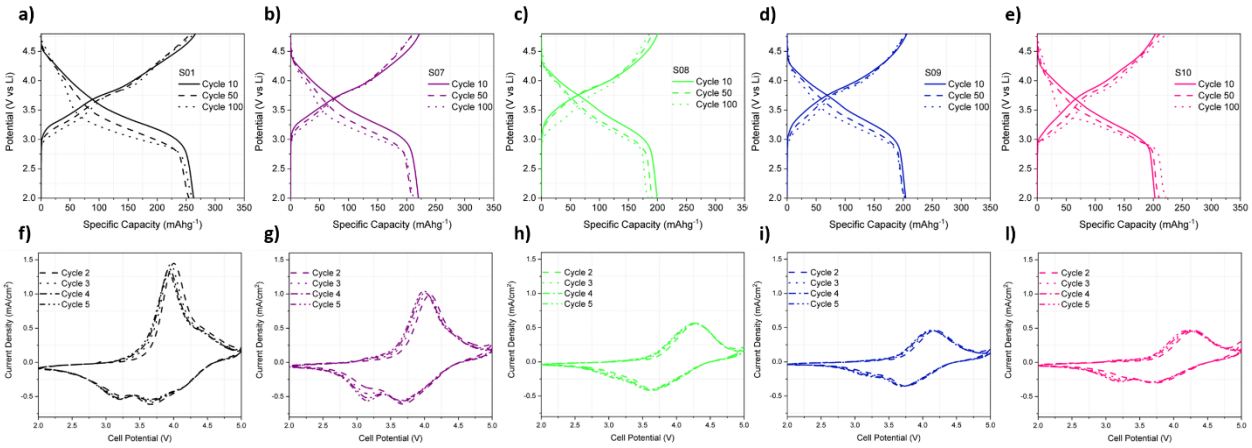

Figure 2.14: a-e) Potential Profile and e-l) cyclic voltammetries of S01, S07, S08, S09 and S10.

Looking at the charge/discharge profiles after 10, 50 and 100 cycles reported in figure 2.14a-d, we can observe a marked reduction in voltage decay in all the doped materials compared to the starting one (S01). As it is well known, the voltage decay is one of the main issues of Lithium Rich materials and seems to be correlated to a phase transition from layered to spinel structure during the cycling[11,39]. Figures 2.14e-h report the cyclic voltammetry after the first cycle where it possible to note how the shift of the peak, in the anodic scan, is mitigated compared to the sample S01 and the presence of a new peak around 3.1V during the anodic scan due to the activation of redox couple Mn^{4+}/Mn^{3+}. To confirm this trend, we have calculated the average discharge potentials for all samples and the results are shown in figure 2.15. The average discharge potential has been calculate by dividing the energy by the specific capacity. The energy can be calculate from the area of the discharge curve. The S01 average discharge voltage drops more quickly than the doped samples, in fact, the ΔV, the difference between the average voltage of the 1st cycle and 200th cycle, are 0.42, 0.34, 0.32, 0.33 and 0.27, respectively for S01, S07, S08, S09 and S10.

In summary, the replacement of cobalt with the contemporary over-lithiation and the co-doping with aluminum in LRLO materials, is a successful strategy to balance the cost reduction and satisfactory electrochemical performance in prolonged charge-discharge cycling tests.

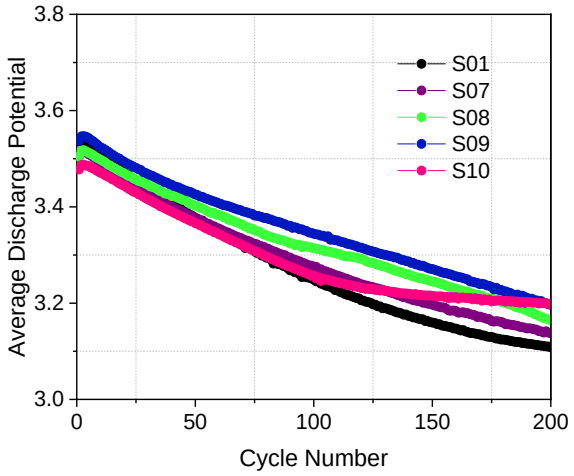

Figure 2.15: Average discharge voltage of Over-Lithiated series and S01 sample during galvanostatic cycling.

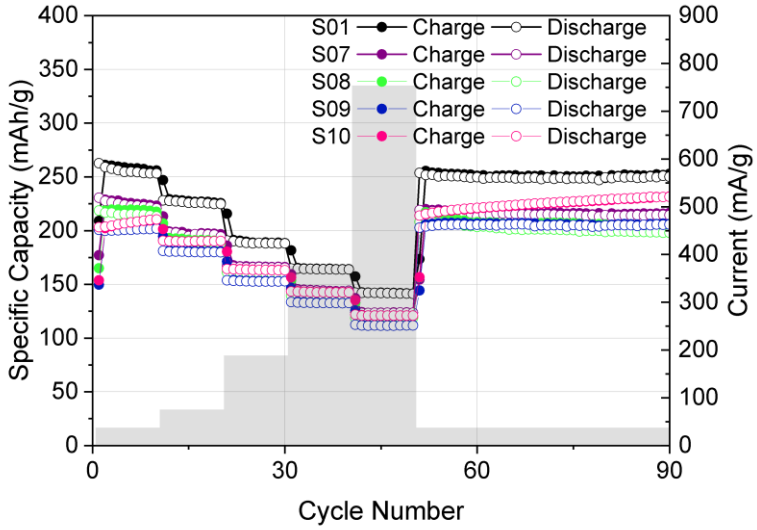

Figure 2.16: Rate Capability test of Over-Lithiated series.

Further electrochemical tests have been performed on these materials to verify their performance at high currents. Figure 2.16 shows the rate capability test at different C-rates, *i.e.* 0.1 C, 0.2 C, 0.5 C, 1 C, 2 C (1C=377 $mAhg^{-1}$). The specific capacities of the doped materials are smaller than that of the pristine material (S01), but it is worth noting that the difference in these capacities decreases when the current increases and, at the end of the experiment, the capacities are very close, in particular for S10. All samples are able to work at high currents, in fact, the discharge capacities

at 2C are 164, 144, 139, 133 and 143 $mAhg^{-1}$, respectively for S01, S07, S08, S09 and S10. Performance are very close and the slightly decrease can be explained by the reduction of the cobalt. However, the balanced metals blend allows to reach a good performance. For example, we have only a 13% drop in the capacity for S10 at 2C while the cobalt has been reduced by 85% compared to S01.

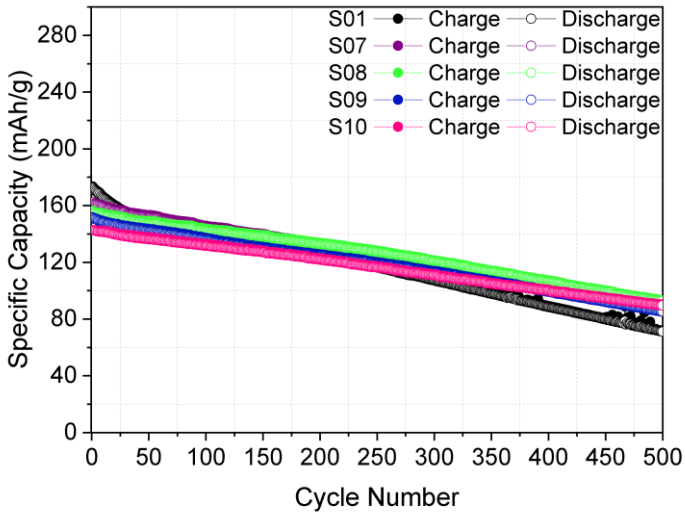

Figure 2.17: Galvanostatic cycling of S01, S07, S08, S09 and S10 at 1C (377 mAg^{-1}).

Finally, in figure 2.17 the comparison between over-Lithiated Al-doped samples and the pristine material at 1C for 500 cycles is shown in order to investigate the behavior during prolonged experiment. During the first discharge, the specific capacity follows the same trend of previous experiment and slightly decreases with the reduction of Cobalt. The capacity retention after 500 cycles is about 41, 54, 59, 56 and 63% for S01, S07, S08, S09 and S10, respectively, indicating the best cycling stability for the S10 sample.

Apparently, the simultaneous replacement of $Co^{2+/3+}$ mixed centres in the layered structure with balanced amounts of Al^{3+} and Li^{+} can enhance the performance at high current compared to pristine sample.

2.4 $Li_{1.28}Mn_{0.54}Ni_{0.13}Co_{0.02}Al_{0.03}O_2$ (S10) SAMPLE

2.4.1 Structural investigation of S10 sample

Being the Li and Al co-doping a good strategy to reduce cobalt in the structure of LRLO materials, while maintaining high electrochemical performance, we further investigated the sample S10, $Li_{1.28}Mn_{0.54}Ni_{0.13}Co_{0.02}Al_{0.03}O_2$.

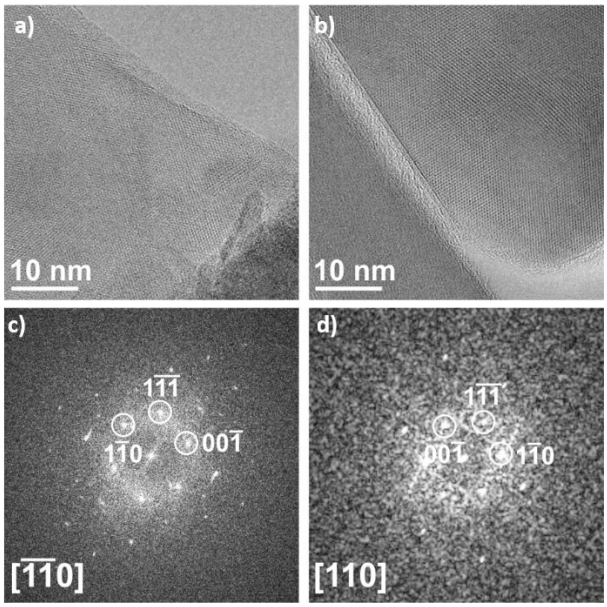

Figure 2.18: a-b) HR-TEM images and c-d) reconstructed FFT of S01 and S10.

A deeper structural analysis was performed by high resolution transmission electron (HR-TEM), XANES and XPS. In figure 2.18, the HRTEM micrographs are shown with reconstructed electron diffraction patterns by FFT using ImageJ. Synchrotron XRD patterns shown in figure 2.7 indicate the formation of a layered phase with the typical coexisting R-3m and C2/m structures. The HR-TEM analysis identify a monoclinic local crystal structures of the sample S10: in fact, the electron diffraction patters reconstructed by FFTs are indexed by the C/2m structure. Similar results were obtained for the S01 sample. Thus, cobalt substitution, aluminum doping and over-lithiation do not alter the complexity of the structural identity of this material, where disordered C2/m unit cells almost randomly packed along the c-axis distort the long-range symmetry to a R-3m lattice.

The atomic occupancy disorder (anti-site defects concentration) has been investigated by Rietveld refinement as well as the occurrence of oxygen vacancies (figure 2.19). The disorder has been refined to around 1%, while the oxygen occupancy below unity suggests vacancies in the anionic

sublattice (table 2.4). This last change matches the charge unbalance originated by the replacement of Co^{3+} with Li^{+} and Al^{3+} (pseudo n-doping), thus confirming the expected oxygen vacancies (*i.e.*, estimated S10 stoichiometry from XRD: $Li_{1.28}M_{0.72}O_{2-z}$, z=0.06, where M is the metal blend in the transition metal layer).

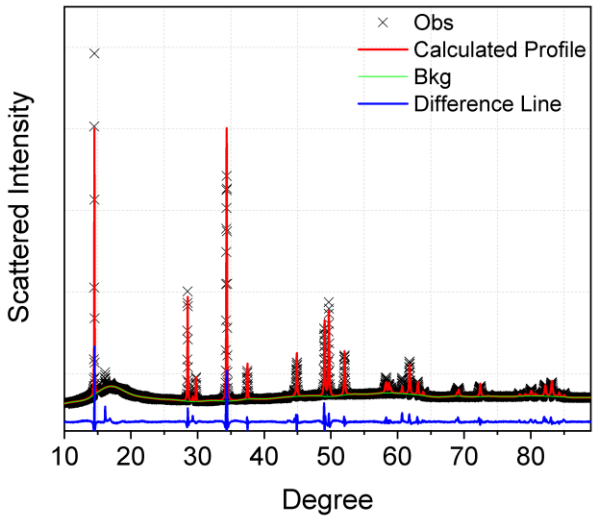

Figure 2.19: Rietveld refinement of S10 sample with anti-site defects and oxygen vacancies.

Table 2.4: Refined parameters of S10 sample with anti-site defects and oxygen vacancies.

Stoichiometry					**wR(%)**
$Li_{1.28}Mn_{0.54}Ni_{0.13}Co_{0.02}Al_{0.03}O_2$					**6.8**
Structural Model	*Cell Parameters*	*Atoms*	*Wyckoff Position*	*Atomic Coordinates*	*Occupancies*
R-3m	$a = 2.855$	Li/Ni	3b	0, 0, 0.5	0.99/0.01
	$b = 14.248$	Mn/Co/Ni/Li/Al	3a	0, 0, 0	0.54/0.02/0.12/0.29/0.03
		O	6c	0, 0, 0.739	0.97

The occurrence of oxygen vacancies induced by the pseudo n-doping impacts on the electronic structure of the S10 as outlined by X-ray absorption near edge spectroscopy (XANES) at the K and $L_{2,3}$-edges for Mn, Ni and Co, and X-ray photoemission spectroscopy in the Mn 2p region. The measurements were performed at XAFS and APE-HE beamlines of the ELETTRA synchrotron radiation for XANES and XPS analysis, respectively, in collaboration with Istituto

Officina dei Materiali (IOM)-CNR. The samples S01 is reported as a comparison. The XANES spectra at the Ni and Mn K-edges are shown for the S10 and S01 samples in the figure 2.20.

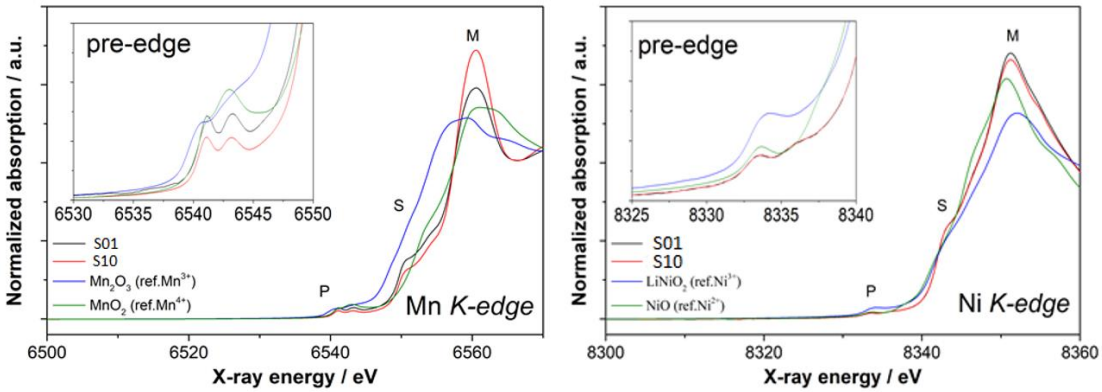

Figure 2.20: Experimental XANES spectra at the K-edges of a)Mn and b)Ni measured for the S10 and S01 samples. Experimental reference spectra for Mn_2O_3, MnO_2, NiO and $LiNiO_2$ are also shown.

The two samples show mainly the same electronic structure at both Mn and Ni edges. Pre-edge peak P (1s → 3d inner atomic transition, dipole forbidden- quadrupole allowed) at Mn edge suggests the occurrence of a reduced inversion symmetry of Jahn-Teller distorted MnO_6 octahedra in the structure, being the observed doublet due to the crystal-field splitting of Mn 3d states into t_{2g} and e_g orbitals. The other spectral features (e.g. S peak associated with 1s transitions into p-like states of t_{1u} symmetry, and the white-line M)[40] are remarkably similar in the two samples. Quantitative fittings of the pre-edge and edge regions allow to estimate the mean Ni and Mn oxidations states in the two samples (*i.e.*, Ni +2.12±0.02 and +2.23±0.02, Mn+3.89±0.02 and +3.86±0.02, for S01 and S10, respectively). These values confirm the occurrence of a minor Jahn-Teller electronic distortion originated by the simultaneous charge transfer from the Ni^{2+} centers to Mn^{4+}, thus leading to the formation of small amounts of Ni^{3+} and Mn^{3+}.

A careful analysis of the oxides stoichiometry, assuming the electro-neutrality constraints and the Co^{3+} Al^{3+} Li^{+} oxidation states, indirectly confirms the possible occurrence of vacancies on the oxygen anion sublattices in the Co-poor sample (*i.e.*, $z \approx 0$ and 0.1, $Li_{1+x}M_{1-y}O_{2-z}$, for S01 and S10, respectively) in line with the XRD Rietveld results.

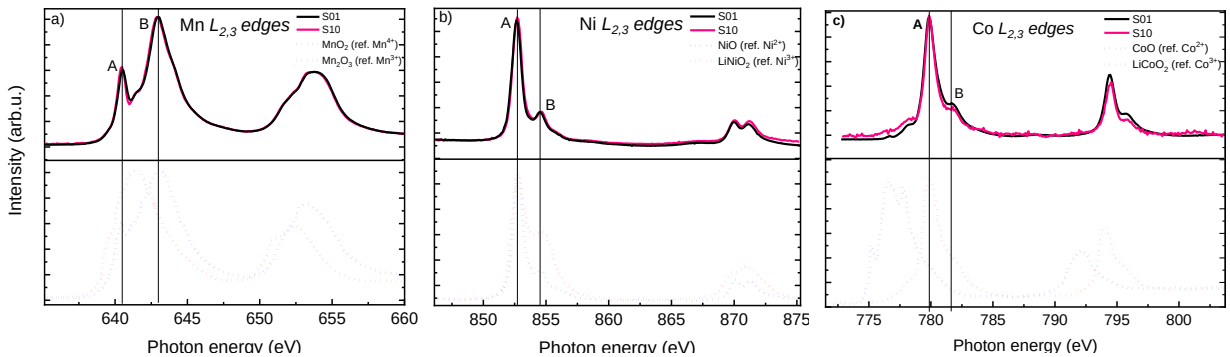

Figure 2.21: Upper panels: experimental $L_{2,3}$ edges XANES of a) Mn, b) Ni, c) Co measured for the S01 (blue line) and S10 (red line) samples. Lower panels: experimental reference spectra for a) Mn_2O_3 and MnO_2, b) NiO and $LiNiO_2$, c) LiCoO2 and CoO.

The XANES spectra at the Co, Ni and Mn $L_{2,3}$-edges are shown in the figure 2.21. The electronic transitions giving rise to the most intense structures of these spectra are related to dipole allowed $2p \rightarrow 3d$ transitions. The spin–orbit interaction of the 2p core holes splits the spectra into two multiplets, the L_3 ($2p_{3/2}$) edges at ≈ 643, 853 and 780 eV for respectively Mn, Ni and Co, while the L_2 ($2p_{1/2}$) edges fall at ≈ 653, 871 and 795 eV. In turn, all the three L_3 are split in two structures (labeled as A and B). Since the $L_{2,3}$ edges probe the unoccupied 3d states of the absorbing atoms, the resulting spectral shapes change accordingly to the different filling of the 3d orbitals in the ground state (and thus to different oxidation numbers) but also to the different crystal field effects[41]. The comparison with the reference spectra (lower panels) allows to assign the oxidation numbers of 4+, 2+ and 3+ respectively to Mn, Ni and Co for both samples[42,43]. Focusing on the Mn $L_{2,3}$ edges spectra, peaks A and B are related to $p \rightarrow d$ dipole allowed transitions towards the unoccupied 3d molecular orbitals originating from the crystal-field splitting of Mn 3d states in a distorted octahedral geometry[42]. Comparing the experimental spectra with the reference spectrum of the MnO_2 (blue dotted spectrum), it can be observed that A and B structures in the experimental spectra are sharper. This can be related to transitions towards more energetically localized 3d orbitals, confirming thus that in both S10 and S01 samples the orbital splitting caused by the Jahn Teller effect is less pronounced with respect to the conventional distorted octahedral coordination of Mn in MnO_6. It is important to underline that this last consideration is only qualitative, indeed the energy separation between peaks A and B, albeit depending on the crystal field effects, cannot be related directly to the difference between the t_{2g} and e_g states, because the 3d-3d as well as the 2p-3d two-particle interactions strongly contribute to the spectral shape[41]. For what concern Ni^{2+}

and Co^{3+}, also theoretical calculations confirm that structures A and B in the $L_{2,3}$ edges spectra are related to an O_h symmetry of the absorbing atoms. Data of *L edges* show that the surface composition of the samples is similar to bulk one observed in the XAS *K edges* spectra of figure 2.20: indeed, the soft X-Rays spectroscopy (operated in total electron yield) is much more surface sensitive than the hard X-Rays one (related to the photon energies of the transition metals K edges).

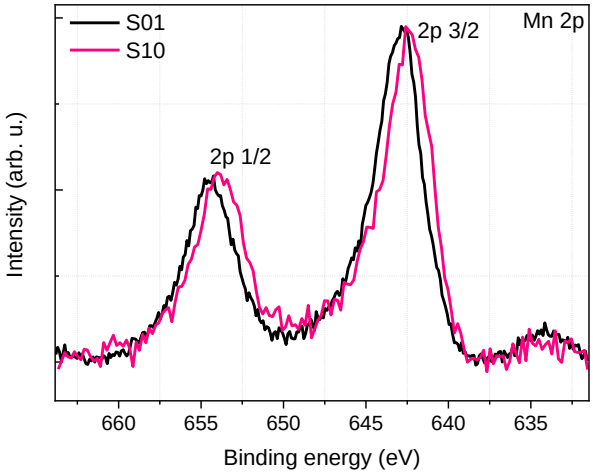

Figure 2.22: Experimental XPS Mn 2p core level spectra of S01 and S10 samples. $2p_{3/2} \approx 642.5$ eV; $2p_{½} \approx 654$ eV.

The XPS spectra of the Mn 2p region has been also acquired and analyzed for both S10 and S01 to match the results of the XANES investigation. The Mn 2p core levels (see figure 2.22) confirms the +4 oxidation state of Mn (looking at the spectral shape and energetic positions[44]). The two peaks slightly shift (≈0.2 eV) to lower binding energies in S10 possibly attributed to a minor oxidation of the Mn centers in agreement with the quantitative fitting of the K edge XANES spectra of Mn reported above.

Starting from the ICP compositions and the XAS experimental charges on Ni and Mn in both S10 and S01 it is possible to estimate oxygen vacancies, assuming the electro-neutrality constraints and the Co^{3+} Al^{3+} Li^{+} oxidation states. Our estimates confirm the presence of vacancies on the oxygen anion sub-lattices only in the Over-Lithiated sample (*i.e.* z=0.1 assuming the general stoichiometry $Li_{1.28}TM_{0.72}O_{2-z}$). This defect concentration is in quantitative agreement with the XRD Rietveld results.

Once established the impact of the alteration of the metal blend induced by over-lithiation, *i.e.* formation of extended oxygen vacancies and increase of Jahn-Teller distortions by minor oxidation of the $Ni^{2+}$to Ni^{3+} it is possible to reconsider the apparent negligible structural changes of the lattice passing from S01 to S10. By assuming the Shannon atomic radii[35] for O^{2-} (1.40 Å), Mn^{3+} (0.58 Å), Mn^{4+} (0.53 Å), Ni^{2+} (0.69 Å), Ni^{3+} (0.56 Å), Co^{3+} (0.55 Å), Li^{+} (0.76 Å) and Al^{3+} (0.54 Å) and considering the volume of the unit cell derived by Rietveld refinement, it is possible to estimate the corresponding fraction filled by atoms in the transition metal layer (2.8 and 3.0% for the S01 and S10 materials, respectively) as well as lithium ions in the Li layer (5.5% for both materials), oxygen anions in the O-layers (68.7 and 66.5% for the S01 and S10 materials, respectively) or unoccupied (structural voids, 23.1 and 25.0% for the S01 and S10 materials, respectively). Overall, the minor structural change (+0.1% in the cell volume passing from S01 to S10) balances opposite structural alterations: (i) the larger steric hinderance of the transition metal layer and the formation of oxygen vacancies that (ii) shrinks the volume occupied by the anion sublattice and (iii) enlarge the empty voids in the lattice.

2.4.2 Post-mortem analysis of cycled S10 electrodes

Regarding the electrochemical behavior, galvanostatic cycling, cyclic voltammetries and rate capability tests are extensively analyzed in the section 2.3.3, in particular in figures 2.13, 2.14, 2.15, 2.16 and 2.17. The S10 keeps an almost constant specific capacity value of about 220 $mAhg^{-1}$ from cycle 50 to cycle 200 while the S01 fades from 270 $mAhg^{-1}$ to 250 $mAhg^{-1}$. However, S10 outperforms S1 in respect to: (a) capacity retention; (b) mean discharge potential (see figure 2.17); (c) potential hysteresis between charge and discharge (it is 0.7 V at cycle 200 to be compared to 0.93 V for S01);, and (d) the cumulative irreversible capacity suffered upon cycling that is reduced by -38% at cycle 200 compared to S01, as reported in figure 2.23.

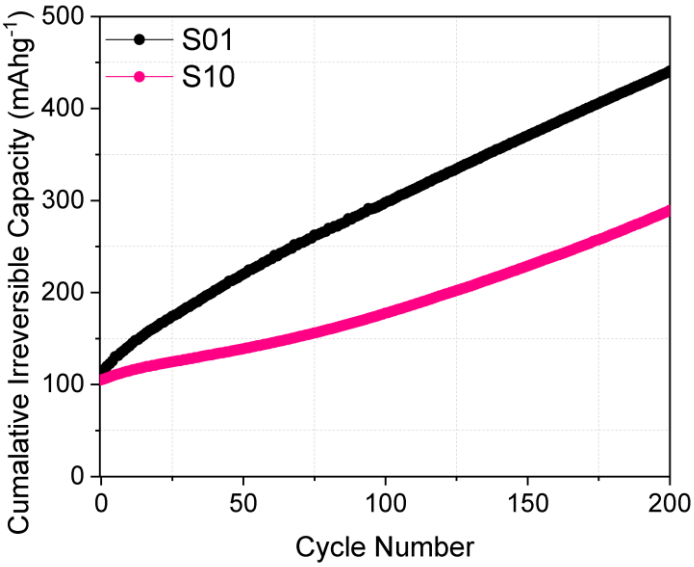

Figure 2.23: Cumulative irreversible capacity vs cycle number.

Overall, S10, despite the slight reduction in the specific capacity compared to the S01, shows superior capacity retention, smaller irreversible capacity, and improved energetic efficiency (*i.e.*, 82% vs. 76% at cycle 200 for S10 and S01, respectively). Among all beneficial effect in the cell performance provided by the substitution of Co with an optimized blend of Li/Al, the most relevant one is the strong mitigation of the voltage decay upon cycling. LRLOs suffer a remarkable voltage decay upon cycling likely due to the irreversible release of molecular oxygen, the accumulation of oxygen vacancies and the resulting structural transformation from a layered to a spinel-like structure[45–47] .The oxygen loss suffered during the first charge plateau at 4.5 V plays a crucial role in voltage fade[48] as it impacts the redox active couple at high voltage O^{2-}/O^{-} and the lattice stability[29]. Therefore, the remarkable limitation of the voltage plateau in the S10 compared to the S01 is an electrochemical fingerprint of an improved balance between native vacancies and lattice stability likely leading to the reduction of the voltage decay.

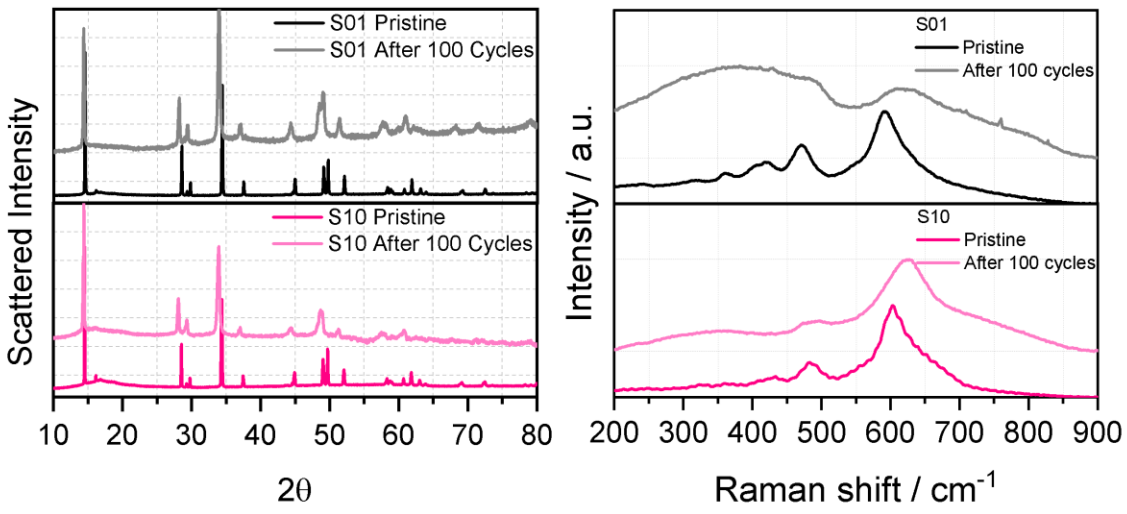

Figure 2.24. Synchrotron Diffraction patterns and Raman spectra of S01 and S10 after 100 cycles in comparison with pristine one.

To prove this point, the structural stability was evaluated by post-mortem XRD and Raman spectroscopy of S10 after 100 galvanostatic cycles at C/10 as shown in figure 2.24. The diffractogram, in comparison with the pristine one, highlights only a slight loss of crystallinity and cell volume expansion of the original R-3m lattice without any trace of extra peaks due to the spinel formation. Regarding the Raman analysis, the spectra of pristine LRLOs consist of two active modes connected to the R-3m lattice (600 and 485cm^{-1}) and six modes to the C2/m structure (605, 552, 432, 411, 364, 328 cm^{-1})[49,50]. From the Post mortem Raman spectra (figure 2.24b), the most intense peaks around 600 and 485 cm^{-1} are still visible and intense for S10 samples. On the other hand, in S01 sample, it is possible to identify only a broader peak around 620 cm^{-1}. It is possible that we have a spinel structure component in the spectra due to the broaden peak but, surely, it is not the most important component at least for S10 sample. Furthermore, for both materials, the peaks associated with the C2/m structure disappear. The spectrum of S10 confirms that the layered structure is still maintained. The results are in agreement with the post mortem XRD, the superstructure peaks are not even visible in the patterns and the layered structure is more defined in S10.

2.4.3 Evaluation of S10 performance in Li-ion cell

Once established the performance of the over-lithiated LRLO, we investigated its use as positive electrode in a full Li-ion formulation vs. graphite to prove the performance of a full battery prototype.

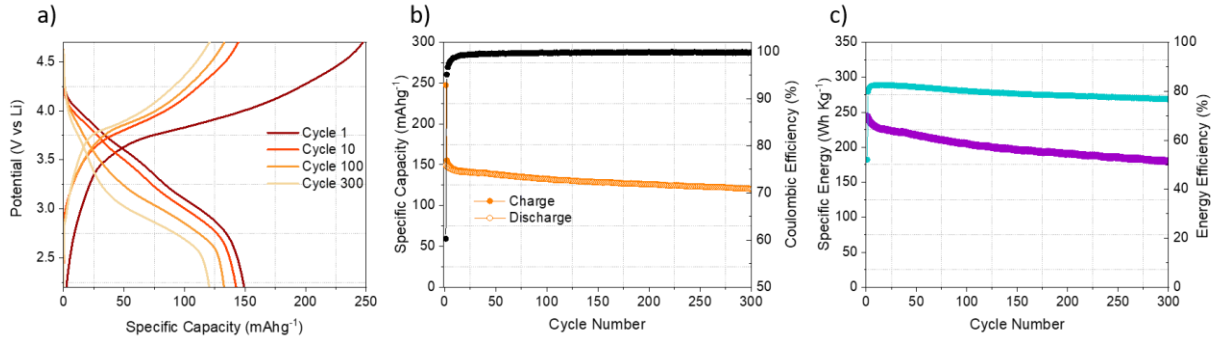

Figure 2.25: Cells have been assembled accordingly to the following galvanic chain: (-) Graphite / EC:DMC 1:1 Vol $LiPF_6$ 1mol/L / LRLO (+) and tested in galvanostatic regimes at 1C (230 mAg^{-1}) in the 4.7-2.2 V vs Li range. (a) Voltage profile; (b) Specific capacity vs cycle, (c) Corresponding specific energy vs cycle.

Battery performance are shown in figure 2.25 whereas the electrochemical characterization of graphite lithium half cells is reported in figure 2.26. The full lithium-ion battery shows promising and stable performance upon cycling, reaching a specific discharge capacity of 150 $mAhg^{-1}$, based on the mass of positive material, with a capacity retention of 80.4% after 300 cycles (figure 2.25b). The voltage profile shows a featureless slope in charge and discharge with irreversibly capacities losses limited to the first cycle being the coulombic efficiency >99.5% from cycle 2 to 300. A remarkable constant specific energy is obtained reaching about 200 $WhKg^{-1}$, calculated in respect to the sum of both electrode masses, with a stable energy efficiency approaching 80%.

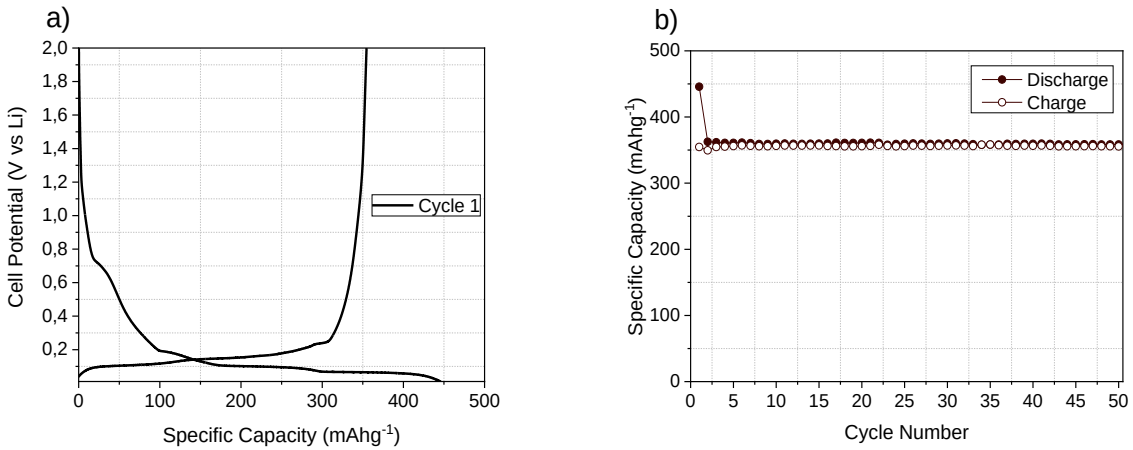

Figure 2.26: First cycle (a) and specific capacity vs cycle number (b) of graphite in half-cell. The current is 37.2 mAg^{-1} in a voltage range between 0.01-2V.

2.5 EXPLORING THE OVER-LITHIATION AND MN-DOPING

In consideration of the excellent electrochemical properties of Over-Lithiated Al-Doped samples, we further investigated the Co removal by simultaneously over-lithiation and manganese doping. In fact, the Al is electrochemically inactive, while the Manganese is active in cells. Therefore, starting from S01, two new samples were synthetized and the stoichiometries are reported in the table 2.5.

Table 2.5: Stoichiometries of S11 and S12 samples.

	Formula	%Li	%Mn	%Co	%Ni
S11	$Li_{1.25}Mn_{0.563}Ni_{0.125}Co_{0.06}O_2$	**62.5**	**28.2**	**3**	**6.25**
S12	$Li_{1.25}Mn_{0.625}Ni_{0.125}O_2$	**62.5**	**31.2**	**0**	**6.25**

Figure 2.27 shows the XRD patterns of the two samples and, as can be noted, we find again the typical peaks associated with these materials. The reference patterns in the figure allow to index most of the peaks to $LiTMO_2$ and the peaks between 20° and 25° to the Li_2MnO_3 phase. There is no presence of other phases, confirming that the over-lithiation and Mn-doping do not change the structure.

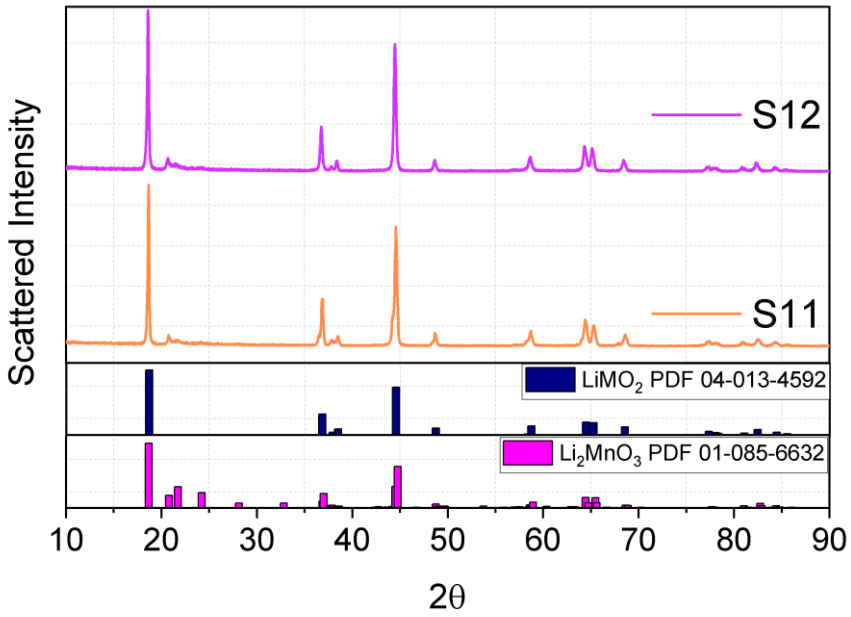

Figure 2.27: XRD patterns of S11 and S12.

The S11 sample is made up of polyhedral shaped particles with a homogeneous size between 150-200 nm (figure 2.28). Unlike the previous sample, S12 consists of agglomerates of particles, as can be seen from the 2.28d image at high magnification. The particle shape turns out to be much more irregular compared to that of S11.

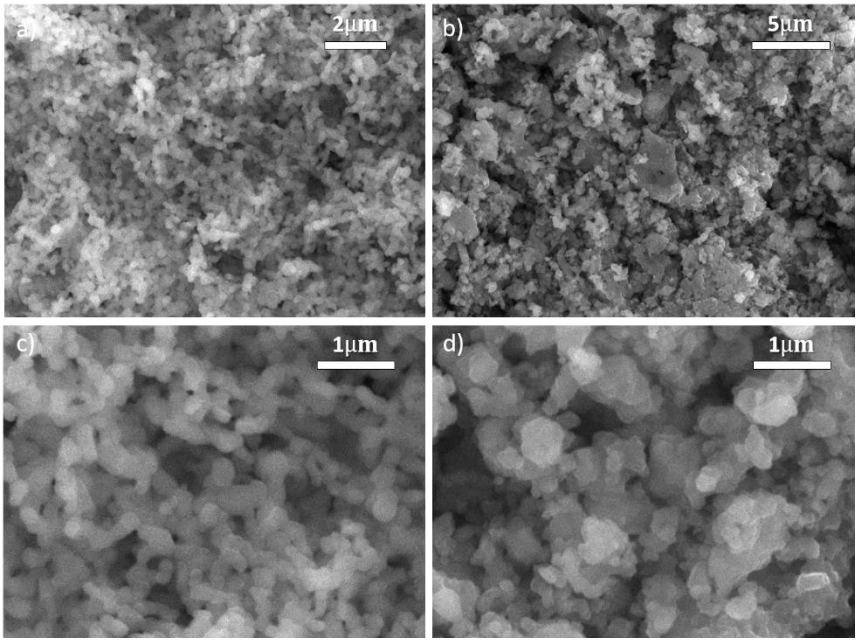

Figure 2.28: Micrographs obtained by Scanning Electron Microscopy of a-c) S11 e b-d) S12.

The samples were tested in lithium cells by galvanostatic cycling using a potential window of 2-4.8V.

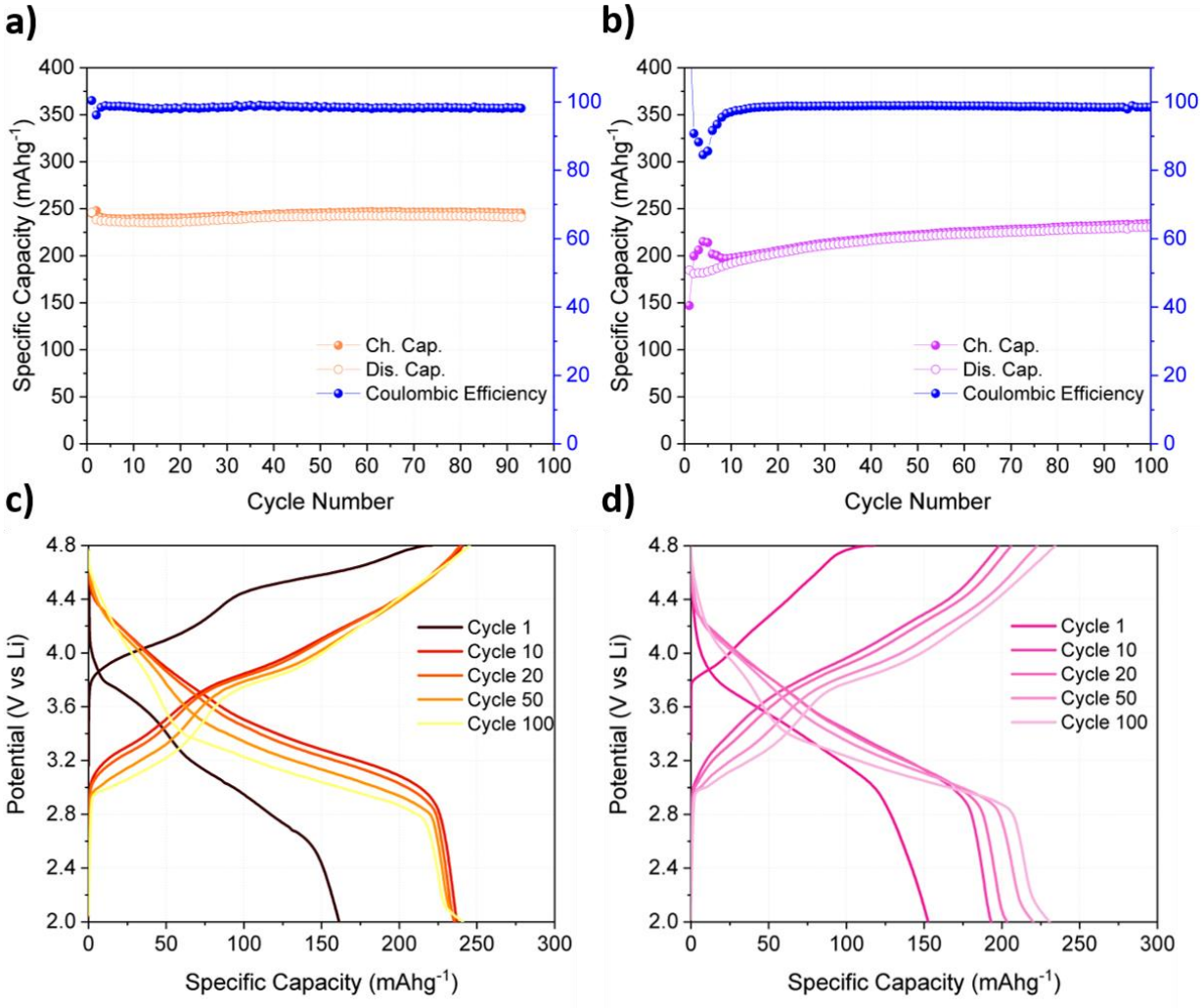

Figure 2.29: Specific capacity and potential profiles of S11 and S12.

Figure 2.29 shows the specific charge/discharge capacities as a function of the number of cycles and the potential profiles of the samples. During galvanostatic cycling, the electrochemical performance of the S11 sample shows high stability, in fact it is able to exchange a capacity of 245 $mAhg^{-1}$ during the first cycle and 239 $mAhg^{-1}$ after 100 cycles. When the cobalt is completely removed from the structure by increasing the manganese content, the electrochemical behavior change. In fact, S12 shows a trend activated during cycling, starting from a specific capacity of about 185 $mAhg^{-1}$ in the first cycle reaching a capacity of 231 $mAhg^{-1}$ after 100 cycles. At the end of the experiment, the two samples have comparable performance. The preliminary

electrochemical characterization shows a very promising performance for sample S12, considering the low content of Nickel and the removal of cobalt from the metals blend. Therefore, a careful investigation was carried out to analyze the properties of this material. The electronic structure of S12 has been investigated by X-ray absorption near edge spectroscopy (XANES) at Ni and Mn K-edges and X-ray photoemission spectroscopy (XPS), to probe the oxidation state of elements in the bulk and on the particles surface, respectively. XANES spectra recorded in the S12 material are shown in figure 2.30. Mn_2O_3, MnO_2 and NiO and $LiNiO_2$ have been used as references and recorded in the same experimental conditions.

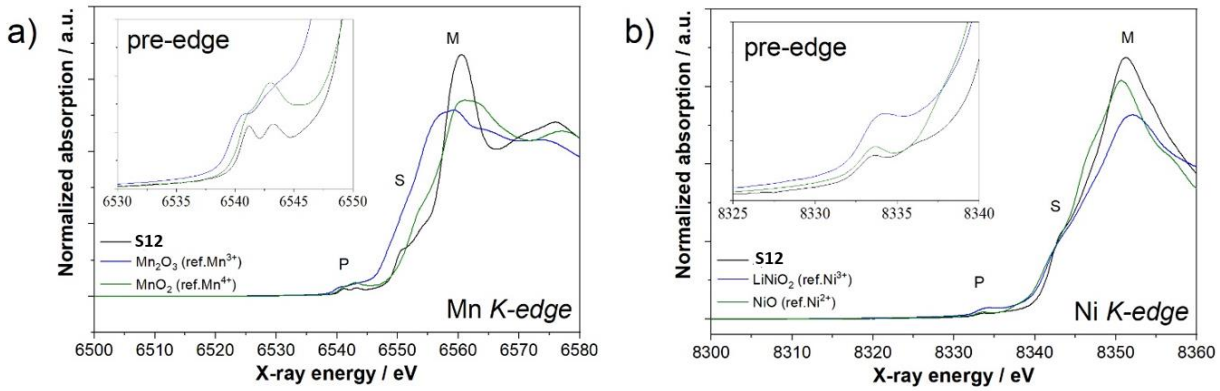

Figure 2.30: XANES spectra at K-edges of a) Mn and b) Ni obtained for S12 sample.

The S12 sample shows mainly the same electronic structure at both Mn and Ni edges. Pre-edge peak P (1s → 3d inner atomic transition, dipole forbidden- quadrupole allowed) at the Mn edge suggests the occurrence of a reduced inversion symmetry of Jahn-Teller distorted MnO_6 octahedra in the structure, being the observed doublet due to the crystal-field splitting of Mn 3d states into t_{2g} and e_g orbitals. The other spectral features are expected (*i.e.* S peak associated with 1s transitions into p-like states of t_{1u} symmetry, and the white-line M) and in line with the literature[40]. Quantitative fittings of the pre-edge and edge regions allow to estimate the mean Ni and Mn oxidations states: Ni +2.09±0.02 and Mn +3.91±0.02. These values confirm the occurrence of a minor Jahn-Teller electronic disorder distortion originated by the simultaneous charge transfer from the Ni^{2+} centers to Mn^{4+}, leading to limited concentrations of Ni^{3+} and Mn^{3+}. The Figure 2.31 shows the XPS core-level spectrum of Ni $2p_{3/2}$, Mn 3s and O1s.

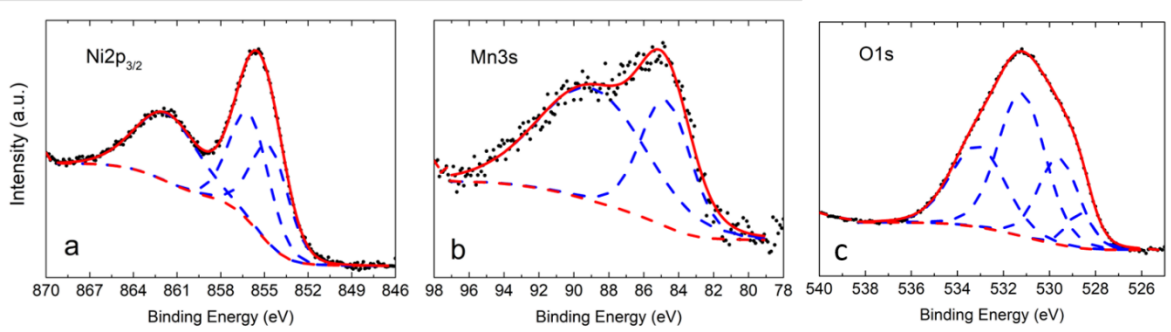

Figure 2.31: XPS a) Ni2$p_{3/2}$, b) Mn3s and c) O1s core-level spectra of S12 sample.

Binding energies are referred to the C1s C-C(C-H) peak set at 284.7eV (internal calibration). The Ni spectral features display a major asymmetric peak at 855.6eV with a satellite structure at 862eV[51,52]. The binding energies and the shape of the Ni 2$p_{3/2}$ signal are characteristic for Ni^{4+}, NiOOH or $Ni(OH)_2$[53], and accordingly the peak can be fitted at least with two components at 856eV and 854.6eV (blue-dashed curves) which can be ascribed to Ni(IV) and Ni(II), respectively[54]. Due to the broad shape of the peak and the absence of visible structures, the presence of Ni(III) cannot be excluded. Indeed, XPS measurements show slight differences with XANES, revealing higher Ni oxidation state in the particles surface compared to the bulk.

The Mn2$p_{3/2}$ core-level maximum is observed at 643.0eV, in the energy range characteristic of Mn^{4+}.[55] Figure 2.31b shows the Mn3s XPS data superimposed to the best fit. Galakhov et al.[56] demonstrated that the splitting between the main Mn3s peak and its satellite, due to exchange coupling between the 3s hole and 3d electrons, is highly sensitive to the average Mn oxidation state (AOS). The larger the splitting the lower is the oxidation state, approximately according to the equation, AOS = 8.956-1.126 ΔE, where ΔE is the splitting energy[57]. Our splitting results 4.25eV therefore indicating an oxidation state of 4.

The oxygen O1s shows a broad, intense, and multicomponent intensity in the region around 531eV (figure 2.31c). The fitting of the O1s line-shape reveals the presence of three components at 529.0eV, 531eV and 533.2eV. The O1s in layered oxides is typically reported at 529.5eV[54]. The observed lower binding energy value could be due to the compresence of an unresolved component at 528.6 attributable to Li_2O[58,59] suggesting the presence of lithium rich regions, not surprising in an over-lithiated compound. Peroxide species, occurring at higher BE, are excluded**.**

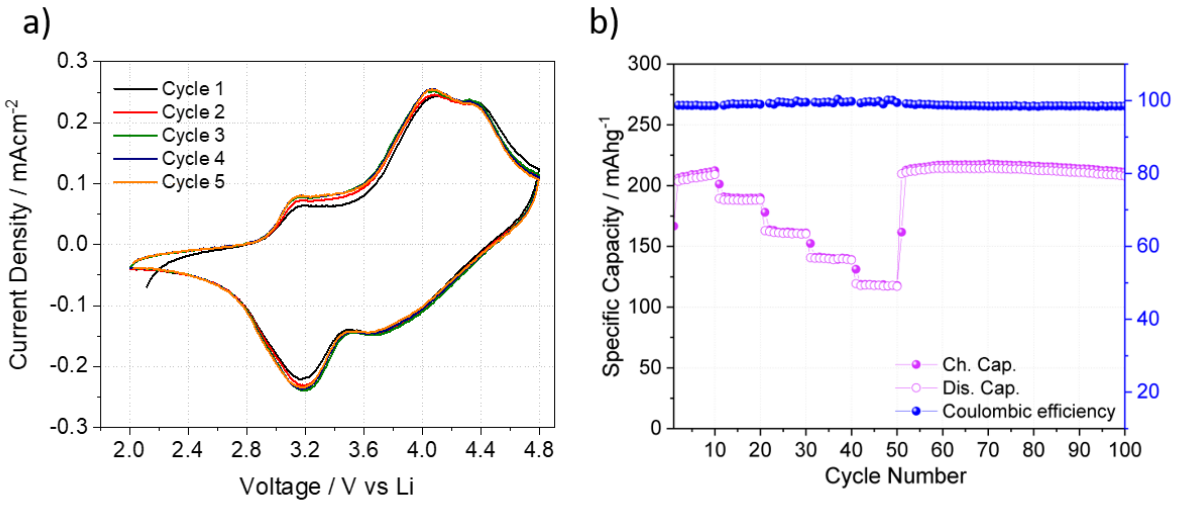

Figure 2.32: a) Cyclic Voltammetry and b) rate capability test of S12.

Further electrochemical tests were performed to complete the characterization, in particular a cyclic voltammetry, to shed light the electrochemical process, and a rate capabilities test, to check material behaviour at high current. The results are shown in figure 2.32. CV recorded after activation (figure 2.32a) clearly shows the simultaneous redox activity of Ni and Mn. In the anodic scan, the voltammogram exhibits a composite peak around 4.2V vs Li, likely due to the oxidation of Ni^{2+}/Ni^{3+}, Ni^{3+}/Ni^{4+} and O^{2-}/O^{-}. Moreover, an electroactive process around 3.2V can be observed, possibly associated to the redox couple Mn^{4+}/Mn^{3+}. Upon cycling, we can observe a very light increase of all the redox processes, in accordance with the activated trend obtained during galvanostatic cycling. A rate capability test has been also performed from C/10 to 2C as shown in figure 2.32b. S12 electrode displays high capacity and excellent rate performance. It delivers discharge capacities of 205, 188, 160, 140 and 118 $mAhg^{-1}$ at C/10, C/5, C/2, 1C, 2C, respectively. Moreover, when the current goes back to C/10, S12 can recover all the initial discharge capacity.

Post-mortem analysis after cycling of S12 has been carried out, including Synchrotron XRD pattern, Raman spectrum and SEM images. Figure 2.33 shows the XRD and Raman results, in comparison with the pristine ones. Regarding the XRD, all the peaks shift to smaller 2θ angles due to structural rearrangements occurring upon cycling. Peaks are smaller in intensity and larger in shape compared to the pristine material pattern: this is a clue of a reduction of the crystallite sizes induced by the repeated extraction/insertion of lithium ions from/into the host material. The 2θ

region between 10°-20° shows that peaks indexed to the monoclinic Li_2MnO_3 distortion almost disappear after cycling. This indicates the loss of the limited Li-Mn cation ordering in the transition metal layers[60] upon cycling.

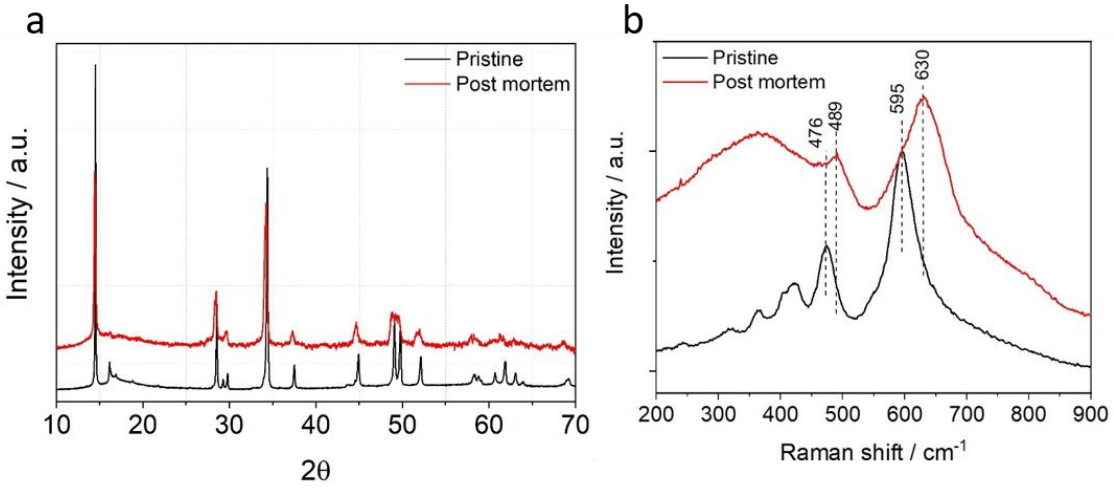

Figure 2.33: Post-mortem analysis of S12. a) Synchrotron X-ray Diffraction and b) Raman Spectroscopy.

Raman spectra were recorded on the cycled electrode, to highlight vibrational fingerprint of local distortion on the crystallite surface: results are shown in figure 2.33b. The Raman spectra before cycling presents the typical vibrational modes of LRLOs. The E_g band around 476 cm^{-1} in the pristine electrode is shifted to 489 cm^{-1}, while the A_{1g} band appears as a shoulder of the intense peak at around 630 cm^{-1}. This last intense feature can originate from vibrations also of a spinel-like structure. The coexistence of the A_{1g} and E_g bands and the strong band at around 630 cm^{-1} is a clue of the presence of two different local M-O arrangements in the electrodes after cycling.

Overall, even though some structural rearrangements occur, the material maintains the layered structure upon cycling being limited the crystallographic alterations. In particular XRD highlights a loss of monoclinic distortion[39] and the persistence of the trigonal lattice whereas Raman spectroscopy suggests the possible formation of local motifs of the spinel structure on the crystallite surface. This structural resilience matches the excellent electrochemical activity and the remarkable capacity retention whereas the limited voltage decay suffered upon cycling can be related to the abovementioned partial structural rearrangements. Finally, postmortem electrode has been analyzed by FE-SEM and the acquired images reported in figure 2.34, in comparison to the pristine electrode. As evident from figure, even after almost 200 cycles, the electrode maintains its

initial morphology and remain undamaged. The polyhedral particles retain their shape, while their dimensions seem increased.

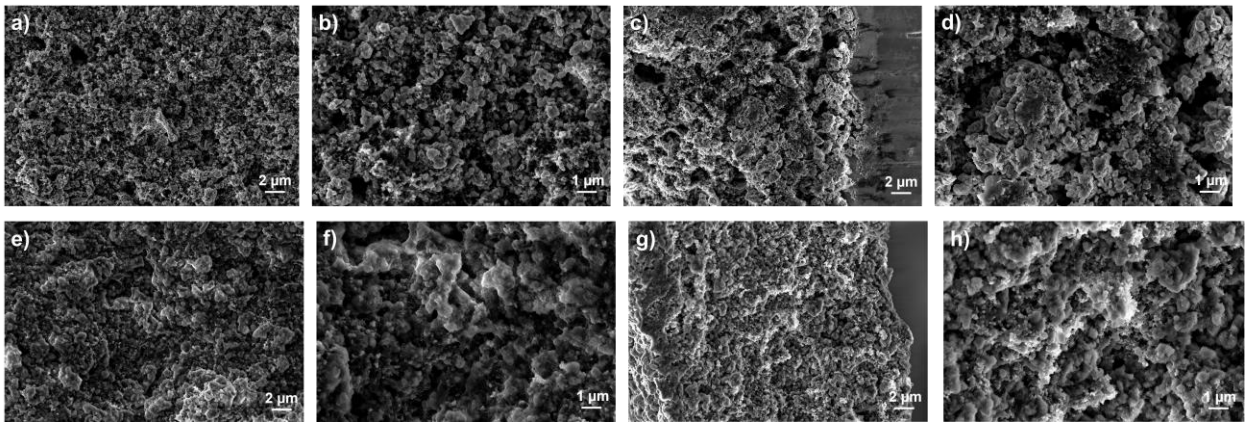

Figure 2.34: FE-SEM images of S12 electrode a-d) before and e-h) after cycling.

2.6 CONCLUSIONS

In this chapter, the synthesis and physical-chemical characterization of doped Lithium-Rich layered oxides have been discussed. The final goal was to reduce or eliminate cobalt from the structure, without damaging the electrochemical performance. A Sol-Gel process has been used to synthetize all the samples, maintaining the same synthetic condition. The introduction of Al as a dopant into the structure of $Li_{1.2}Mn_{0.54}Ni_{0.13}Co_{0.13}O_2$, with different amounts, was analyzed in terms of structure, morphology and electrochemical performance. From a chemical-physical point of view, the Al-doped samples have the same features, *i.e.* layered structure and polyhedrical particles in a range of 200-400 nm. Instead, the electrochemical behavior changes completely while the Al content grows in the material: in particular the specific capacity drops in parallel with the Al increase. On the contrary, over-lithiation has proven to be a good strategy. Therefore, a new set of over-lithiated materials has been prepared and for all we obtained specific capacities beyond 200 $mAhg^{-1}$ for 200 cycles. The layered structure was kept for all samples and a complete electrochemical characterization was performed. The rate capability tests and cyclic voltammetries show very stable electrode materials at high current and a modification of the main redox process, respectively. The sample S10 ($Li_{1.28}Mn_{0.54}Ni_{0.13}Co_{0.02}Al_{0.03}O_2$) has been characterized deeper to understand better the features of the over-lithiated samples. Rietveld refinement, XAS and XPS allowed to catch sight of the formation of extended oxygen vacancies and the increase of Jahn-

Teller distortions. These changes in the composition lead to remarkably improved performance in lithium half cells, in particular the reduction of the irreversible capacity accumulation, improvement of the capacity retention, increase of the mean discharge potential and limitation of the potential hysteresis between charge and discharge. A remarkable improvement in the voltage decay was observed, originated by the excellent structural stability of S10 upon cycling, as demonstrated with XRD and Raman post mortem. To investigate the practical use of the electrode in full battery, we selected graphite as a negative counterpart and tested the Lithium-Ion performance. The resulting high specific capacity and high energy density suggests our over-lithiated formulation very promising. As a final point, the over-lithiation and Mn-doping have been used to obtain a cobalt-free electrode material, showed in section 2.5. S12 sample ($Li_{1.25}Mn_{0.625}Ni_{0.125}O_2$) can supply excellent electrochemical performance either at low and high currents and long cycling life stability. The reasons can be found in a good balancing of Ni/Mn/Li blend in the transition metal sublattice, which stabilizes the lithium extraction/insertion and the oxygen vacancy formation during the first cycles disclosing excellent performance in prolonged cycling.

REFERENCES

1. Whittingham, M. S. Lithium batteries and cathode materials. *Chem. Rev.* **104**, 4271–4301 (2004).
2. Choi, N. S. *et al.* Challenges facing lithium batteries and electrical double-layer capacitors. *Angewandte Chemie - International Edition* **51**, 9994–10024 (2012).
3. Peres, J. P. *et al. The Relationship between the composition of Lithium Nickel Oxide and the loss of reversibility during the first cycle.* (1996).
4. Chen, C. H. *et al.* Aluminum-doped lithium nickel cobalt oxide electrodes for high-power lithium-ion batteries. *J. Power Sources* **128**, 278–285 (2004).
5. Ohzuku Tsutomu & Makimura Yoshinari. Layered Lithium Insertion Material of $LiNi_{1/2}Mn_{1/2}O_2$: A Possible Alternative to $LiCoO_2$ for Advanced Lithium-Ion Batteries. *Chemistry letters*, **30** (2001).
6. Ji, X. *et al.* A review on progress of lithium-rich manganese-based cathodes for lithium ion batteries. *Journal of Power Sources* **487**, (2021).
7. Nayak, P. K. *et al.* Review on Challenges and Recent Advances in the Electrochemical Performance of High Capacity Li- and Mn-Rich Cathode Materials for Li-Ion Batteries. *Advanced Energy Materials* **8**, (2018).
8. Thackeray, M. M. *et al.* Li_2MnO_3-stabilized $LiMO_2$ (M = Mn, Ni, Co) electrodes for lithium-ion batteries. *J. Mater. Chem.* **17**, 3112–3125 (2007).
9. Lu, Z., Chen, Z. & Dahn, J. R. Lack of cation clustering in $Li[Ni_xLi_{1/3-2x/3}Mn_{2/3-x/3}]O_2$ ($0 < x \leq 1/2$) and $Li[Cr_xLi_{(1-x)/3}Mn_{(2-2x)/3}]O_2$ ($0 < x < 1$). *Chem. Mater.* **15**, 3214–3220 (2003).
10. Wang, J. *et al.* Lithium- and Manganese-Rich Oxide Cathode Materials for High-Energy Lithium Ion Batteries. *Adv. Energy Mater.* **6**, (2016).
11. Zhao, S., Yan, K., Zhang, J., Sun, B. & Wang, G. Reaction Mechanisms of Layered Lithium-Rich Cathode Materials for High-Energy Lithium-Ion Batteries. *Angewandte Chemie - International Edition* **60**, 2208–2220 (2021).
12. Zheng, J. *et al.* Li- and Mn-Rich Cathode Materials: Challenges to Commercialization. *Advanced Energy Materials* **7**, (2017).
13. Yan, W. *et al.* Enhanced Rate Performance of Al-Doped Li-Rich Layered Cathode Material via Nucleation and Post-solvothermal Method. *ACS Sustain. Chem. Eng.* **6**, 4625–4632

(2018).

14. Schipper, F. *et al.* From Surface ZrO_2 Coating to Bulk Zr Doping by High Temperature Annealing of Nickel-Rich Lithiated Oxides and Their Enhanced Electrochemical Performance in Lithium Ion Batteries. *Adv. Energy Mater.* **8**, (2018).
15. Nayak, P. K., Grinblat, J., Levi, M. & Aurbach, D. Electrochemical and structural characterization of carbon coated $Li_{1.2}Mn_{0.56}Ni_{0.16}Co_{0.08}O_2$ and $Li_{1.2}Mn_{0.6}Ni_{0.2}O_2$ as cathode materials for Li-ion batteries. *Electrochim. Acta* **137**, 546–556 (2014).
16. Nayak, P. K. *et al.* Al Doping for Mitigating the Capacity Fading and Voltage Decay of Layered Li and Mn-Rich Cathodes for Li-Ion Batteries. *Adv. Energy Mater.* **6**, (2016).
17. Dahiya, P. P., Ghanty, C., Sahoo, K., Basu, S. & Majumder, S. B. Suppression of Voltage Decay and Improvement in Electrochemical Performance by Zirconium Doping in Li-Rich Cathode Materials for Li-Ion Batteries. *J. Electrochem. Soc.* **165**, A3114–A3124 (2018).
18. Meng, F. *et al.* Magnesium-doped $Li[Li_{0.2}Mn_{0.54}Ni_{0.13}Co_{0.13}]O_2$ cathode with high rate capability and improved cyclic stability. *Ionics (Kiel).* **25**, 1967–1977 (2019).
19. Liu, Y. *et al.* Improving the electrochemical performances of Li-rich $Li_{1.20}Ni_{0.13}Co_{0.13}Mn_{0.54}O_2$ through a cooperative doping of Na^+ and PO_4^{3-} with Na_3PO_4. *J. Power Sources* **375**, 1–10 (2018).
20. Zhang, H. Z., Qiao, Q. Q., Li, G. R. & Gao, X. P. PO_4^{3-} polyanion-doping for stabilizing Li-rich layered oxides as cathode materials for advanced lithium-ion batteries. *J. Mater. Chem. A* **2**, 7454–7460 (2014).
21. Ahmed, S., Nelson, P. A., Gallagher, K. G., Susarla, N. & Dees, D. W. Cost and energy demand of producing nickel manganese cobalt cathode material for lithium ion batteries. *J. Power Sources* **342**, 733–740 (2017).
22. Schmuch, R., Wagner, R., Hörpel, G., Placke, T. & Winter, M. Performance and cost of materials for lithium-based rechargeable automotive batteries. *Nature Energy* **3**, 267–278 (2018).
23. *COMMITTEE OF THE REGIONS AND THE EUROPEAN INVESTMENT BANK on the Implementation of the Strategic Action Plan on Batteries: Building a Strategic Battery Value Chain in Europe.*
24. *Report on Raw Materials for Battery Applications*.
25. Toby, B. H. & Von Dreele, R. B. GSAS-II: The genesis of a modern open-source all purpose

crystallography software package. *J. Appl. Crystallogr.* **46**, 544–549 (2013).

26. Jarvis, K. A., Deng, Z., Allard, L. F., Manthiram, A. & Ferreira, P. J. Atomic structure of a lithium-rich layered oxide material for lithium-ion batteries: Evidence of a solid solution. *Chem. Mater.* **23**, 3614–3621 (2011).
27. Meng, Y. S. *et al.* Cation ordering in layered O3 $Li[Ni_xLi_{1/3-2x/3}Mn_{2/3-x/3}]O_2$ ($0 \leq x \leq 1/2$) compounds. *Chem. Mater.* **17**, 2386–2394 (2005).
28. Boulineau, A., Croguennec, L., Delmas, C. & Weill, F. Reinvestigation of Li_2MnO_3 structure: Electron diffraction and high resolution TEM. *Chem. Mater.* **21**, 4216–4222 (2009).
29. Hu, E. *et al.* Evolution of redox couples in Li- and Mn-rich cathode materials and mitigation of voltage fade by reducing oxygen release. *Nat. Energy* **3**, 690–698 (2018).
30. Gent, W. E. *et al.* Coupling between oxygen redox and cation migration explains unusual electrochemistry in lithium-rich layered oxides. *Nat. Commun.* **8**, 1–12 (2017).
31. Sathiya, M. *et al.* Reversible anionic redox chemistry in high-capacity layered-oxide electrodes. *Nat. Mater.* **12**, 827–835 (2013).
32. Martha, S. K., Nanda, J., Veith, G. M. & Dudney, N. J. Electrochemical and rate performance study of high-voltage lithium-rich composition: $Li_{1.2}Mn_{0.525}Ni_{0.175}Co_{0.1}O_2$. *J. Power Sources* **199**, 220–226 (2012).
33. Lee, E. S. & Manthiram, A. Smart design of lithium-rich layered oxide cathode compositions with suppressed voltage decay. *J. Mater. Chem. A* **2**, 3932–3939 (2014).
34. Deng, Z. Q. & Manthiram, A. Influence of cationic substitutions on the oxygen loss and reversible capacity of lithium-rich layered oxide cathodes. *J. Phys. Chem. C* **115**, 7097–7103 (2011).
35. Shannon, R. T. & Prewitt, C. T. Effective ionic radii in oxides and fluorides. *Acta Crystallogr. Sect. B Struct. Crystallogr. Cryst. Chem.* **25**, 925–946 (1969).
36. Muhammad, S. *et al.* Evidence of reversible oxygen participation in anomalously high capacity Li- and Mn-rich cathodes for Li-ion batteries. *Nano Energy* **21**, 172–184 (2016).
37. Strehle, B. *et al.* The Role of Oxygen Release from Li- and Mn-Rich Layered Oxides during the First Cycles Investigated by On-Line Electrochemical Mass Spectrometry. *J. Electrochem. Soc.* **164**, A400–A406 (2017).
38. Arunkumar, T. A., Wu, Y. & Manthiram, A. Factors influencing the irreversible oxygen

loss and reversible capacity in layered $Li[Li_{1/3}Mn_{2/3}]O_2$-$Li[M]O_2$ ($M=Mn_{0.5-y}Ni_{0.5-y}Co_{2y}$ and $Ni_{1-y}CO_y$) solid solutions. *Chem. Mater.* **19**, 3067–3073 (2007).

39. Boulineau, A. *et al.* Evolutions of $Li_{1.2}Mn_{0.61}Ni_{0.18}Mg_{0.01}O_2$ during the initial charge/discharge cycle studied by advanced electron microscopy. *Chem. Mater.* **24**, 3558–3566 (2012).
40. Ressler, T., Brock, S. L., Wong, J. & Suib, S. L. Multiple-Scattering EXAFS Analysis of Tetraalkylammonium Manganese Oxide Colloids. *J. Phys. Chem. B* **103**, 6407–6420 (1999).
41. de Groot, F. M. F., Fuggle, J. C., Thole, B. T. & Sawatzky, G. A. 2p x-ray absorption of 3d transition-metal compounds: An atomic multiplet description including the crystal field. *Phys. Rev. B* **42**, 5459–5468 (1990).
42. Gilbert, B. *et al.* Multiple scattering calculations of bonding and X-ray absorption spectroscopy of manganese oxides. *J. Phys. Chem. A* **107**, 2839–2847 (2003).
43. Montoro, L. A., Abbate, M., Almeida, E. C. & Rosolen, J. M. Electronic structure of the transition metal ions in $LiCoO_2$, $LiNiO_2$ and $LiCo_{0.5}Ni_{0.5}O_2$. *Chem. Phys. Lett.* **309**, (1999).
44. Castro, V. Di & Polzonetti, G. XPS Study of MnO Oxidation. *J. Electron Spectros. Relat. Phenomena* **48**, 117–123 (1989).
45. Mohanty, D. *et al.* Structural transformation of a lithium-rich $Li_{1.2}Co_{0.1}Mn_{0.55}Ni_{0.15}O_2$ cathode during high voltage cycling resolved by in situ X-ray diffraction. *J. Power Sources* **229**, 239–248 (2013).
46. Yu, S. H. *et al.* Continuous activation of Li_2MnO_3 component upon cycling in $Li_{1.167}Ni_{0.233}Co_{0.100}Mn_{0.467}Mo_{0.033}O_2$ cathode material for lithium ion batteries. *J. Mater. Chem. A* **1**, 2833–2839 (2013).
47. Song, B. *et al.* Mitigated phase transition during first cycle of a Li-rich layered cathode studied by in operando synchrotron X-ray powder diffraction. *Phys. Chem. Chem. Phys.* **18**, 4745–4752 (2016).
48. Armstrong, A. R. *et al.* Demonstrating Oxygen Loss and Associated Structural Reorganization in the Lithium Battery Cathode $Li[Ni_{0.2}Li_{0.2}Mn_{0.6}]O_2$. (2006). doi:10.1021/ja062027
49. Amalraj, F. *et al.* Integrated Materials $xLi_2MnO_3{\cdot}(1-x)LiMn_{1/3}Ni_{1/3}Co_{1/3}O_2$ (x=0.3, 0.5, 0.7) Synthesized. *J. Electrochem. Soc.* **157**, A1121 (2010).

50. Ruther, R. E., Callender, A. F., Zhou, H., Martha, S. K. & Nanda, J. Raman Microscopy of Lithium-Manganese-Rich Transition Metal Oxide Cathodes. *J. Electrochem. Soc.* **162**, A98–A102 (2015).
51. Grosvenor, A. P., Biesinger, M. C., Smart, R. S. C. & McIntyre, N. S. New interpretations of XPS spectra of nickel metal and oxides. *Surf. Sci.* **600**, 1771–1779 (2006).
52. Payne, B. P., Grosvenor, A. P., Biesinger, M. C., Kobe, B. A. & McIntyre, N. S. Structure and growth of oxides on polycrystalline nickel surfaces. *Surf. Interface Anal.* **39**, 582–592 (2007).
53. Biesinger, M. C. *et al.* Resolving surface chemical states in XPS analysis of first row transition metals, oxides and hydroxides: Cr, Mn, Fe, Co and Ni. *Appl. Surf. Sci.* **257**, 2717–2730 (2011).
54. Assat, G. *et al.* Fundamental interplay between anionic/cationic redox governing the kinetics and thermodynamics of lithium-rich cathodes. *Nat. Commun.* **8**, (2017).
55. Ilton, E. S., Post, J. E., Heaney, P. J., Ling, F. T. & Kerisit, S. N. XPS determination of Mn oxidation states in Mn (hydr)oxides. *Appl. Surf. Sci.* **366**, 475–485 (2016).
56. Galakhov, V. R. *et al.* Mn (formula presented) exchange splitting in mixed-valence manganites. *Phys. Rev. B - Condens. Matter Mater. Phys.* **65**, 1–4 (2002).
57. Verde, M. G. *et al.* Effect of morphology and manganese valence on the voltage fade and capacity retention of $Li[Li_{2/12}Ni_{3/12}Mn_{7/12}]O_2$. *ACS Appl. Mater. Interfaces* **6**, 18868–18877 (2014).
58. Yao, K. P. C. *et al.* Thermal Stability of Li_2O_2 and Li_2O for Li-Air Batteries: In Situ XRD and XPS Studies . *J. Electrochem. Soc.* **160**, A824–A831 (2013).
59. Tanaka, S., Taniguchi, M. & Tanigawa, H. XPS and UPS studies on electronic structure of Li_2O. *Journal of nuclear materials* **283**, 1405 (2000).
60. Jiang, M., Key, B., Meng, Y. S. & Grey, C. P. Electrochemical and structural study of the layered, 'Li-excess' lithium-ion battery electrode material $Li[Li_{1/9}Ni_{1/3}Mn_{5/9}]O_2$. *Chem. Mater.* **21**, 2733–2745 (2009).

3 STUDY OF STRUCTURAL EVOLUTION UPON CYCLING

This chapter focuses on the investigation of LRLOs structure upon cycling. The study is mainly devoted on the changes occurring during the first two cycles by the analysis of XRD patterns and Raman spectra acquired at different points of the charge and discharge steps. We show the modification of the lattice parameters and the existence of a second rhombohedral phase after the first charge. Moreover, we show also the modification on the surface during the charge/discharge.

3.1 INTRODUCTION

The lithium rich materials owe their high capacity to the activation of anodic redox [1–6], as discussed in the previous chapters. This process is uncommon in classical layered oxides and suggest that the large capacity observed arises from the O_2^{4-}/O_2^{2-} electrochemical reaction[6–8]. In the last chapter, I discussed the electrochemical behavior of the synthesized samples, finding a smooth slope below 4.5V, in which the extracted Li^+ are compensated by the oxidation of transition metals ions, and then a voltage plateau[4,6]. During the plateau, the lattice oxygen redox is activated to compensate the extra capacity[5,9].

The existence of lattice oxygen redox reactions has been confirmed by many authors[8,10,11], but the products of that redox are still debated. O_2^{n-} species have been identified in many Lithium Rich materials, but the nature of these species is difficult to reveal due to the complexity of the pristine materials[12,13]. In fact, the nature of the oxidized species depends on the covalence of metal-oxygen bond, the presence of cationic vacancies near the oxygen, the activation of migrations, the existence of electron holes on some oxygen, the metal compositions and so on[6,14–16]. Anyway, the observation of O_2 release during the plateau can be found in many works[10,17–19], and the O_2 evolution is closely connected with the formation of oxygen vacancies in the structure. In this respect, the accumulation of oxygen vacancies promotes cation mixing, stacking faults, segregation of new phases and irreversible change in the oxidation state of metals[20–23]. Moreover, it is not understood if vacancies are a bulk or surface phenomenon and if they can migrate from the surface to the bulk or vice-versa. Therefore, the question is very intricate and, surely,

interplayed with the deterioration of cycling performance[24–26] and the voltage decay upon cycling[27,28], both hindering LRLO market commercialization[29].

From the structural point of view, the degradation mechanisms is not clarified: one of most popular mechanism is a structural shift from the layered to the spinel structure[30,31]. However, other authors describe the degradation with a formation of densified layers[24,32,33].

In the previous chapters, we showed that S10 exhibits a mitigated voltage decay upon prolonged cycling compared to archetypical S01. Through the post mortem X-Ray diffraction analysis, showed in the section 2.4.2, for S01 and S10, we highlight that the diffraction patterns still show the features of a layered materials, but with a lower crystallinity. While the analysis of the local structure of the same post-mortem samples with Raman Spectroscopy (see section 2.4.2), showed formation of spinel-like structure, on the surface overall, less extended in the sample S10 compared to S01.

Here, in order to evaluate the structural evolution of S10, *ex situ* Synchrotron Powder Diffraction experiments have been performed collecting the diffraction patterns of S10 electrodes at different state of charge/discharge. Specifically, in addition to the uncycled pristine materials, three series of electrodes were analyzed:

1. Charged at 4.2V and 4.8V (collected during 1st and 2nd cycles).
2. Discharged at 3.5V and 2V (collected during 1st and 2nd cycles).
3. After 10 cycles in the discharged state.

The same experiments have been carried out on the undoped material $Li_{1.2}Ni_{0.13}Co_{0.13}Mn_{0.54}O_2$ (S01), as a benchmark.

3.2 MATERIALS AND METHODS

Both materials, with/without doping, have been prepared following the synthetic route already discussed in section 2.2. Electrodes have been prepared as composite pellets, assembled into coin-cells and, by galvanostatic cycling, charged and discharged vs. lithium foils using standard electrolytes (LP30). The details of all preparations (electrode discs, coin cell and so on) have been reported in the chapter 2.

At the end of galvanostatic cycling, all coin cells have been de-assembled into Ar-filled glove box and the electrodes recovered, washed in anhydrous dimethyl carbonate (DMC) and tetrahydrofuran (THF) several times. The electrode discs were dried overnight in vacuum, the powder was scratched from the aluminum support and sealed in borosilicate capillary tubes, see figure 3.1. The sealed capillaries are necessary to prevent any contact with ambient atmosphere and to avoid the material degradation. Twenty (20) capillaries have been analyzed and, in particular, 2 pristine samples, 8 for first series, 8 for second series and 2 for third series. Synchrotron diffraction patterns have been collected at Elettra MCX beamline[34] using an energy of 10 KeV (corresponding wavelength of 1.2 Å) and a 2θ resolution of 0.02°.

The time/step ratio has been 5.4 s for pristine materials and 1.8 s for the other samples, therefore the duration of experiments was 8.3 hours for pristine materials and 2.3 hours for the others.

All diffractograms were analyzed by GSAS-II[35] in order to identify the evolution of materials structure upon charge/discharge by Rietveld profile fittings.

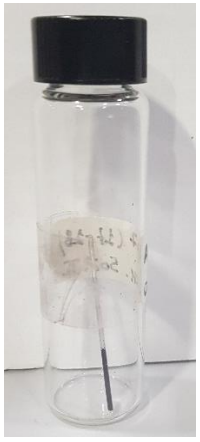

Figure 3.1: Example of sealed capillary used for *ex situ* Analysis.

Ex situ Raman experiments on the same samples series have been recorded using a Dilor microRaman spectrophotometer equipped with HeNe laser and a CCD detector.

3.3 *EX SITU* RAMAN EXPERIMENT

Figure 3.2 shows the *ex situ* Raman spectra for both pristine samples and for the powders in the discharge points, *i.e.* at the end of first and second cycles and after ten cycles.

The pristine materials spectra (black lines in figure 3.2) are consistent with previously reported spectra for LR-NMC and both characteristics vibrational modes of $LiMO_2$ and Li_2MnO_3 components have been identified. As reported in literature[36–39], $LiMO_2$ component with R-3m symmetry has two Raman-active modes, A_{1g} and E_g that can be assigned to the M-O stretching and the O-M-O bending modes. Differently, Li_2MnO_3 component with C2/m symmetry has six Raman-active modes, 4Ag and 2Bg. The most intense peaks around 600 and 480 cm^{-1} belong to R-3m symmetry, (see the blue dash lines in figure 3.2). Whereas all, the other peaks belong to the Li_2MnO_3 component (see the red dash lines). The accurate position of all peaks is reported in the table 3.1.

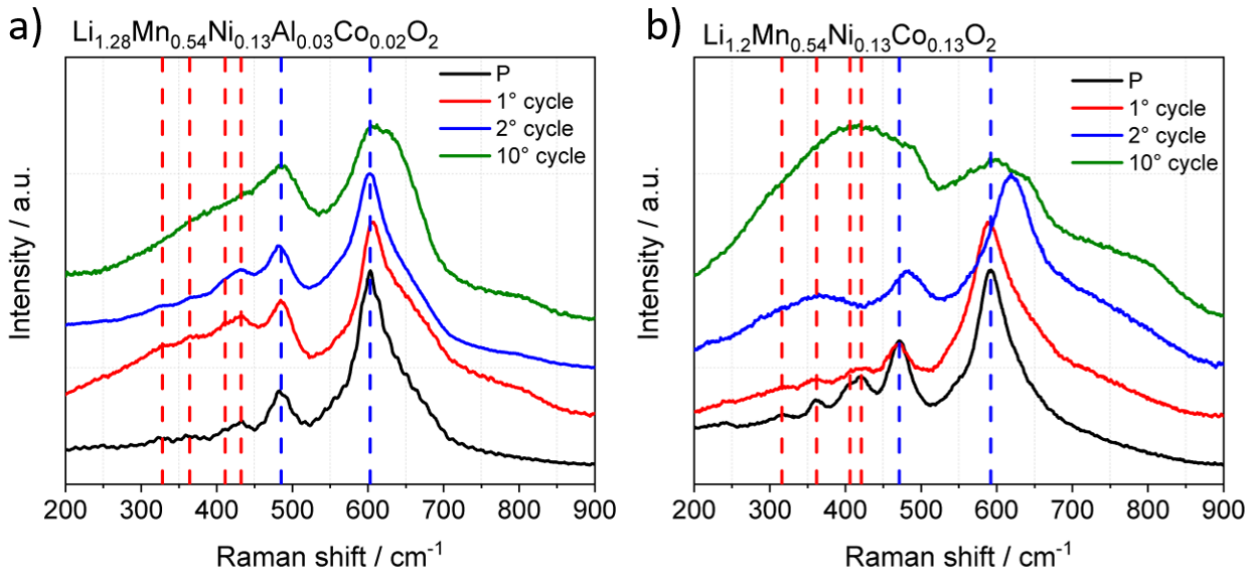

Figure 3.2: *ex situ* Raman spectra of a) S10 and b) S01

The *ex situ* Raman spectra of S10 are shown in the figure 3.2a. Peak positions are unaltered up to the end of the second cycle whereas they enlarge. After ten galvanostatic cycling, the peaks associated with the monoclinic phase tend to disappear (red dotted lines), and the most intense peak at 603 cm^{-1} is split. The peak broadening indicates a more disordered structure, while the peak splitting indicates the emergence of a new phase with a different local structure. Figure 3.2b shows the *ex situ* Raman spectra of S01. After two charge-discharge cycles, the main peaks shifted toward higher Raman shift and it is not possible to distinguish the Li_2MnO_3 component peaks. The green spectrum, after ten galvanostatic cycles, shows a very disordered local structure, in fact the peak around 600 cm^{-1} is very broad with weak intensity.

Table 3.1: Raman peaks position.

S10	**S01**	**Phase**
Peak position (cm^{-1})	**Peak position (cm^{-1})**	
603	592	R-3m
485	471	R-3m
432	421	C2/m
411	406	C2/m
364	362	C2/m
328	316	C2/m

In both samples, the Raman analysis suggests a change in the local structure during the charge-discharge cycling. The disorder increases as confirmed by the peaks broadening, with different extent in the two samples, and a new phase is forming upon cycling at least on the surface of the materials.

3.4 *Ex situ* Diffraction Experiment of sample $Li_{1.2}Mn_{0.54}Ni_{0.13}Co_{0.13}O_2$ (S01)

Figure 3.3 shows the galvanostatic cycling for the first two cycles, in particular the first cycle is the "olive line", the second cycle is the "orange line" and , finally, the green circles indicate the points where the cells have been stopped and the material has been recovered for the analysis. *Ex situ* patterns for the first and second cycle are shown in figure 3.4 and 3.5, respectively. The diffractograms have been collected at two points during the charge step, 4.2 and 4.8V (point A, B, E and F), and at two point during the subsequent discharge, in particular at 3.5 and 2V (point C, D, G and H).

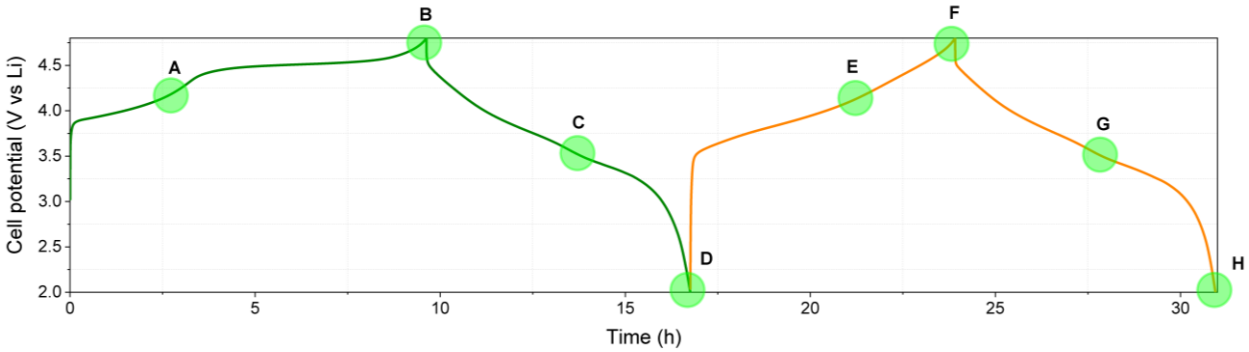

Figure 3.3: First and second charge/discharge curve of S01 and the associated state of charge points studied.

Generally speaking in both cycles, peaks shift to lower angles upon oxidation and to higher angles during the discharge step. Focusing on the fully discharged state (2V), the diffraction peaks do not move back to the original positions, suggesting permanent changes in the crystal structure. Moreover, diffractograms reveal a fast broadening of the peaks upon lithium de-intercalation (see the peak around 14.5° and the peak around 34.4, respectively (003) and (104) indexed with R-3m space group). At the end of the plateau (fully charged state), new peaks can be observed. Structural changes in the second cycle are similar but less intense compared to the first. It is worth noting that the peaks between 15.5° and 21° disappear after the first full charge and they are no longer visible in the subsequent steps.

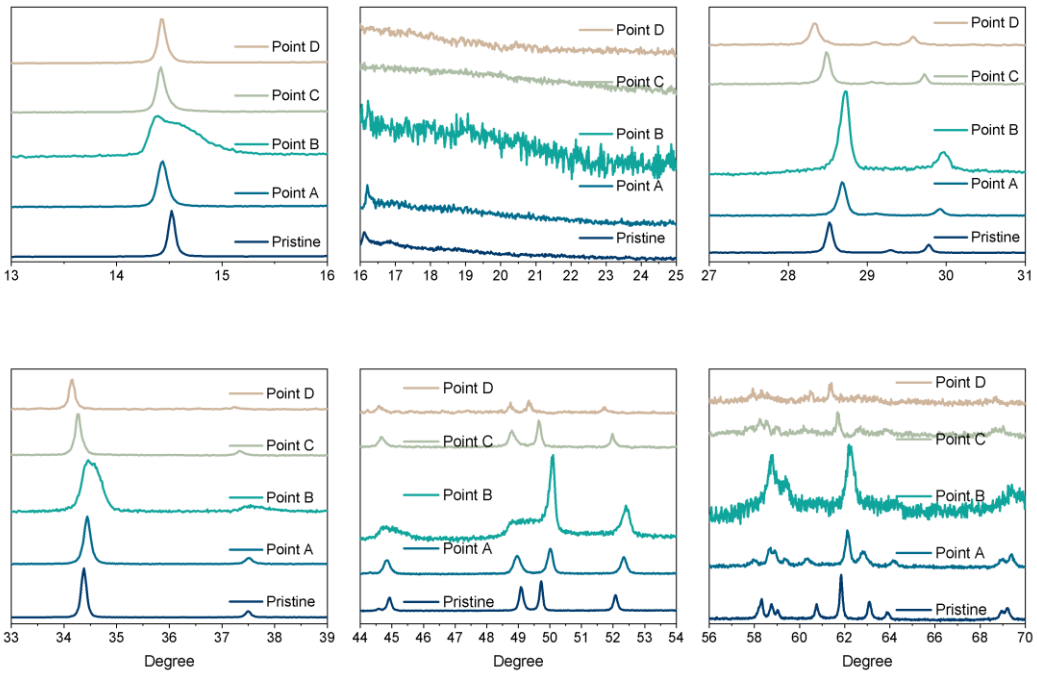

Figure 3.4: Collected Diffraction Pattern of galvanostatic cycling at different points of first cycle.

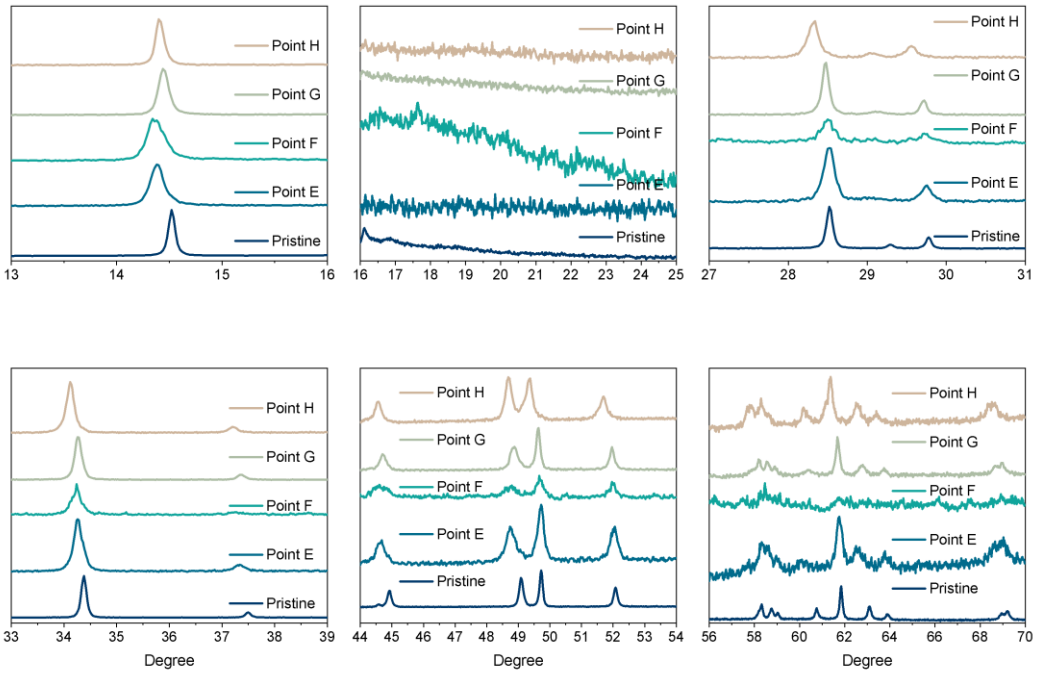

Figure 3.5: Collected Diffraction Pattern of second galvanostatic cycling at different points of second cycle.

Rietveld refinement of the pristine material, using a R-3m symmetry, indicates that it is a typical well layered phase and the cell parameter are 2.854 and 14.239 Å, respectively for *a* and *c*.

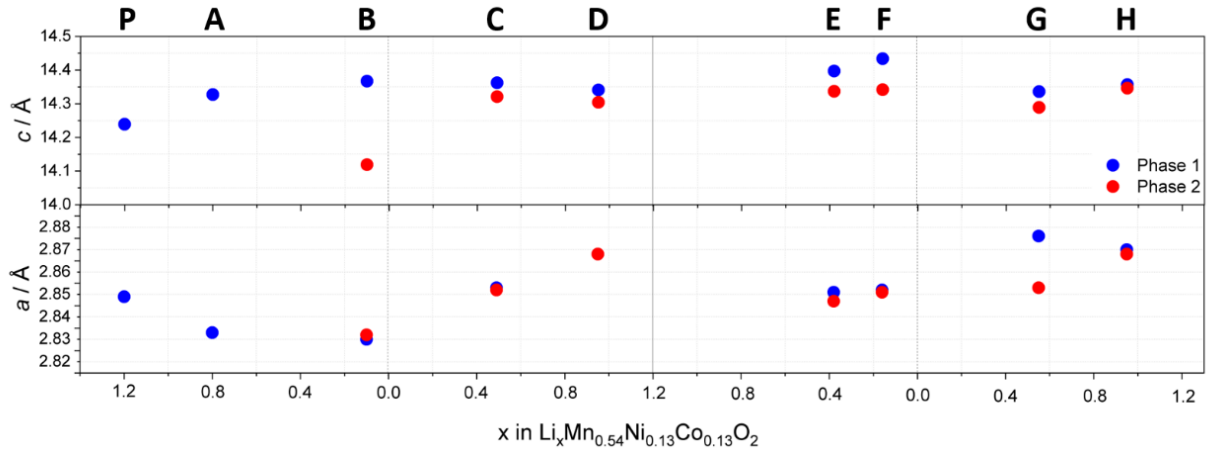

Figure 3.6: Evolution of lattice parameter of S01 during charge-discharge cycling.

Figure 3.6 shows the modification of cell parameter during the first two cycles with the corresponding points in the voltage profiles. The lattice parameters are reported as a function of lithium equivalents, so the blue circle to the left of figure 3.6, corresponding to x=1.2, represents the pristine material. It is possible to follow the modifications during the charge and discharge steps when lithium ions are de-intercalated and re-intercalated into the structure. All lattice refined parameters are reported in table 3.2.

Table 3.2: Refined Lattice Parameters of S01.

			Phase 1		Phase 2	
		Point	a Parameter	c Parameter	a Parameter	c Parameter
	Pristine		2.854	14.239		
1° Cycle	**Charged at 4.2V**	**A**	2.838	14.327	--	--
1° Cycle	**Charged at 4.8V**	**B**	2.835	14.367	2.837	14.119
1° Cycle	**Discharged at 3.5V**	**C**	2.858	14.362	2.857	14.321
1° Cycle	**Discharged at 2V**	**D**	2.873	14.341	2.873	14.304
2° Cycle	**Charged at 4.2V**	**E**	2.856	14.397	2.852	14.337
2° Cycle	**Charged at 4.8V**	**F**	2.857	14.434	2.856	14.342
2° Cycle	**Discharged at 3.5V**	**G**	2.861	14.336	2.858	14.289
2° Cycle	**Discharged at 2V**	**H**	2.881	14.357	2.873	14.346
	After 10 cycles		2.875	14.416	2.869	14.387

At the point A (4.2V) in figure 3.3, the *a* lattice parameter decreases and the *c* lattice parameter increases, this trend can be explained with the oxidation of Ni^{2+} and Co^{3+} to Ni^{4+} and Co^{4+} and Li^{+} removal from the structure[40]. Indeed, the *a* parameter is highly correlated to the average oxidation state of the metals, while, the *c* parameter reflects the increasing electrostatic repulsions between the oxygen layers due to the Li ions removal.

At full charged state (point B), the assumption of a single R-3m phase leads to poor convergence: the experimental pattern appears broaden and new diffraction lines are clearly visible. Improvements in the Rietveld refinement convergence can be obtained by assuming the co-presence of two R-3m coexisting in the charged state. The cell parameters of the new R-3m phase is reported as red dots in figure 3.6. As evident from the figure, the *a* parameter is pretty much the same for both layered phases, indicating a similar mean oxidation states of the transition metal ions in the two phases. On the other hand, the *c* parameters of the two phases are strongly different: the phase 1 in the figure has a *c* parameter very close to the parameter in the point B, but the phase 2 has a smaller *c* parameter.

The formation of a new phase with reduced *c* parameters opens tricky questions. Koga et al[32] justify its formation with a densification process via transition metals migration from the surface to the bulk of the particles. The same authors also suggest that the oxygen vacancies created during the plateau induce stacking faults causing layer gliding and the ordering of a second layered phase.

After charge, we analyzed two other samples in the discharge step, respectively at 3.5V (Point C) and 2V (Point D; fully discharged state). The *a* parameters seem to increase monotonically during the discharge: the average oxidation state of metals varies over the entire discharge step due to the reduction of Ni^{4+} and Co^{4+}, to give Ni^{2+} and Co^{3+}. At the end of discharge, *a* parameters are higher compared to the initial values, indicating irreversible oxidations in the TM blend. Instead, the *c* parameter of phase 1 is unchanged at point C, while it increases for the phase 2 in the fully lithiated state (point D). However, the *c* parameters of the two phases are very close in value. Anyway, both *a* and *c* parameters are greater than the pristine values due to the irreversible changes occurred in the first cycle.

The first charge-discharge cycle is very different to the second cycle, for example the voltage plateau around 4.5V disappears during the second cycle. In order to evaluate the modification occurring after the first cycle in the electrochemical process of this type of materials, we did a full

Rietveld analysis also for the second cycle (see points E, F, G and H in figure 3.3). The results are shown in the second part of figure 3.6. Although the trends of the lattice parameters are similar to those for the initial cycle, the capacity, exchanged at high voltage, is smaller in line with the absence of the voltage plateau. Nevertheless, the limited differences in the cell parameters between the two phases suggest a permanent phase segregation. The *a* parameter of phase 2 is slightly smaller than a of phase 1, probably because the phase 2 has less Li^+ ions in the metals layers. This difference has an impact also on the evolution of *c* parameters during the lithiation and de-lithiation steps.

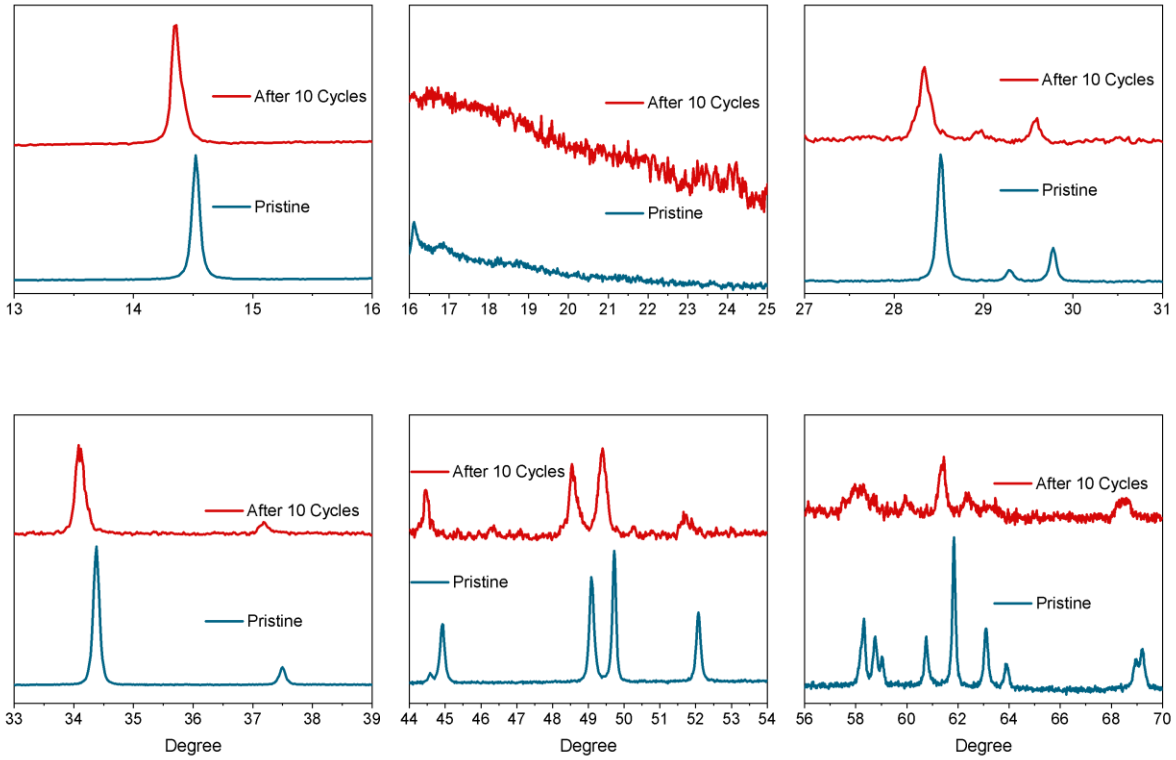

Figure 3.7: *ex situ* diffraction patter of S01 after ten charge/discharge cycles. Pristine material is added as a comparison.

X-ray diffraction pattern of the material following 10 electrochemical cycles are shown in Figure 3.7. The collected diffractograms have been refined with two R-3m cells and both layered phases show an expanded lattice in *c* direction. Surprisingly the *a* parameters are smaller than the full discharged material after two cycles. All profile fits for Rietveld refinement of Synchrotron X-Ray Diffraction are showed in figures 3.8 and 3.9.

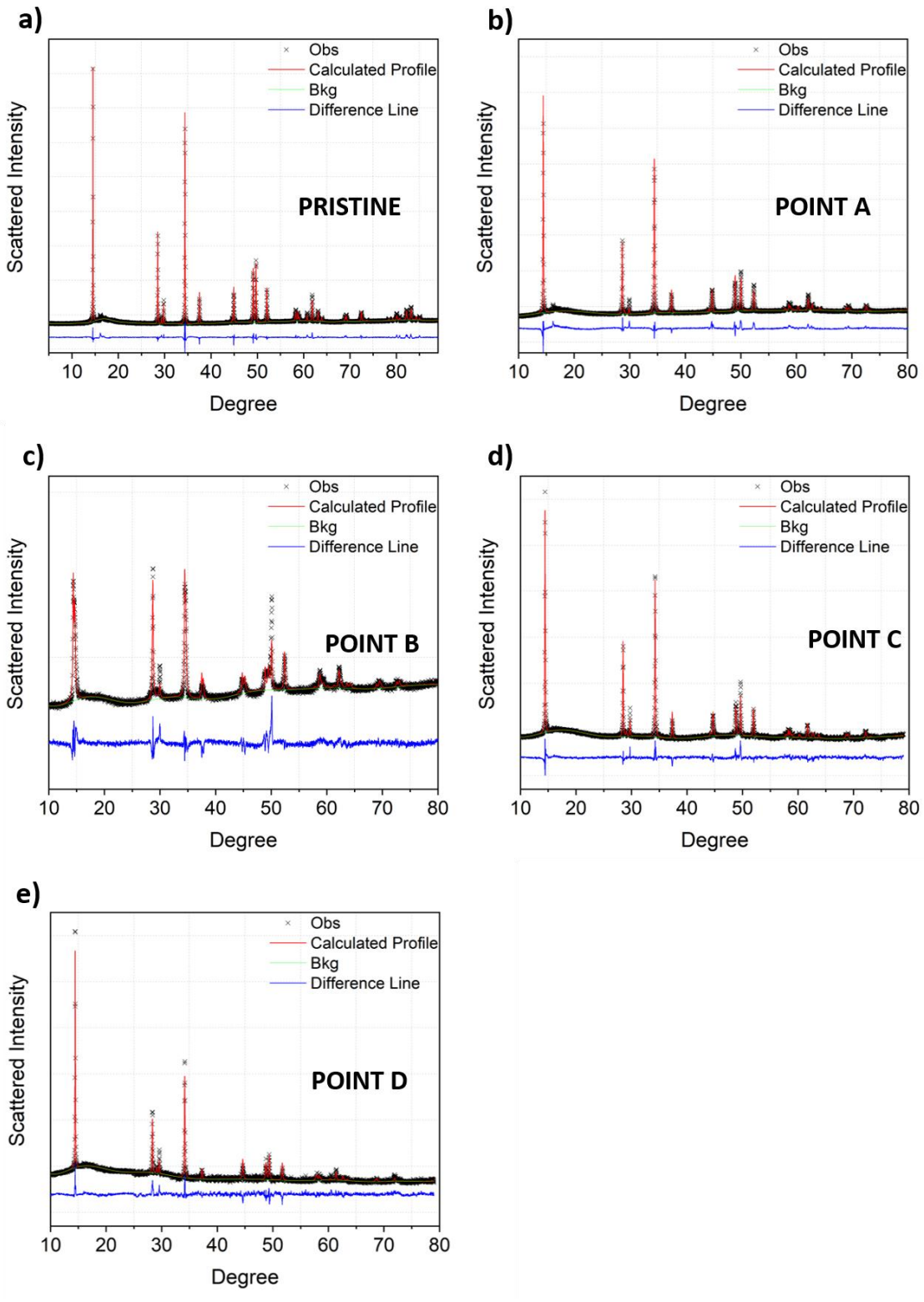

Figure 3.8: Rietveld Refinement of S01. a) Pristine sample, b) charged to 4.2V 1°cycle, c) charged to 4.8V 1°cycle, d) discharged to 3.5V 1°cycle, e) discharged to 2V 1°cycle.

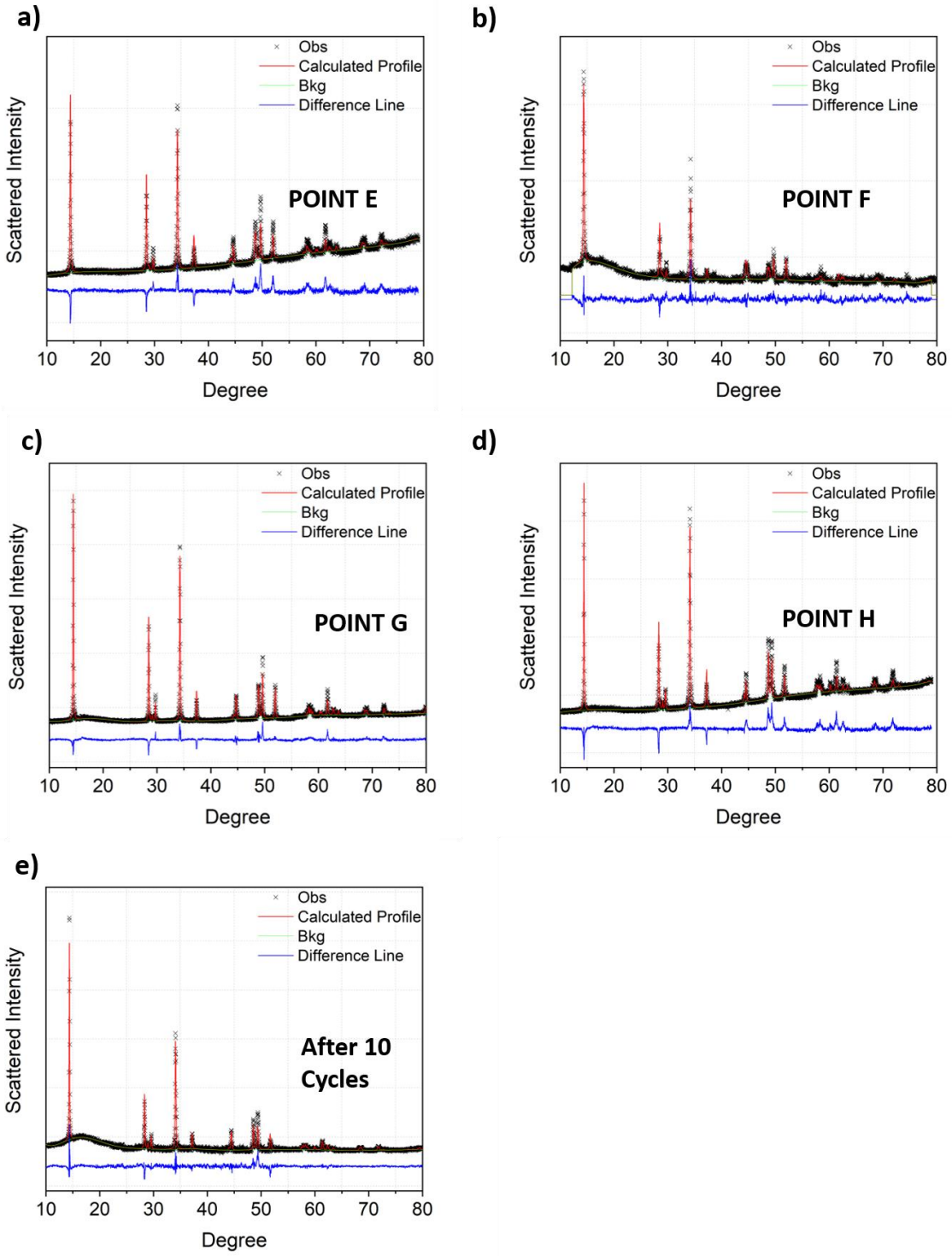

Figure 3.9: Rietveld Refinement of S01. a) charged to 4.2V 2°cycle, b) charged to 4.8V 2°cycle, c) discharged to 3.5V 2°cycle, d) discharged to 2V 2°cycle and e) after 10 cycles.

3.5 *EX SITU* DIFFRACTION EXPERIMENT OF SAMPLE $Li_{1.28}Mn_{0.54}Ni_{0.13}Co_{0.02}Al_{0.03}O_2$ (S10)

The *ex situ* diffraction experiment has been repeated for S10 in the same conditions of previous material, therefore we have two points during the charge, 4.2 and 4.8V, and two points during the discharge, 3.5 and 2V for the first two cycles and the full discharged samples after ten cycles.

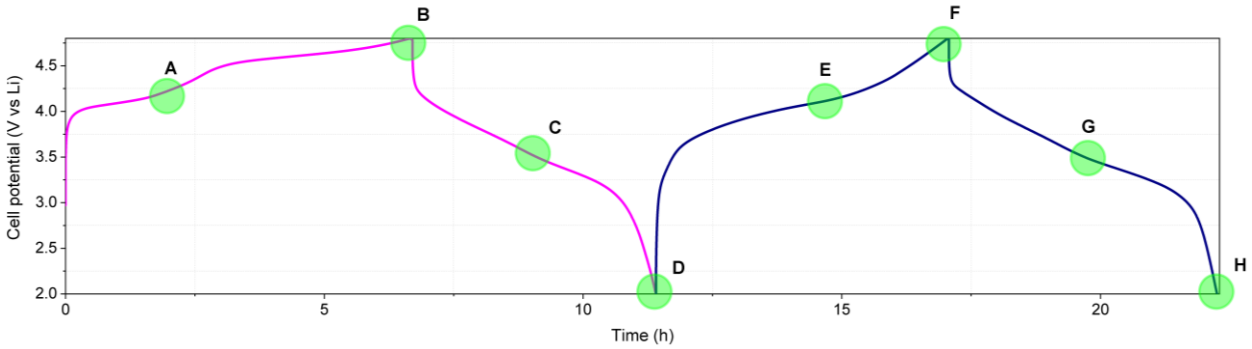

Figure 3.10: First and second charge/discharge curve of S10 and the associated state of charge points studied.

Figure 3.10 shows the galvanostatic two cycling, reporting the voltage of the cell vs the time. The green circles indicate the points in which the cell has been stopped to recover the material. The points A, B, E and F represent different charge states for the first and second cycles, while the remaining points, C, D, G and H, indicate the discharge states.

The collected pattern are showed in figures 3.11 and 3.12, respectively for the first and second cycle. It is interesting to note that the peaks, connected with monoclinic phase in the range between 15.5° and 21°, don't disappear during the first charge, and they are still clearly visible until the end of the second cycle. This phenomenon reveals that a partial ordering between Li ions and metals ions is preserved during the cycling. Generally speaking, the different patterns show modifications of the peaks position during charge-discharge steps and, at the end of the first charge, the appearance of a new phase. Looking at the first discharge and the second cycle, the patterns suggest that these two phases modify in parallel upon lithium extraction and insertion.

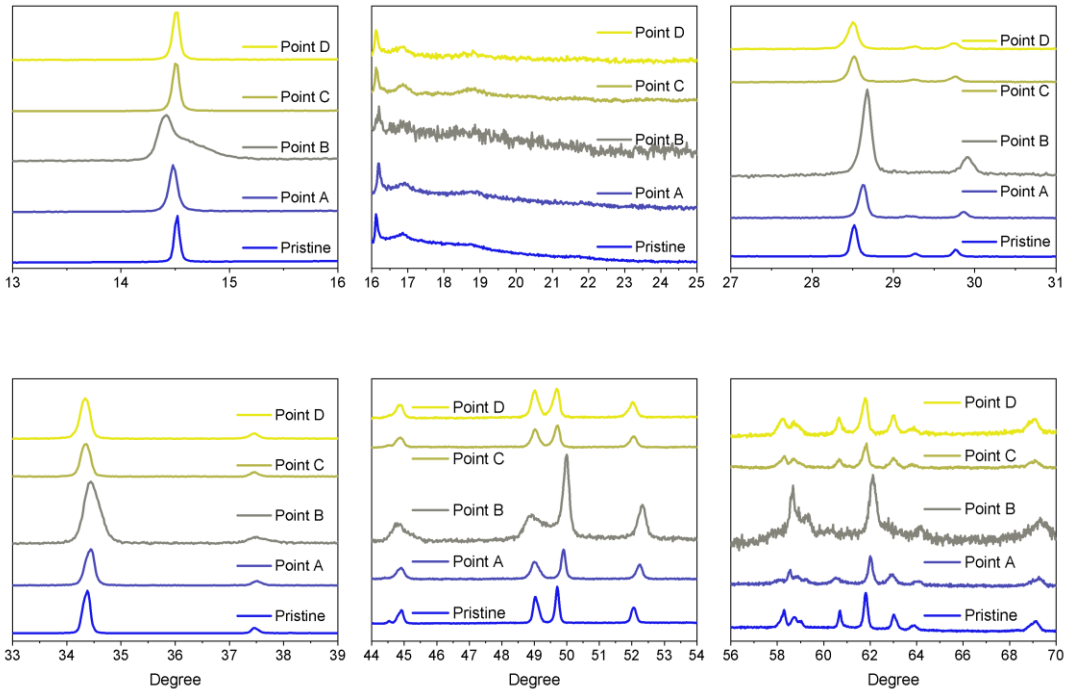

Figure 3.11: Collected Diffraction Pattern of first galvanostatic cycling at different points.

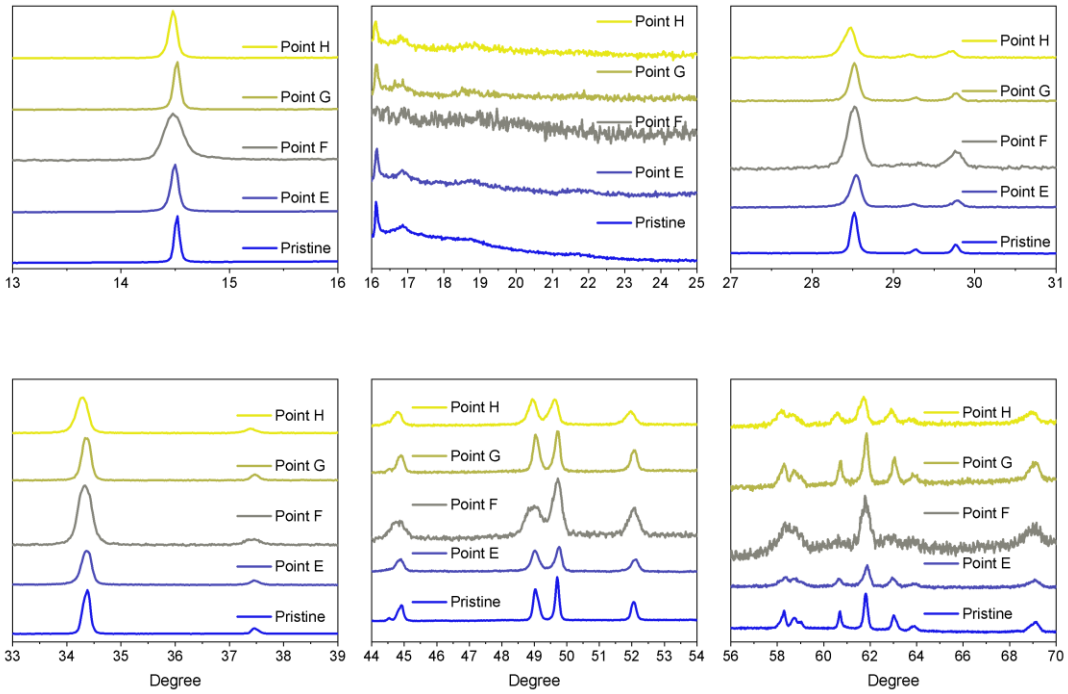

Figure 3.12: Collected Diffraction Pattern of second galvanostatic cycling at different points.

As in the previous section, the 2θ positions at the end of the first cycle, and also at the end of the second cycle, are not the same as the pristine material. Therefore, the sample undergoes irreversible structural changes during the charge-discharge cycling. Looking at the main reflections, the peak around 14.5° (003 reflection) shifts toward lower 2θ values at the point B and its width begins to broaden. When the charge potential reaches 4.8V (point C), a new phase is present and then, gradually, the (003) peak goes back to higher 2θ values during the discharge (points D and E in the galvanostatic cycling). For the (104) peak around 34.4°, it can be found that, with the charging potential increasing, the peak moves to higher degree and to the opposite direction during the discharge, again with a fast broadening of the width.

Rietveld refinement of the pristine material with R-3m symmetry leads to lattice parameters 2.855 and 14.248 Å, respectively for *a* and *c*. The cell charged up to 4.2V (point B) shows the presence of a second layered phase with R-3m already at this point. This second phase could be related to the oxygen vacancies in the pristine material (see section 2.4.1), which could trigger ions migrations or other process. Therefore, a second phase is added throughout the analysis.

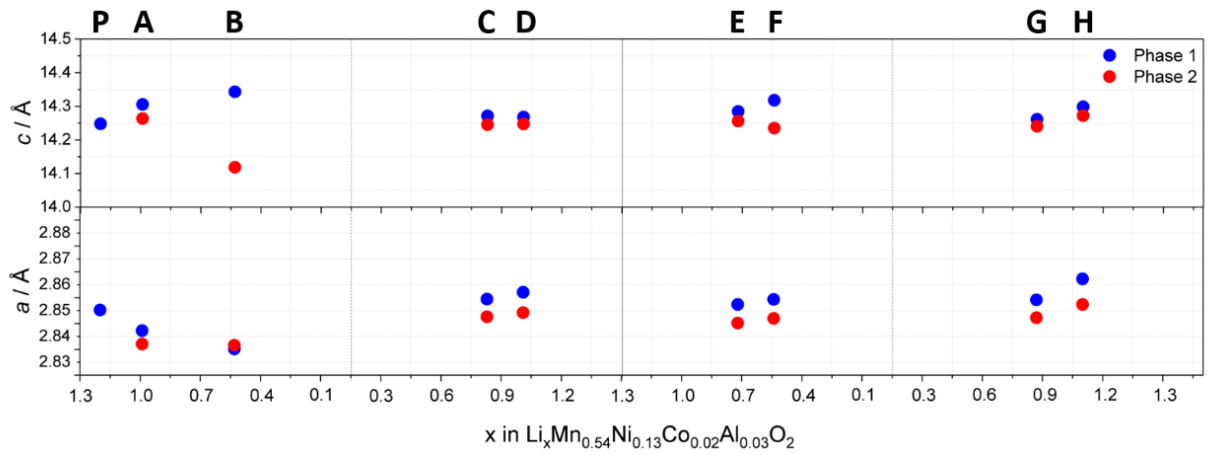

Figure 3.13: Evolution of lattice parameter during charge-discharge cycling.

The evolution of lattice parameters during the experiment is shown in figure 3.13, while the calculated lattice parameters are shown in table 3.3.

Table 3.3 Refined Lattice Parameters of S10.

		Phase 1		Phase 2	
		a Parameter	c Parameter	a Parameter	c Parameter
	Pristine	2.855	14.248		
1° Cycle	**Charged at 4.2V**	2.847	14.306	2.842	14.264
	Charged at 4.8V	2.840	14.343	2.842	14.118
	Discharged at 3.5V	2.859	14.272	2.853	14.245
	Discharged at 2V	2.862	14.268	2.854	14.247
2° Cycle	**Charged at 4.2V**	2.857	14.285	2.850	14.256
	Charged at 4.8V	2.859	14.318	2.855	14.235
	Discharged at 3.5V	2.859	14.261	2.852	14.240
	Discharged at 2V	2.867	14.298	2.857	14.272
	After 10 cycles	2.895	14.431	2.880	14.367

The *a* parameter for both phases decreases during the charge process, according to the oxidation of Ni^{2+} and Co^{3+} to Ni^{4+} and Co^{4+} and the changes in their ionic radii. The *c* parameter reduces its value and, at 4.8 V, in the case of phase 2 it shrinks down to 14.1 Å. The sample collected during the discharge, points C and D, shows a reverse trend, *i.e.* increase of *a* and decrease of *c* parameters, due to the reduction of the metals and reinsertion of lithium ions. In fact, the metals increases their ionic radii, expanding the a-b plane, and the intercalation of lithium reduces the repulsion between oxygen layers, compressing the unit cell in c direction. Regarding the second cycle, the lattice parameters show the same behavior, despite the smaller exchanged capacity. Refined phase fractions exhibit that the two phases interconvert into each other during the cycling.

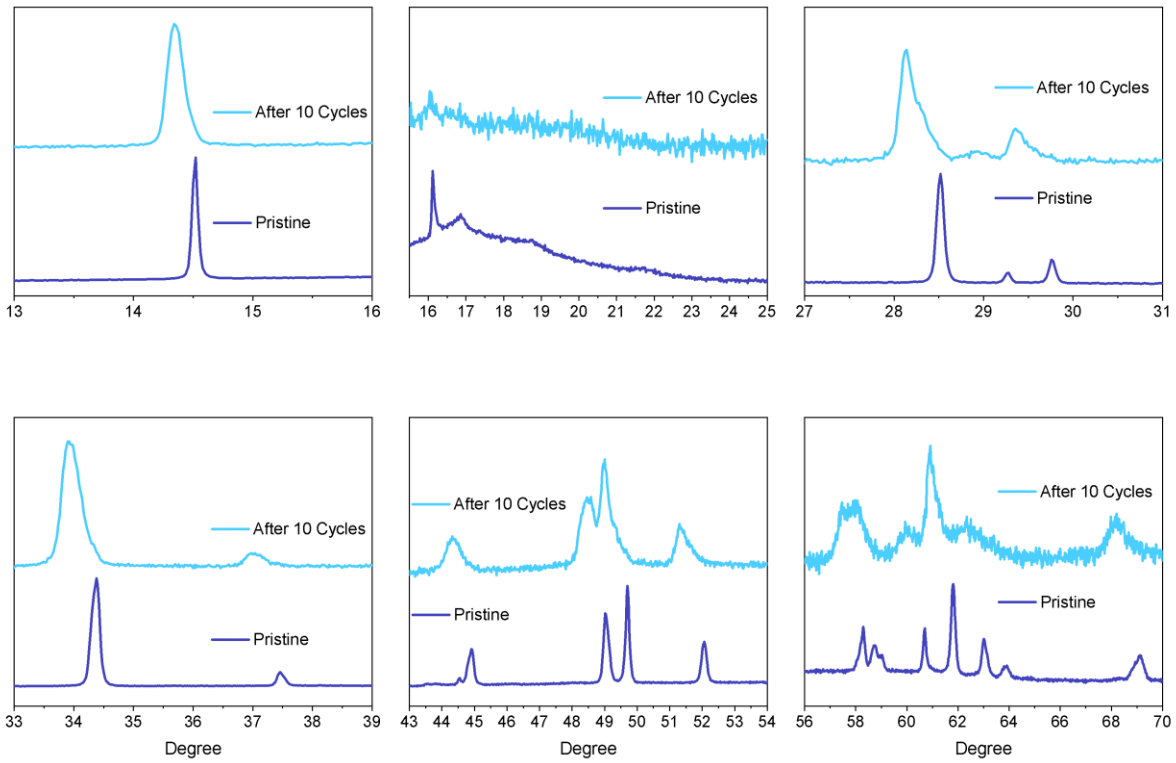

Figure 3.14: *ex situ* diffraction patter of S10 after ten charge/discharge cycles. Pristine material is added as a comparison.

Besides the analysis in the firsts two cycles, the S10 electrodes have been collected also after 10 cycles and recovered for the diffraction analysis. The results are shown in figure 3.14, the pristine pattern was added as a comparison. Again the material has been analyzed by Rietveld Refinement, using two R-3m unit cell. Both unit cells are bigger than last ones in both directions.

The figures 3.15 and 3.16 shows a summary of obtained profile fits for S10.

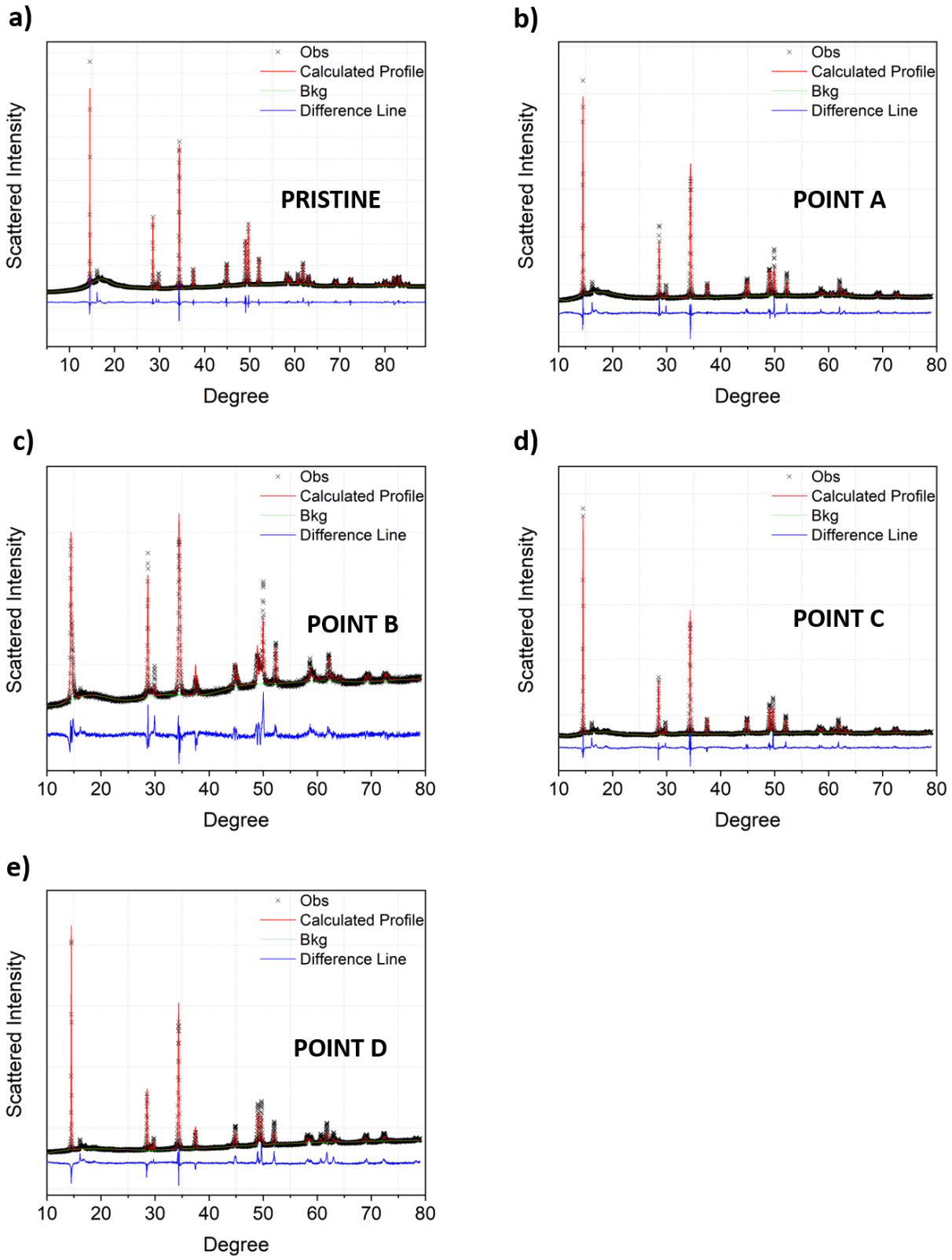

Figure 3.15: Rietveld Refinement of S10. a)Pristine sample, b)charged to 4.2V 1°cycle, c) charged to 4.8V 1°cycle, d)discharged to 3.5V 1°cycle, e) discharged to 2V 1°cycle.

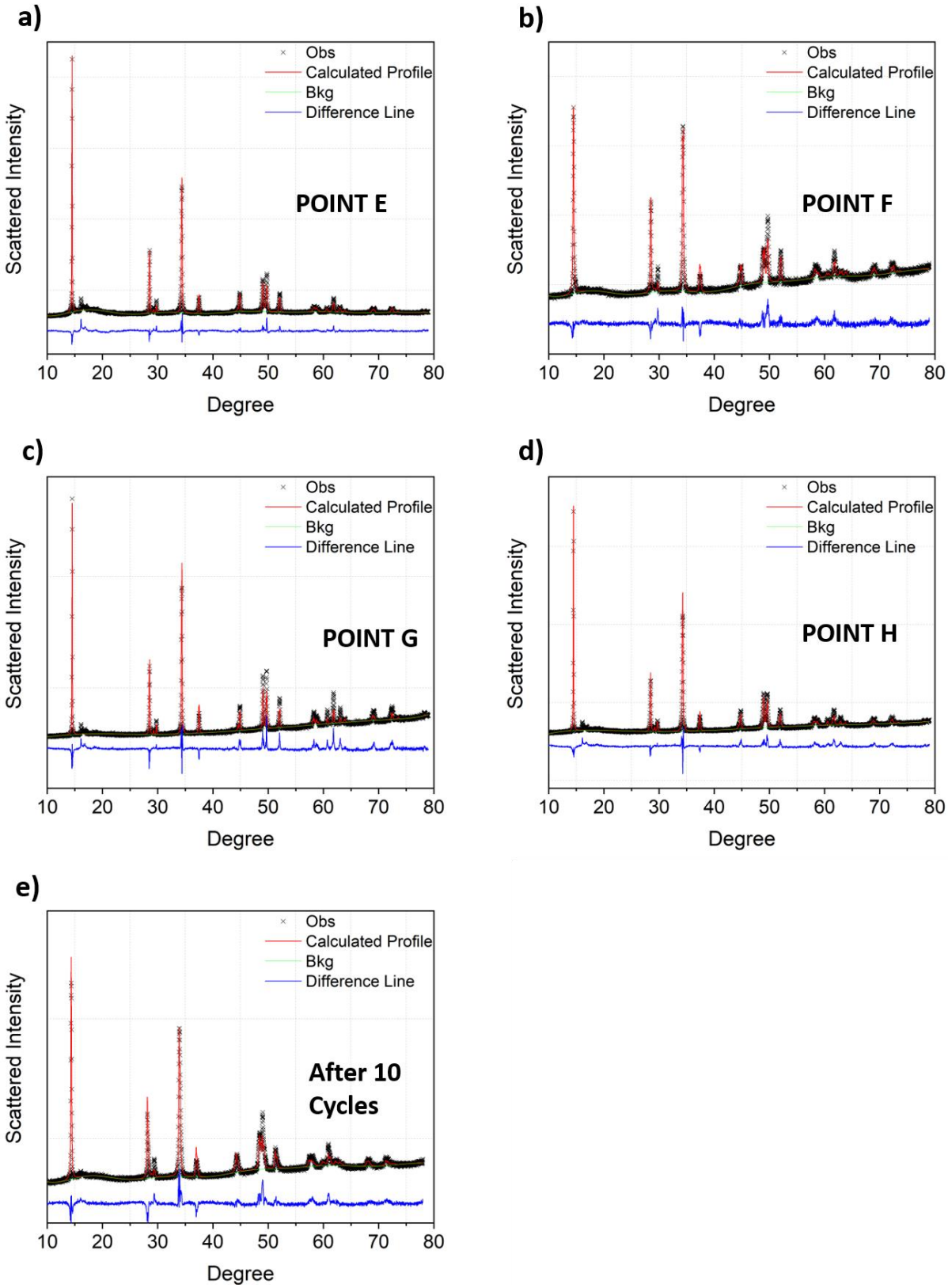

Figure 3.16: Rietveld Refinement of S10. a)charged to 4.2V 2°cycle, b) charged to 4.8V 2°cycle, c)discharged to 3.5V 2°cycle, d) discharged to 2V 2°cycle and e)after 10 cycles.

3.6 CONCLUSION

Raman and XRD *ex situ* analysis allow us to monitor the structural evolution of cathode materials during galvanostatic cycling. In particular, the modifications occurring in $Li_{1.28}Ni_{0.13}Co_{0.02}Mn_{0.54}Al_{0.03}O_2$ (S10) and $Li_{1.28}Ni_{0.13}Co_{0.13}Mn_{0.54}O_2$ (S01) samples have been investigated.

In general, the main modifications occur in the first electrochemical cycle and in particular during the first charge. The first charge can be divided in two distinct regions, an initial step before the plateau (<4.5V) and a plateau around 4.5-4.6V. In the charge of the sample S10 up to 4.2V, the diffractograms show very broad peaks with two possible isostructural phases; thus, the refinement has been done assuming two R-3m lattices. This behavior is in contrast with the refinement of S01 in the same state of charge where we observe a single phase. A possible explanation is the presence of native oxygen vacancies in S10 sample, which could promote ion migration processes leading to the segregation of a new phase. The sample S01 exhibits significant changes in the structure only in the fully charged state (4.8V). These changes possibly involve oxygen ionic sublattice by direct oxidation or O_2 loss. Generally speaking, up to 4.2V, the lithium ions are extracted from the structure while Ni and Co are oxidized, thus leading to shifts in the cell parameters in both samples. As noted above, both S01 and S10 at 4.8V show two distinct phases. The segregation phase takes place in the first charge and it is irreversible: the new phase remains in the subsequent cycles for both samples and, from this point, the two phases interconvert while the lithium ions are extracted or inserted into the structure.

It is worth to note a difference between two samples. The superlattice peaks disappear and never reappear for S01. However, they are still visible at the end of the second cycle for S10, suggesting that the ordering in transition metals layers is disrupted by the de-lithiation for S01 but not for S10. During the discharge process, the materials incorporate lithium ions and the lattice parameters move back close to the original values. The values of lattice parameters reported in table 3.2 and 3.3 indicate that the recovering of the original structure is better in S10 compared to S01. This trend is even more evident at the end of the second cycle. These results are consistent with the *ex situ* Raman spectroscopy analysis. At the end of second cycle, the S10 spectrum broadens but the position of main peaks is the same. In contrast, the S01 spectrum appears very broaden and with shifts in main peaks. Therefore, the local structure of S01 is much more altered upon cycling

compared to S10. As in the *ex situ* XRD patterns, the Raman spectra confirm also that the peaks associated with the monoclinic structure are still visible for the S10 but not for S01.
After ten cycles, the local structure of both materials appears more disordered with shifted peaks possibly in the range of spinel structure.

REFERENCES

1. Pan, H. *et al.* Li- and Mn-rich layered oxide cathode materials for lithium-ion batteries: A review from fundamentals to research progress and applications. *Molecular Systems Design and Engineering* **3**, 748–803 (2018).
2. Tan, S., Ji, Y. J., Zhang, Z. R. & Yang, Y. Recent progress in research on high-voltage electrolytes for lithium-ion batteries. *ChemPhysChem* **15**, 1956–1969 (2014).
3. Assat, G., Delacourt, C., Corte, D. A. D. & Tarascon, J.-M. Editors' Choice—Practical Assessment of Anionic Redox in Li-Rich Layered Oxide Cathodes: A Mixed Blessing for High Energy Li-Ion Batteries. *J. Electrochem. Soc.* **163**, A2965–A2976 (2016).
4. Wang, J. *et al.* Lithium- and Manganese-Rich Oxide Cathode Materials for High-Energy Lithium Ion Batteries. *Adv. Energy Mater.* **6**, (2016).
5. Muhammad, S. *et al.* Evidence of reversible oxygen participation in anomalously high capacity Li- and Mn-rich cathodes for Li-ion batteries. *Nano Energy* **21**, 172–184 (2016).
6. Gent, W. E. *et al.* Coupling between oxygen redox and cation migration explains unusual electrochemistry in lithium-rich layered oxides. *Nat. Commun.* **8**, 1–12 (2017).
7. Armstrong, A. R. *et al.* Demonstrating Oxygen Loss and Associated Structural Reorganization in the Lithium Battery Cathode $Li[Ni_{0.2}Li_{0.2}Mn_{0.6}]O_2$. (2006). doi:10.1021/ja062027
8. Sathiya, M. *et al.* Reversible anionic redox chemistry in high-capacity layered-oxide electrodes. *Nat. Mater.* **12**, 827–835 (2013).
9. Susai, F. A. *et al.* Horizons for Li-Ion Batteries Relevant to Electro-Mobility: High-Specific-Energy Cathodes and Chemically Active Separators. *Advanced Materials* **30**, (2018).
10. Strehle, B. *et al.* The Role of Oxygen Release from Li- and Mn-Rich Layered Oxides during the First Cycles Investigated by On-Line Electrochemical Mass Spectrometry. *J. Electrochem. Soc.* **164**, A400–A406 (2017).
11. Laha, S. *et al.* Oxygen-participated Electrochemistry of New Lithium-rich Layered Oxides Li_3MRuO_5 (M = Mn, Fe). *Phys. Chem. Chem. Phys.* **17**, 3749–3760 (2015).
12. Oishi, M. *et al.* Direct observation of reversible charge compensation by oxygen ion in Li-rich manganese layered oxide positive electrode material, $Li_{1.16}Ni_{0.15}Co_{0.19}Mn_{0.50}O_2$. *J.*

Power Sources **276**, 89–94 (2015).

13. Zhao, S., Yan, K., Zhang, J., Sun, B. & Wang, G. Reaction Mechanisms of Layered Lithium-Rich Cathode Materials for High-Energy Lithium-Ion Batteries. *Angewandte Chemie - International Edition* **60**, 2208–2220 (2021).
14. Luo, K. *et al.* Charge-compensation in 3d-transition-metal-oxide intercalation cathodes through the generation of localized electron holes on oxygen. *Nat. Chem.* **8**, 684–691 (2016).
15. Seo, D. H. *et al.* The structural and chemical origin of the oxygen redox activity in layered and cation-disordered Li-excess cathode materials. *Nat. Chem.* **8**, 692–697 (2016).
16. Li, X. *et al.* Direct Visualization of the Reversible O^{2-}/O^{-} Redox Process in Li-Rich Cathode Materials. *Adv. Mater.* **30**, (2018).
17. Lu, Z. & Dahn, J. R. Understanding the Anomalous Capacity of Li/Li[$Ni_xLi_{(1/3-2x/3)}Mn_{(2/3-x/3)}O_2$ Cells Using In Situ X-Ray Diffraction and Electrochemical Studies. *J. Electrochem. Soc.* **149**, A815 (2002).
18. Armstrong, A. R., Robertson, A. D. & Bruce, P. G. Overcharging manganese oxides: Extracting lithium beyond Mn^{4+}. in *Journal of Power Sources* **146**, 275–280 (2005).
19. La Mantia, F., Rosciano, F., Tran, N. & Novák, P. Direct evidence of oxygen evolution from $Li_{1+x}(Ni_{1/3}Mn_{1/3}Co_{1/3})_{1-x}O_2$ at high potentials. *J. Appl. Electrochem.* **38**, 893–896 (2008).
20. Cui, S. L., Wang, Y. Y., Liu, S., Li, G. R. & Gao, X. P. Evolution mechanism of phase transformation of Li-rich cathode materials in cycling. *Electrochim. Acta* **328**, (2019).
21. Boulineau, A., Simonin, L., Colin, J. F., Bourbon, C. & Patoux, S. First evidence of manganese-nickel segregation and densification upon cycling in Li-rich layered oxides for lithium batteries. *Nano Lett.* **13**, 3857–3863 (2013).
22. Gao, Y., Wang, X., Ma, J., Wang, Z. & Chen, L. Selecting substituent elements for Li-rich Mn-based cathode materials by Density Functional Theory (DFT) calculations. *Chem. Mater.* **27**, 3456–3461 (2015).
23. Hu, E. *et al.* Evolution of redox couples in Li- and Mn-rich cathode materials and mitigation of voltage fade by reducing oxygen release. *Nat. Energy* **3**, 690–698 (2018).
24. Fell, C. R. *et al.* Correlation between oxygen vacancy, microstrain, and cation distribution in lithium-excess layered oxides during the first electrochemical cycle. *Chem. Mater.* **25**,

1621–1629 (2013).

25. Croy, J. R. *et al.* Examining hysteresis in composite $xLi_2MnO_3 \cdot (1-x)LiMO_2$ cathode structures. *J. Phys. Chem. C* **117**, 6525–6536 (2013).
26. Qiu, B. *et al.* Gas-solid interfacial modification of oxygen activity in layered oxide cathodes for lithium-ion batteries. *Nat. Commun.* **7**, (2016).
27. Sathiya, M. *et al.* Origin of voltage decay in high-capacity layered oxide electrodes. *Nat. Mater.* **14**, 230–238 (2015).
28. Lee, E. S. & Manthiram, A. Smart design of lithium-rich layered oxide cathode compositions with suppressed voltage decay. *J. Mater. Chem. A* **2**, 3932–3939 (2014).
29. Zheng, J. *et al.* Li- and Mn-Rich Cathode Materials: Challenges to Commercialization. *Advanced Energy Materials* **7**, (2017).
30. Gu, M. *et al.* Formation of the spinel phase in the layered composite cathode used in Li-Ion batteries. *ACS Nano* **7**, 760–767 (2013).
31. Hong, J. *et al.* Structural evolution of layered $Li_{1.2}Ni_{0.2}Mn_{0.6}O_2$ upon electrochemical cycling in a Li rechargeable battery. *J. Mater. Chem.* **20**, 10179–10186 (2010).
32. Koga, H. *et al.* Different oxygen redox participation for bulk and surface: A possible global explanation for the cycling mechanism of $Li_{1.20}Mn_{0.54}Co_{0.13}Ni_{0.13}O_2$. *J. Power Sources* **236**, 250–258 (2013).
33. Yin, W. *et al.* Structural evolution at the oxidative and reductive limits in the first electrochemical cycle of $Li_{1.2}Ni_{0.13}Mn_{0.54}Co_{0.13}O_2$. *Nat. Commun.* **11**, (2020).
34. Rebuffi, L., Plaisier, J. R., Abdellatief, M., Lausi, A. & Scardi, A. P. MCX: A synchrotron radiation beamline for X-ray diffraction line profile analysis. *Zeitschrift fur Anorg. und Allg. Chemie* **640**, 3100–3106 (2014).
35. Toby, B. H. & Von Dreele, R. B. GSAS-II: The genesis of a modern open-source all purpose crystallography software package. *J. Appl. Crystallogr.* **46**, 544–549 (2013).
36. Lanz, P., Villevieille, C. & Novák, P. Ex situ and in situ Raman microscopic investigation of the differences between stoichiometric $LiMO_2$ and high-energy $xLi_2MnO_3 \cdot (1-x)LiMO_2$ (M = Ni, Co, Mn). *Electrochim. Acta* **130**, 206–212 (2014).
37. Ruther, R. E., Callender, A. F., Zhou, H., Martha, S. K. & Nanda, J. Raman Microscopy of Lithium-Manganese-Rich Transition Metal Oxide Cathodes. *J. Electrochem. Soc.* **162**, A98–A102 (2015).

38. Wu, Q. *et al.* A Raman-Based Investigation of the Fate of Li_2MnO_3 in Lithium- and Manganese-Rich Cathode Materials for Lithium Ion Batteries . *J. Electrochem. Soc.* **162**, A1255–A1264 (2015).
39. Venkateswara Rao, C. *et al.* Investigations on electrochemical behavior and structural stability of $Li_{1.2}Mn_{0.54}Ni_{0.13}Co_{0.13}O_2$ lithium-ion cathodes via in-situ and ex-situ Raman spectroscopy. *J. Phys. Chem. C* **118**, 14133–14141 (2014).
40. Shannon, R. T. & Prewitt, C. T. Effective ionic radii in oxides and fluorides. *Acta Crystallogr. Sect. B Struct. Crystallogr. Cryst. Chem.* **25**, 925–946 (1969).

4 STRUCTURAL INVESTIGATION OF OVER-LITHIATED LI-RICH LAYERED OXIDES

The chapter is devoted to the understanding of the pristine structure of over-lithiated Li-Rich materials, mainly with the use of supercells and with the introduction of stacking faults. We demonstrate the successfully use of the R_C_3b supercell to fit XRD and ND patters. The lattice parameter *b* of R_C_3b is three times larger compared to the monoclinic unit cell. Moreover, we describe and quantify the stacking defect within the material.

4.1 INTRODUCTION

The crystal structure of LRLO is an open playground of debate[1,2]. There are two main hypotheses: a) a two phase nano-domain[3,4] and b) a single phase solid solution[5,6].
Under the "nano-domain" hypotheses, LRLOs are composed by two coexisting phases, namely, a trigonal $LiTMO_2$ phase (space group R-3m), and a monoclinic Li_2MnO_3 phase (space group C2/m). A visualization of both structure is shown in figure 4.1.

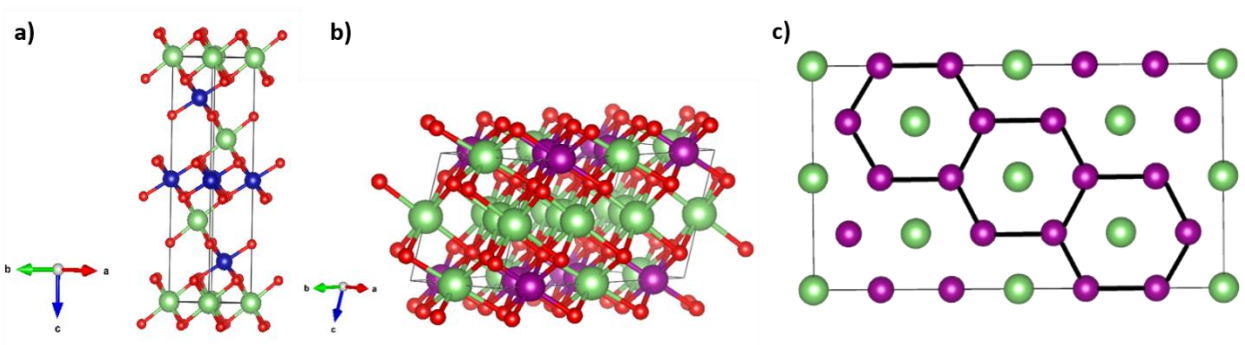

Figure 4.1: Representation of a) R-3m and b) C2/m unit cell. c) Superlattice ordering in the TM layer of Li_2MnO_3.

$LiTMO_2$ belongs to the trigonal crystal class with R-3m (166) space group symmetry, in which the structure can be visualized as alternating O-Li-O and O-TM-O layers[6,7]. This kind of structure is well-known because the stoichiometric layered materials, such as LiCoO2, crystalize in these prototypal lattices [8]. A NMC materials can be derived by substituting Co with Mn and/or Ni, resulting in TM layers with randomly distributed metals[9–11]. Instead, Li_2MnO_3 structure belongs to

the monoclinic crystal class with C2/m (12) space group symmetry[12–15]. Actually, the C2/m unit cell is similar to that of rhombohedral because both are made up of alternating O-Li-O and O-TM-O layers, stacked along the c direction. However, the excess of Li resides in the TM-layer and occupies one-third of the TM sites. Indeed the formula of Li_2MnO_3 refers to a crystal structure that can be represented as $Li[Li_{1/3}Mn_{2/3}]O_2$, this partial occupancy form $LiMn_6$ honeycomb motifs, in which each Li is surrounded by six Mn[16,17]. The honeycomb ordering reduces the symmetry from R-3m to C2/m: a pictorial representation is shown in figure 4.1c. To take into account the two different phases, the general formula of Lithium-Rich materials can be expressed as $xLi_2MnO_3 \bullet (1-x)LiNi_xCo_yMn_zO_2$[4]. Under the solid solution hypothesis, the crystal structure is a randomic solid solution with formula $Li_{1+x}[NiCoMn]_{1-x}O_2$, with C2/m local symmetries broken to the R-3m trigonal ones after few unit cells within the same crystallite. In fact, the monoclinic and rhombohedral unit cells are very similar and a unique structure is not established[18–20]. Furthermore, other parameters, such as synthesis methods, annealing temperature, stoichiometry, lithium excess, have an impact on the final structure of the material[21–23]. The complexity of these structures is increased by the large number of defects[23–25], in particular stacking faults easily occurs when the oxygen periodicity is broken along the c direction (*i.e.* the stacking direction).

Therefore, Rietveld refinements of X-Ray diffractograms are very challenging. In fact, the use of a R-3m unit cell allows to fit all the pattern peaks, except for the superlattice peaks located between 20-30° (with Cu Kα wavelength), while the use of C2/m cell is able to fit all the pattern but the results are not completely satisfactory due to the differences in intensity between the calculated and experimental patterns, especially in the superstructure peaks. A different approach is to use a monoclinic structure incorporating stacking faults, to mimic the anisotropic broadening of some specific Bragg reflections in the XRD patterns, in particular, superstructure reflections[23,26].

In this section the structure of over-lithiated Li-Rich layered oxides has been investigated, exploring the possibility that the unit cell has a certain periodicity along one or more lattice directions. For this purpose, the material formulation presented in chapter 2, $Li_{1.28}Mn_{0.54}Ni_{0.13}Co_{0.02}Al_{0.03}O_2$ (S10), has been analyzed by synchrotron X-Ray diffraction and Neutron diffraction. The collected patterns have been refined by the classical unit cell, rhombohedral and monoclinic to further investigate the degree of stacking faults. After that, several supercells have been used to refine the synchrotron and neutron pattern. Finally, the best

supercell has been employed for $Li_{1.2}Mn_{0.54}Ni_{0.13}Co_{0.13}O_2$ (S01) and $Li_{1.25}Mn_{0.625}Ni_{0.125}O_2$ (S12) to check the extent of traceability of this structural hypothesis.

4.2 MATERIALS AND METHODS

S01, S10 and S12 have been prepared as reported in chapter 2. X-Ray Diffraction patterns have been acquired at the MCX beamline[27] in the ELETTRA synchrotron radiation source, using a wavelength of 1.2 Å (10 KeV) in the 2θ range = 5°- 90° with a step size of 0.01°.
Neutron powder diffraction data have been collected on the time-of-flight instrument Polaris at the ISIS neutron and muon source[28] and the samples have been loaded into open, cylindrical 6mm vanadium can. Refinements of Synchrotron X-Ray and Neutron patterns have been performed with GSAS-II[29] and FAULTS[30]. Synchrotron diffractogram of S10 has been analyzed with several unit cells created with PowderCell Software[31]. Starting from a classical Rhombohedral unit cell, we have been downgraded the symmetry to the primitive monoclinic unit cell. After that, the possible larger unit cell built as supercells along one or more lattice directions have been explored, without symmetry degradation. An overview of all unit cells explored are reported in table 4.1 and in figure 4.2. It worth to note that the last column of table 4.1 illustrates the applied transformation to make the supercells.

Table 4.1: Summary of unit cells created with PowderCell Software.

Name	Structural Model	Lattice Parameter				Transformation
		a	b	c	β	
R	Rhombohedral	2.8524	2.8524	14.24	90	
R_C	Monoclinic	9.6352	2.8524	5.0243	151.02	$a = \frac{2}{3}a_R + \frac{1}{3}b_R - \frac{2}{3}c_R$ $b = b_R$ $c = \frac{2}{3}a_R + \frac{1}{3}b_R + \frac{1}{3}c_R$
R_C_3a	Monoclinic	28.9055	2.8524	5.0243	151.02	$a = 3a_{R\_C}$ $b = b_{R\_C}$ $c = c_{R\_C}$
R_C_3b	Monoclinic	9.6352	8.5572	5.0243	151.02	$a = a_{R\_C}$ $b = 3b_{R\_C}$ $c = c_{R\_C}$
R_C_3c	Monoclinic	9.6352	2.8524	15.073	151.02	$a = a_{R\_C}$ $b = b_{R\_C}$ $c = 3c_{R\_C}$
R_C_3a_3b	Monoclinic	28.9055	8.5572	5.0243	151.02	$a = 3a_{R\_C}$ $b = 3b_{R\_C}$ $c = c_{R\_C}$
R_C_3a_b_a+c	Monoclinic	28.9055	2.8524	5.7775	24.916	$a = 3a_{R\_C}$ $b = b_{R\_C}$ $c = a_{R\_C} + c_{R\_C}$

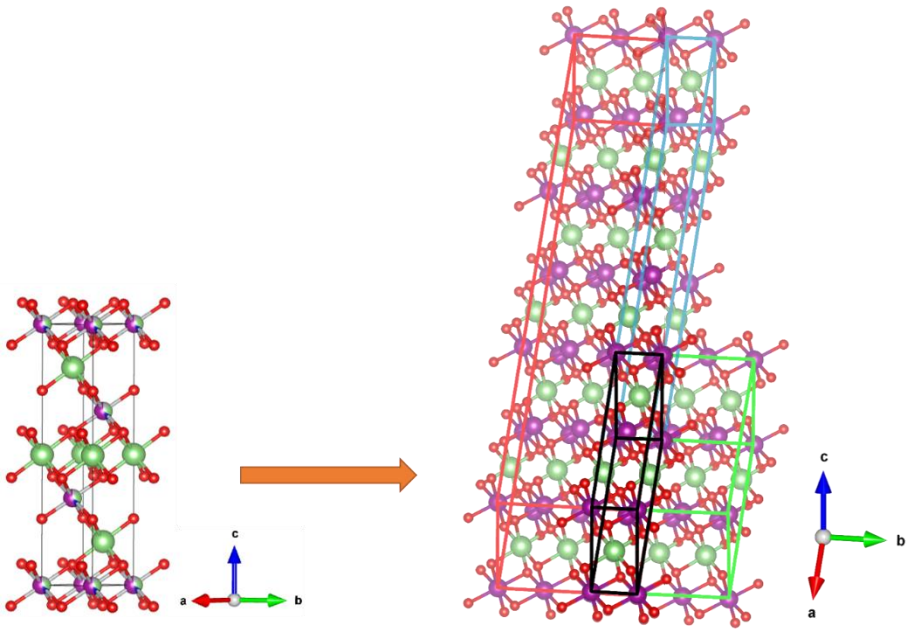

Figure 4.2: The initial rhombohedral unit cell is reported on the left, while, on the right, you can see the monoclinic one (black line) and some supercell and how it is related to the supercells.

The stacking fault simulations of Li_2TMO_3 monoclinic prototype and the refinement of X-ray data have been performed with DIFFaX[32] and FAULTS softwares. XRD patterns were simulated over 10 – 80° (2θ) with a step size of 0.02° and a wavelength of 1.2 Å. For the use of DIFFaX and FAULTS, the conventional monoclinic unit cell was transformed into the triclinic system with P1 space group. The crystals can be seen in terms of atomic sheets (layers), which can be interconnected via stacking operations occurring with a certain probability. Therefore, stacking defects can be described as different layer types and/or transition vectors. Abraham et al.[33] found that the stacking faults in LRLOs can be properly describe with the help of 3 different stacking vectors.

Table 4.2 Details of the structure model used for DIFFaX and FAULTS.

Unit cell parameters					
a, b (Å)		c (Å)		γ (°)	
4.9265		4.7416		60.036	
Layer compositions					
Layer	Atom	x/a	y/b	z/c	Occupancy
L1	Li	0	0	0	1
	Li	1/3	1/3	0	1
	Li	2/3	2/3	0	1
L2=L3=L4	Li	0	0	0	0.84
	TM	0	0	0	0.16
	TM	1/3	1/3	0	1
	TM	2/3	2/3	0	1
	O	0.34	0	0.225	1
	O	0.65	0	-0.225	1
	O	0	0.34	-0.225	1
	O	0.34	0.35	-0.225	1
	O	0.65	0.34	0.225	1
	O	0	0.65	0.225	1
Stacking Vectors					
Transition		x/a	x/b		x/c
L1→L2		1/3	-1/3		1/2
L1→L3		2/3	0		1/2
L1→L4		0	-2/3		1/2
L2→L1		1/3	-1/3		1/2
L3→L1		1/3	-1/3		1/2
L4→L1		1/3	-1/3		1/2

According to the stacking description reported by Serrano et al[34], 2 different layers were built: 1) Li layer (L1) and 2) Li-TM-O layer (L2). With the use of the 3 different stacking vectors, 2 extra Li-Mn-O layers (L3 and L4) were obtained. Table 4.2 summarizes all the operations applied to the structure model. While, in table 4.3, the probability of layers occurrence and the corresponding stacking degree are given.

Table 4.3: Translation vectors with their probabilities and the corresponding stacking fault probabilities.

	Translation Vectors			**Stacking Fault probability (%)**
	(1/3 -1/3 1/2)	**(2/3 0 1/2)**	**(0 -2/3 1/2)**	
Translation probabilities	1	0	0	0
	0.9333	0.033	0.033	10
	0.866	0.067	0.067	20
	0.8	0.1	0.1	30
	0.733	0.133	0.133	40
	0.667	0.167	0.167	50
	0.6	0.2	0.2	60
	0.533	0.233	0.233	70
	0.467	0.267	0.267	80
	0.4	0.3	0.3	90
	0.333	0.333	0.333	100

4.3 FAILURE OF CONVENTIONAL STRUCTURAL MODEL

The diffractogram of S10 is shown in figure 4.3 with the reference patterns PDF 01-085-6632 (Li_2MnO_3) and PDF 04-013-4592 ($LiMO_2$). Most of the peaks can be indexed based on the R-3m structure except for the peaks between 15° and 26°, which can only be indexed based on the monoclinic C2/m structure[1,35,36]. Therefore, the X-ray diffraction pattern exhibits the features of two different structural models. The HR-TEM analysis confirms the monoclinic local crystal structures of the sample (see figures 4.4): indeed, the electron diffraction patterns reconstructed by

FFTs are indexed by the C2/m structure. Therefore, both the analysis, XRD and TEM, shows a very complex structural identity of this material.

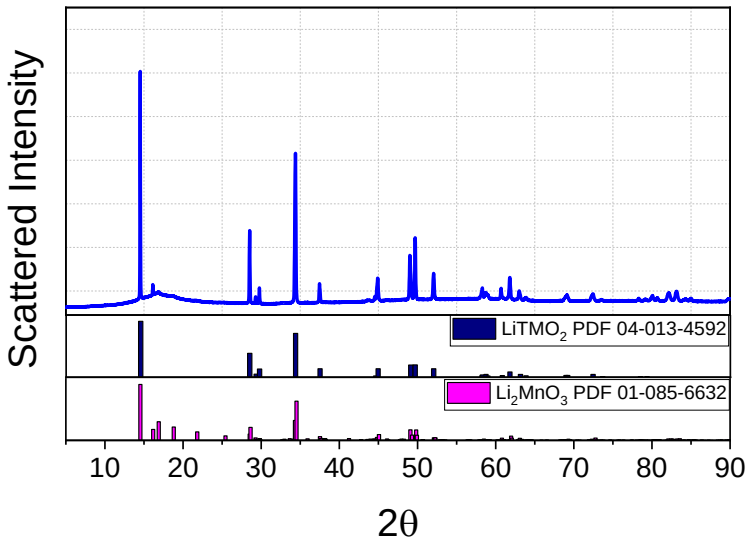

Figure 4.3: Synchrotron Collected Pattern of S10. PDF cards 01-013-4592 ($LiTMO_2$) and 01-085-6632 (Li_2MnO_3) are used as references.

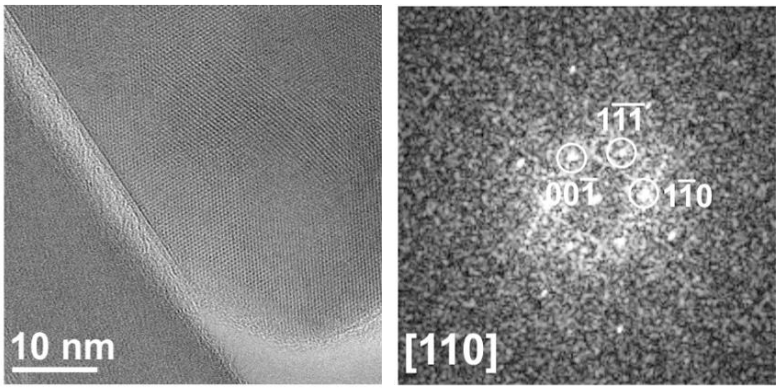

Figure 4.4 a) HR-TEM image and b) corresponding FFT. The reconstructed FFT is indexed with C2/m structure.

In order to understand how the Rietveld refinement changes, synchrotron XRD pattern of S10 has been fitted by the use of both R-3m and C2/m unit cells. The analysis has been performed with GSAS-II and figure 4.5 shows the results obtained with the rhombohedral and monoclinic structure. The wR is a parameter that measures the agreement between the crystallographic model

and the experimental X-Ray diffraction data. The wR values are 6.9% and 9.3%, respectively for R-3m and C2/m.

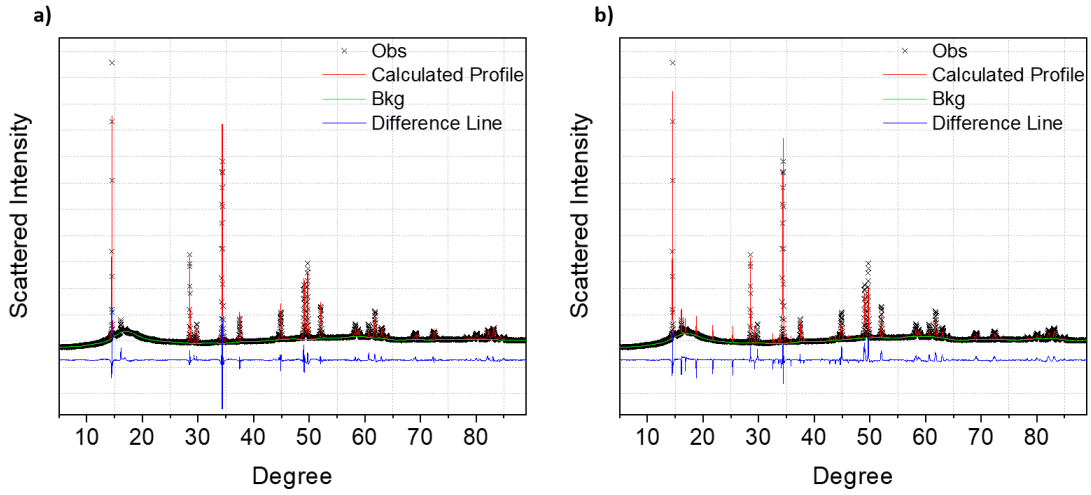

Figure 4.5: Comparison of Rietveld refinement results using a) R-3m and b) C2/m phase.

The first structure exhibits a slight better wR value, although it is not able to fit the superstructure peaks between 15° and 26° (see figure 4.5a). On the other hand, the C2/m structure fits all peaks present in the pattern, but the calculated intensities and shapes of the superstructure peaks are completely wrong (figure 4.5b). Details of refined structural parameters are reported in table 4.4. This analysis suggests that both these conventional structures are not appropriate but the diffractogram shows the characteristics of two unit cells.

Table 4.4: Rietveld refined parameters for R-3m and C2/m unit cell.

Space group	**C 2/m (wR=9.3%)**	**R-3m (wR=6.9%)**
Lattice parameters	a=4.948 b=8.563 c=5.031 α=γ=90° β=109.29°	a=b=2.855 c=14.248 α=β=90° γ=120°
Atomic position and occupancies (Wycoff position; OF=occupancy fraction)		
Lithium ion layer	(2c) (0 0 ½) OF(Li)=1 (4h) (0 0.661 ½) OF(Li)=1	(3b) (0 0 ½) OF=1
Metal ions blend layer	(2b) (0 ½ 0) OF(Li)=0.84 OF(TM)=0.16 (4g) (0 0.167 0) OF(TM)=1	(3a) (0 0 0) OF(Li)=0.28 OF(TM)=0.72
Oxygen ions layers	(4i) (0.272 0 0.247) OF(O)=1 (8j) (0.230 0.344 0.219) OF(O)=1	(6c) (0 0 0.738) OF=1

In order to improve the structural models, anti-site defects and Li-TM site mixing in TM layers were added in the Rhombohedral and monoclinic unit cells, respectively. The introduction of anti-site defects around 1% allows to improve slightly the wR parameter (see section 2.4.1). Moving to the Li-TM site mixing in the monoclinic cell, the results are shown in figure 4.6. The calculated pattern for the intense peaks is almost the same after the introduction of defects, but an evident improvement is visible in the superstructure region. The wR drops from 9.3% to 4.7%, indicating a better representation of the structure, and the new refined parameters are reported in table 4.5. According to the different multiplicity of the sites and using constrains for the total occupancies, a migration of lithium ions from 2b site to 4g site is obtained with a reverse movement of TM metals. As a consequence, the superstructure peaks decrease in intensity and the convergence improves.

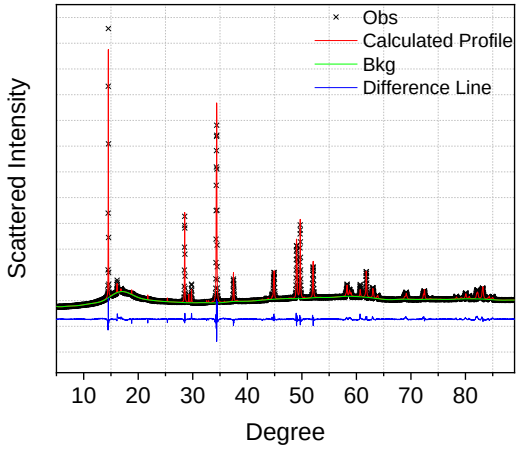

Figure 4.6: Changes in the Rietveld refinement using C2/m phase after the introduction of Li-TM site mixing in TM layers.

Table 4.5: Rietveld refined parameters for C2/m unit cell with Li-TM site mixing.

Space group	**C 2/m (wR=4.7%)**
Lattice parameters	a=4.948 b=8.563 c=5.031 α=γ=90° β=109.29°
Atomic position and occupancies (Wycoff position; OF=occupancy fraction)	
Lithium ion layer	(2c) (0 0 ½) OF(Li)=1
	(4h) (0 0.661 ½) OF(Li)=1
Metal ions blend layer	(2b) (0 ½ 0) OF(Li)=0.51 OF(TM)=0.49
	(4g) (0 0.167 0) OF(Li)=0.17 OF(TM)=083
Oxygen ions layers	(4i) (0.242 0 0.212) OF(O)=1
	(8j) (0.229 0.335 0.223) OF(O)=1

Nevertheless, the representation of superstructure region is still poor. To better describe its structural features, we tested two different approaches: supercells structural model and stacking faults. The experimental details are reported in the following sections.

4.4 APPLICATION OF SUPERCELLS STRUCTURAL MODELS

The last section highlights the complexity of LRLO structures. In order to improve the Rietveld analysis, we tested superlattices with C2/m symmetry to fit the XRD patterns. The highly symmetric rhombohedral unit cell, used in section 4.3, has been used as a starting point and its symmetry has been broken to the primitive C2/m cell by using the PowderCell software. The new unit cell has a monoclinic symmetry and, starting from this primitive cell, we identified 5 supercells with the same symmetry (see table 4.1). The possibility of a larger lattice parameter is not meaningless, keeping in mind that the transition-metal layer can assume various atomic arrangements of Mn, Li, Co, Al and Ni and that this possible atomic arrangement could have a partial ordering.

4.4.1 Synchrotron Diffraction

All the supercells have been used as starting points to refine the synchrotron collected pattern of S10: fit results are shown in figure 4.7. Some of those supercells show peaks in the region between 15° and 26°, thanks to the reduced symmetry whereas the pristine C2/m and R-3m cells failed.
Certainly, we obtained the best results with the supercells that are able to fit the superstructure peaks as shown in the summary of refined lattice parameter and wR values in table 4.6. The details of atomic positions for all cells are reported in table 4.7.
In particular, the R_C_3b structural model exhibits the best wR value, the lattice parameter *b* is three times larger compared to the monoclinic unit cell and this allows to mimic better the superstructure along the TM layers.

Table 4.6: Refined Lattice parameters and wR values.

Name	Lattice Parameter				wR (%)
	a	b	c	β	
R	2.855	2.855	14.248	90	6.9
R_C	9.645	2.857	5.024	151	5
R_C_3a	28.934	2.857	5.024	151.02	5.05
R_C_3b	9.636	8.564	5.032	151.02	4.22
R_C_3c	9.645	2.856	15.069	151.01	4.86
R_C_3a_3b	28.935	8.57	5.024	151.01	4.72
R_C_3a_b_a+c	28.936	2.856	5.788	24.876	5.06

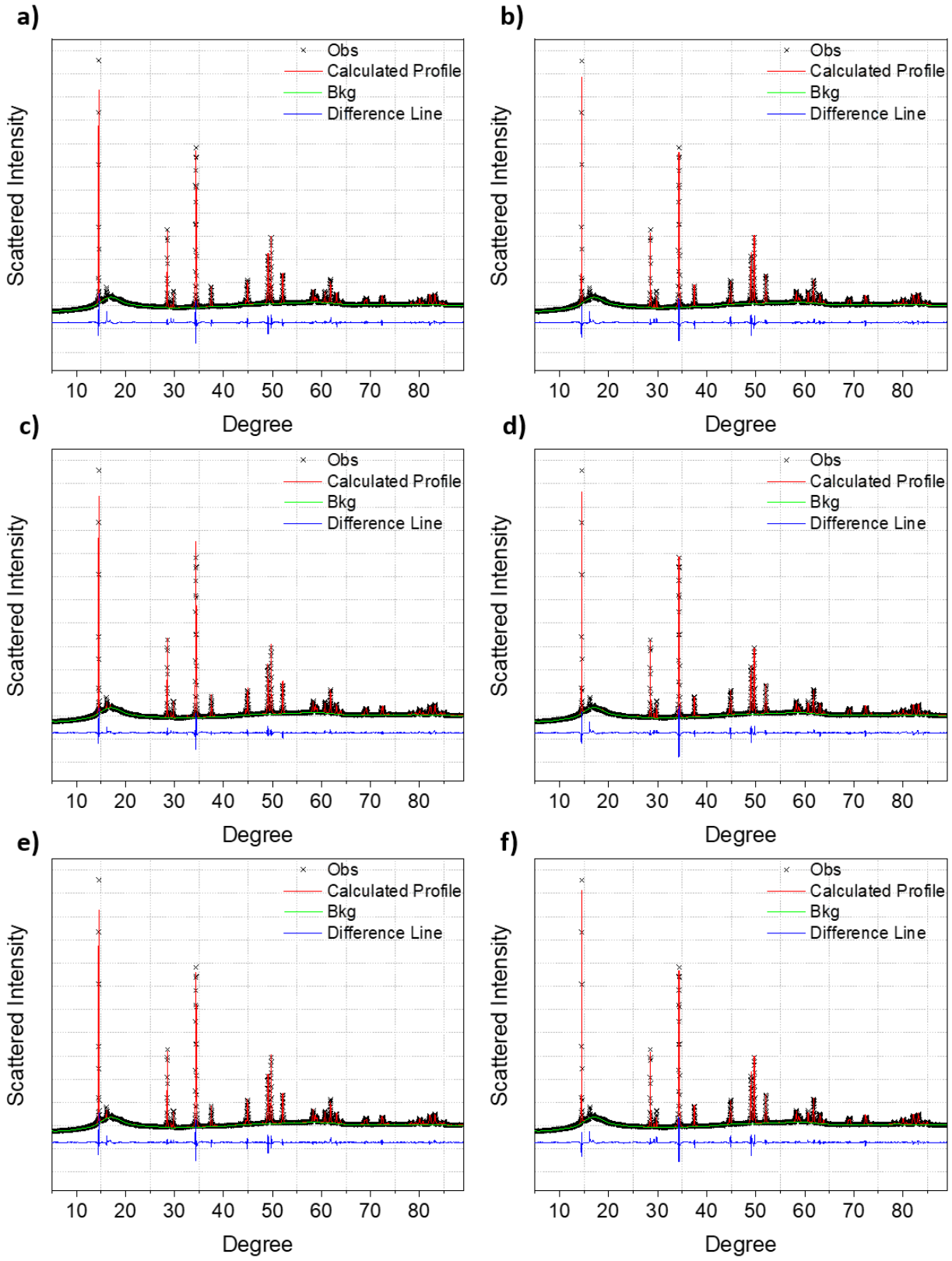

Figure 4.7: Comparison of Rietveld refinements results using a)R_C, b)R_C_3a, c) R_C_3b, d) R_C_3c, e) R_C_3a_3b and f) R_C_3a_b_a+c unit cells.

Table 4.7: Refined atomic positions.

	R_C	R_C_3a	R_C_3b	R_C_3c	R_C_3a_3b	R_C_3a_b_ac
	Atomic position and occupancies (Wycoff position; OF=occupancy fraction)					
Lithium ion layer	(2d) (0 ½ ½) OF(Li)=1	(2d) (0 ½ ½) OF(Li)=1	(2d) (0 ½ ½) OF(Li)=1	(2d) (0 ½ ½) OF(Li)=1	(2d) (0 ½ ½) OF(Li)=1	(2c) (0 0 ½) OF(Li)=1
		(4i) (0.833 0 0.5) OF(Li)=1	(4h) (0 0.825 0.5) OF(Li)=1	(4i) (0.5 0 0.845) OF(Li)=1	(4h) (0 0.823 ½) OF(Li)=1	(4i) (0.667 0 0.5) OF(Li)=1
					(4i) (0.166 0 0.479) OF(Li)=1	
					(8j) (0.833 0.328 0.49) OF(Li)=1	
Metal ions blend layer	(2a) (0 0 0) OF(Li)=0.28 OF(TM)=0.72	(2a) (0 0 0) OF(Li)=0.28 OF(TM)=0.72	(2a) (0 0 0) OF(Li)=0.28 OF(TM)=0.72	(2a) (0 0 0) OF(Li)=0.28 OF(TM)=0.72	(2a) (0 0 0) OF(Li)=0.28 OF(TM)=0.72	(2a) (0 0 0) OF(Li)=0.28 OF(TM)=0.72
		(4i) (0.666 0 -0.006) OF(Li)=0.28 OF(TM)=0.72	(4g) (0 0.669 0) OF(Li)=0.28 OF(TM)=0.72	(4i) (0.004 0 0.668) OF(Li)=0.28 OF(TM)=0.72	(4g) (0 0.66 0) OF(Li)=0.28 OF(TM)=0.72	(4i) (0.67 0 -0.003) OF(Li)=0.28 OF(TM)=0.72
					(4i) (0.331 0 -0.014) OF(Li)=0.28 OF(TM)=0.72	
					(4i) (0.665 0.337 0.007) OF(Li)=0.28 OF(TM)=0.72	
Oxygen ions layers	(4i) (0.248 0 0.719) OF(O)=1	(4i) (0.914 0 0.266) OF(O)=1	(4i) (0.708 0 0.217) OF(O)=1	(4i) (0.752 0 0.747) OF(O)=1	(4i) (0.085 0 0.739) OF(O)=1	(4i) (0.826 0 0.266) OF(O)=1
		(4i) (0.585 0 0.256) OF(O)=1	(8j) (0.244 0.319 0.726) OF(O)=1	(4i) (0.746 0 0.43) OF(O)=1	(8j) (0.919 0.37 0.294) OF(O)=1	(4i) (0.504 0 0.232) OF(O)=1
		(4i) (0.248 0 0.266) OF(O)=1		(4i) (0.734 0 0.08) OF(O)=1	(4i) (0.419 0 0.773) OF(O)=1	(4i) (0.156 0 0.277) OF(O)=1
					(8j) (0.583 0.339 0.307) OF(O)=1	
					(4i) (0.754 0 0.768) OF(O)=1	
					(8j) (0.251 0.345 0.282) OF(O)=1	

4.4.2 Neutron Diffraction

In order to evaluate further the R_C_3b structural model and to validate it as a reasonable alternative to R-3m and C2/m unit cells, a neutron diffraction (ND) patter has been acquired and the diffractogram has been refined with these three unit cells. The collected pattern is shown in figure 4.8, the asterisks indicate the Bragg positions due to the vanadium can[37]. In general, the reflections from the Li−TM ordering are diffuse and weak in neutron data[38], allowing us to compare the different unit cells.

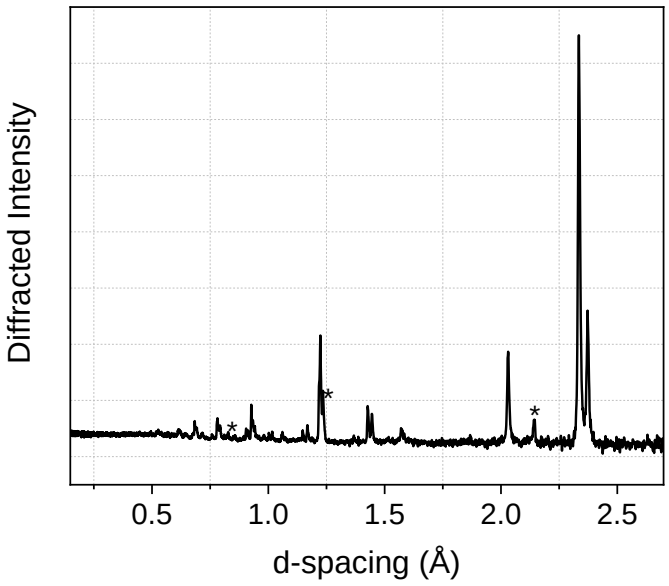

Figure 4.8: Neutron Diffraction data of S10.

The refinements of experimental ND pattern are shown in figure 4.9. The wR values are 2.58, 2.59 and 2.52%, respectively for R-3m, C2/m and R_C_3b unit cells. It is worth to note that we obtained almost the same value with all structural models. Only a slightly improvement can be observed in the case of R_C_3b cell.

Therefore, the neutron analysis confirms that the new structural model, identified from the synchrotron diffraction analysis, is able to successfully fit the collected pattern.

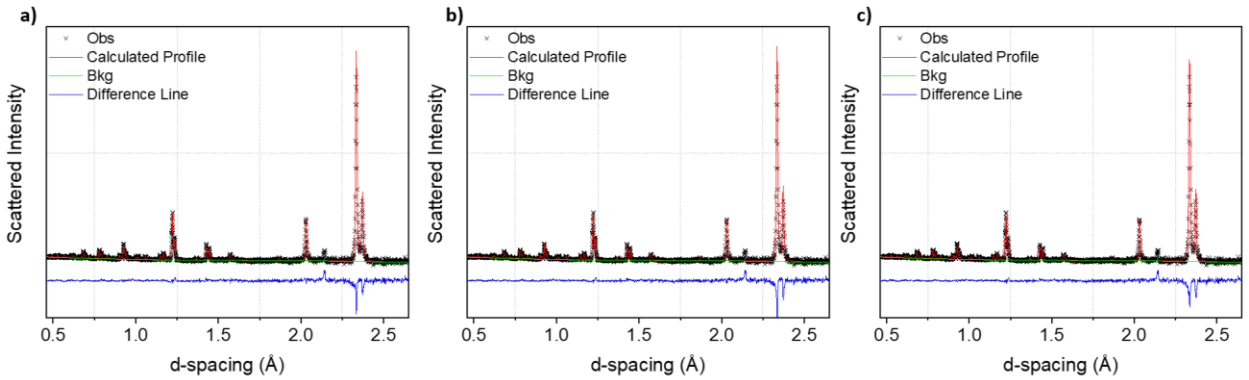

Figure 4.9: Rietveld refinements of Neutron Diffraction data of S10 with a) R-3m, b) C2/m and c) R_C_3b unit cell.

4.4.3 Validation of structural model with different LRLOs materials

The structural model R_C_3b is able to describe the XRD and ND patterns of S10. To check the general validity of the R_C_3b model, two further synchrotron diffractograms of samples $Li_{1.2}Mn_{0.54}Ni_{0.13}Co_{0.13}O_2$ (S01) and $Li_{1.25}Mn_{0.625}Ni_{0.125}O_2$ (S12) have been acquired and refined with the same supercell.

The refinement results are shown in figure 4.10 and the wR values are 3.42 and 5%, respectively for S01 and S12. The same diffractograms converge to wR of 4.6% and 6.5% for the R-3m model, and 6% and 7.6% for the C2/m model, for S01 and S12, respectively.

The low wR parameters suggest that the structural model is also able to model LRLOs with very different stoichiometry.

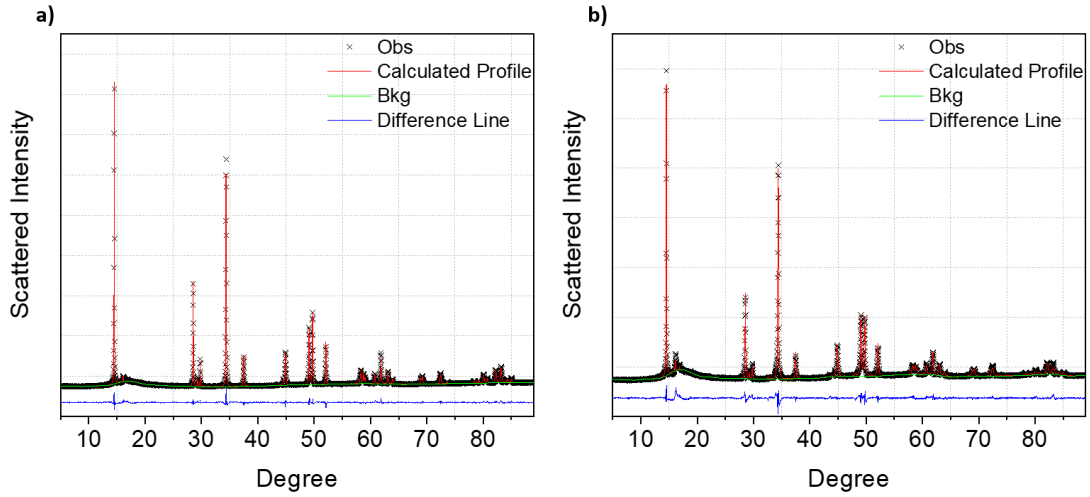

Figure 4.10 a) S01 and b) S12 Synchrotron XRD Refinements with R_C_3b unit cell.

4.5 DESCRIPTION OF STACKING FAULTS: FAULTS APPROACH

It is well known that Lithium-rich materials exhibit a large amount of stacking faults[25,26,34,39], so DIFFaX simulations of several stacking degrees into the sample have been performed to evaluate their impact on the XRD pattern. DIFFaX software requests the construction of several layers stacked on each other differently. A methodological description is reported in section 4.2.

As showed in figure 4.11 stacking faults affect both the peak amplitude and shape, especially in the range of the superstructure peaks. The amplitudes of the (110), (11-1), (021), and (111) reflections, showed in figure 4.11b, significantly reduce and broaden when the degree of stacking faults reaches a faulting value of 20%. These peaks completely disappear increasing the stacking faults. The amplitude of the 020 reflection at around 16.1° remains visible throughout the simulation but exhibits significant asymmetric broadening.

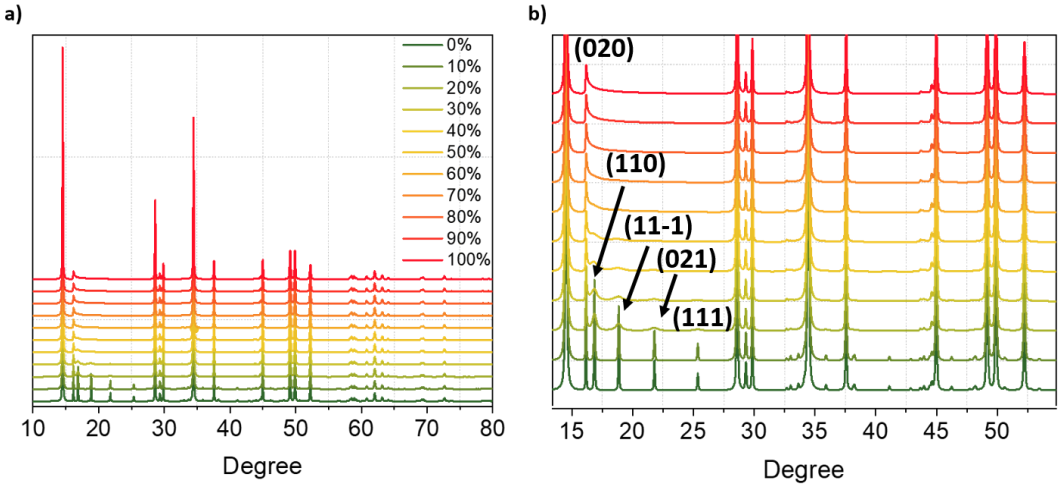

Figure 4.11: a) DIFFaX simulated XRD patterns with varying stacking fault probabilities. b) Enlarged view in the superstructure region.

At the same time, the increase in stacking fault probability does not have any effect on the other Bragg peaks. To quantify the stacking fault probability in the sample, XRD pattern has been fitted with FAULTS software. Similarly to the approach used with DIFFaX, also in this case we need to create a stack of atomic layers connected by stacking vectors associated to stacking probabilities. In fact, the FAULTS software allows to refine the stacking probabilities as well as the lattice parameters, atomic position and so on.

The first step was to refine the collected pattern without any defects in the structure, and the refinement is reported in figure 4.12. From the figure, it can be noted a calculated pattern very similar to the monoclinic pattern reported in figure 4.5b. The calculated intensities and the shapes of superstructure peaks are not able to represent the collected one, in according to what we saw in the simulations of DIFFaX.

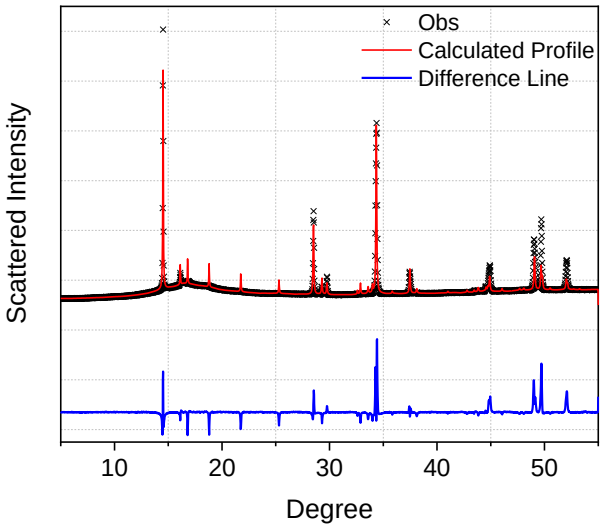

Figure 4.12: a) FAULTS refinement pattern without stacking faults. R-factor=8.4%.

Then, we introduced in the FAULTS refinement of the sample, the presence of stacking faults into the material, as showed in figure 4.13. The refined parameters are shown in table 4.8.

It is expected that the ordering between Li and TM metals in the TM layers is also perturbed by the presence of Ni, Co and Al compared to Li_2MnO_3, which in turn can increase the probability of the stacking disorder along the c axis. Indeed, the refinement reveals a degree of faulting approximately of 45% and R-Factor value of 6.6%. From figure 4.13b, it is evident how this approach successfully fit the superstructure region.

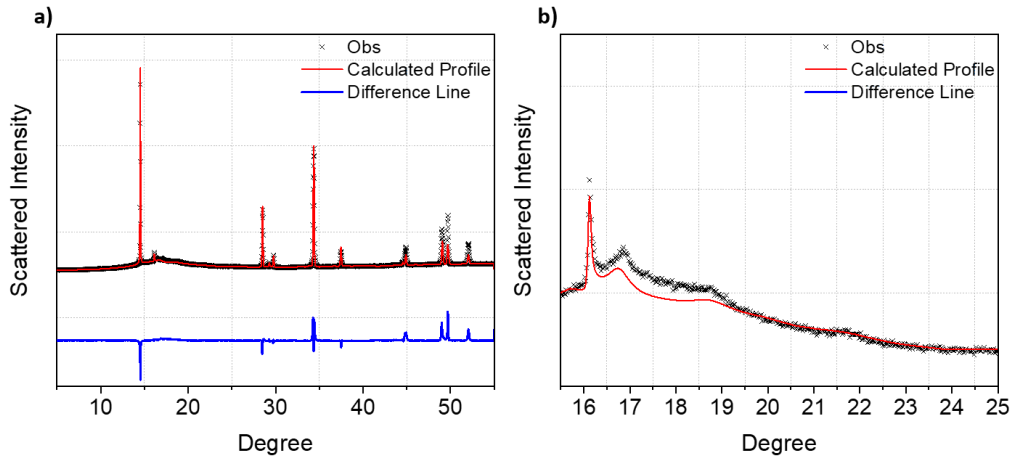

Figure 4.13: a) FAULTS refinement pattern. Magnified view of the refined data in the 15−25° 2θ range.

Table 4.8: Values from the FAULTS refinement.

Unit cell parameters					
a, b (Å)		**c (Å)**		**γ (°)**	
4.939		4.743		60.09	
Layer compositions					
Layer	Atom	x/a	y/b	z/c	Occupancy
L1	Li	0	0	0	1
	Li	1/3	1/3	0	1
	Li	2/3	2/3	0	1
L2=L3=L4	Li	0	0	0	0.84
	TM	0	0	0	0.16
	TM	0.334	0.334	0	1
	TM	0.663	0.663	0	1
	O	0.354	-0.0089	0.249	1
	O	0.643	0.0063	-0.246	1
	O	-0.0092	0.354	-0.246	1
	O	0.337	0.660	-0.225	1
	O	0.660	0.337	0.242	1
	O	0.0064	0.644	0.248	1

In the fitting reported in the table 4.8, we considered stacking defects along the c axis but we omitted to mimic defects in the plane a-b. From the preliminary analysis reported in section 4.3, Li-TM site mixing in the TM layers has proved to lead to a better representation of the structure. Figure 4.14 and table 4.9 show the results also considering Li-TM site mixing. The new occupancies of Li and TM are showed in table 4.9. As a result of the site mixing, the degree of stacking faults changes from 45% to 40%. The R-Factor decreases to 6.2%, indicating an improvement in the refinement and, from figure 4.14b, it is clear that the improvement concerns the superstructure region.

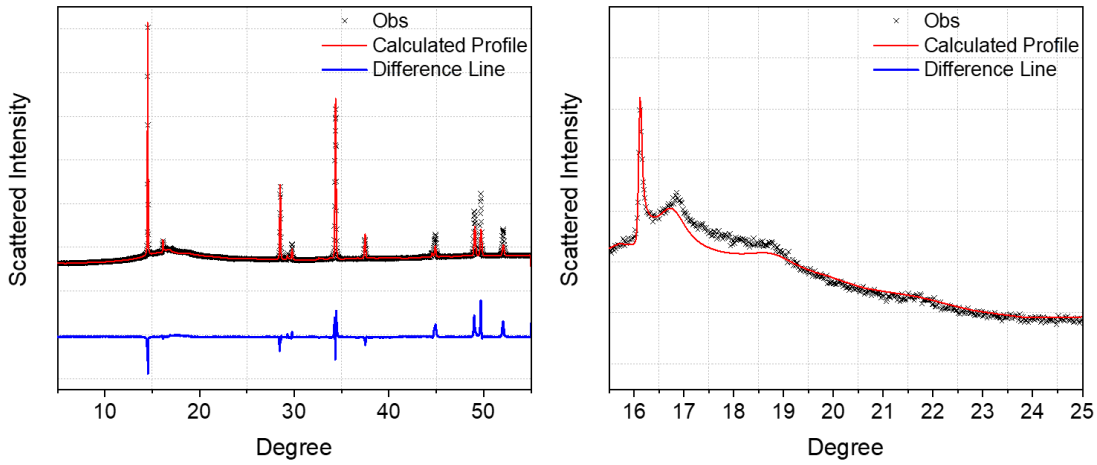

Figure 4.14: a) FAULTS refinement pattern with Li-TM site mixing. Magnified view of the refined data in the 15−25° 2θ range.

Nevertheless, the overall refinement is in line with the previous one. In particular, the refinement fails to model accurately the XRD at high angles, as evident from figure 4.14a. Probably, this can be the consequence of the presence in the sample of crystallites with different degrees of faulting. Therefore, the presence of stacking faults is another good piece of the puzzle but is unable to solve the structure without conserving other parallel phenomena.

Table 4.9: Values from the FAULTS refinement with Li-TM site mixing. The new occupancies are reported in red.

Unit cell parameters					
a, b (Å)		**c (Å)**		**γ (°)**	
4.939		4.743		60.09	
Layer compositions					
Layer	Atom	x/a	y/b	z/c	Occupancy
L1	Li	0	0	0	1
	Li	1/3	1/3	0	1
	Li	2/3	2/3	0	1
L2=L3=L4	Li	0	0	0	0.73
	TM	0	0	0	0.27
	TM	0.337	0.337	0	0.94
	Li	0.337	0.337	0	0.06
	TM	0.662	0.662	0	0.94
	Li	0.662	0.662	0	0.06
	O	0.355	-0.0055	0.252	1
	O	0.644	0.0023	-0.251	1
	O	-0.0021	0.360	-0.252	1
	O	0.331	0.667	-0.244	1
	O	0.668	0.330	0.245	1
	O	0.020	0.636	0.253	1

4.6 CONCLUSIONS

In this chapter, we demonstrated that the conventional unit cells, *i.e.* R-3m and C2/m, cannot represent the overall crystal structure of LRLOs.

When used to refine the synchrotron diffraction pattern of $Li_{1.28}Mn_{0.54}Ni_{0.13}Co_{0.02}Al_{0.03}O_2$, R-3m is not able to fit the superstructure peaks between 16°-25°, while the refinement with C2/m lead

to a poor convergence, mainly due to the wrong calculated intensities and shapes in the superstructure.

For this reason, we tried to introduce defects within the above structures to improve the fitting. Anti-site defects and Li-TM mixing in TM layers have been added in R-3m and C2/m, respectively. Although we got a good improvement with Li-TM mixing, the calculated pattern is still not able to describe all features of the acquired one.

Other two approaches have been used to further improve the description of the pristine structure of over-lithiated Al doped material: 1) supercells and 2) introduction of stacking faults.

The approach of supercells explored the idea that there is some periodicity along one or more lattice directions. Therefore, we have been downgraded the symmetry to the primitive monoclinic unit cell and built the supercells. The cell named R_C_3b showed the best results; it is able to refine both XRD and ND patterns. The comparison between the R_C_3b and the conventional cells exhibited an improvement in the convergence parameters. Moreover, the applicability of this supercell has been tested also on the synchrotron diffraction patterns of other Lithium-Rich material, $Li_{1.2}Mn_{0.54}Ni_{0.13}Co_{0.13}O_2$ and $Li_{1.25}Mn_{0.625}Ni_{0.125}O_2$, with very good results.

The second approach of stacking defects has been investigated due to the experimental evidence of defects in these types of materials. First of all, we simulated the changes of the pattern when the stacking faults increase, using a monoclinic unit cell, in which the stacking faults have been added using different stacking vectors. The superstructure peaks change in intensity and shapes, unlike the other peaks, with the increase of stacking faults.

Then, the pattern has been refined by FAULTS software in order to quantify the staking degree, obtained a value around 45%. Finally, we introduced the Li-TM mixing in the TM layers. Indeed, the classical monoclinic cell has already shown a better convergence after the use of this kind of defects. As a consequence, we obtained a further improvement of the calculated pattern.

In conclusion, we proved that, to describe the complexity of the structure of LRLOs, multiple structural models must be taken into account. The analysis reported here can be considered a further step for the comprehension of the crystal structure of LRLOs materials.

REFERENCES

1. Wang, J. *et al.* Lithium- and Manganese-Rich Oxide Cathode Materials for High-Energy Lithium Ion Batteries. *Adv. Energy Mater.* **6**, (2016).
2. Erickson, E. M. *et al.* Review—Recent Advances and Remaining Challenges for Lithium Ion Battery Cathodes. *J. Electrochem. Soc.* **164**, A6341–A6348 (2017).
3. Thackeray, M. M., Kang, S. H., Johnson, C. S., Vaughey, J. T. & Hackney, S. A. Comments on the structural complexity of lithium-rich $Li_{1+x}M_{1-x}O_2$ electrodes (M = Mn, Ni, Co) for lithium batteries. *Electrochem. commun.* **8**, 1531–1538 (2006).
4. Thackeray, M. M., Johnson, C. S., Vaughey, J. T., Li, N. & Hackney, S. A. Advances in manganese-oxide 'composite' electrodes for lithium-ion batteries. *J. Mater. Chem.* **15**, 2257–2267 (2005).
5. Genevois, C. *et al.* Insight into the atomic structure of cycled lithium-rich layered oxide $Li_{1.20}Mn_{0.54}Co_{0.13}Ni_{0.13}O_2$ using HAADF STEM and electron nanodiffraction. *J. Phys. Chem. C* **119**, 75–83 (2015).
6. Jarvis, K. A., Deng, Z., Allard, L. F., Manthiram, A. & Ferreira, P. J. Atomic structure of a lithium-rich layered oxide material for lithium-ion batteries: Evidence of a solid solution. *Chem. Mater.* **23**, 3614–3621 (2011).
7. Obrovac, M. N., Mao, O. & Dahn, J. R. Structure and electrochemistry of $LiMO_2$ (M=Ti, Mn, Fe, Co, Ni) prepared by mechanochemical synthesis. *Solid State Ionics* **112**, (1998).
8. Montoro, L. A., Abbate, M., Almeida, E. C. & Rosolen, J. M. Electronic structure of the transition metal ions in $LiCoO_2$, $LiNiO_2$ and $LiCo_{0.5}Ni_{0.5}O_2$. *Chem. Phys. Lett.* **309**, (1999).
9. Rozier, P. & Tarascon, J. M. Review—Li-Rich Layered Oxide Cathodes for Next-Generation Li-Ion Batteries: Chances and Challenges. *J. Electrochem. Soc.* **162**, A2490–A2499 (2015).
10. Schipper, F. *et al.* Review—Recent Advances and Remaining Challenges for Lithium Ion Battery Cathodes. *J. Electrochem. Soc.* **164**, A6220–A6228 (2017).
11. Martha, S. K. *et al.* A comparative study of electrodes comprising nanometric and submicron particles of $LiNi_{0.50}Mn_{0.50}O_2$, $LiNi_{0.33}Mn_{0.33}Co_{0.33}O_2$, and $LiNi_{0.40}Mn_{0.40}Co_{0.20}O_2$ layered compounds. *J. Power Sources* **189**, 248–255 (2009).
12. Ruther, R. E. *et al.* Correlating Local Structure with Electrochemical Activity in Li_2MnO_3.

J. Phys. Chem. C **119**, 18022–18029 (2015).

13. Massarotti, V., Bini, M., Capsoni, D., Altomare, M. & Moliterni, A. M. G. G. Ab Initio Structure Determination of Li_2MnO_3 from X-ray Powder Diffraction Data. *J. Appl. Cryst* **30**, (1997).
14. Xiao, R., Li, H. & Chen, L. Density functional investigation on Li_2MnO_3. *Chem. Mater.* **24**, 4242–4251 (2012).
15. Rossouw, M. & Thackeray, M. Lithium manganese oxides from Li_2MnO_3 for rechargeable lithium battery applications. *Mater. Res. Bull.* **26**, 463–473 (1991).
16. Boulineau, A., Croguennec, L., Delmas, C. & Weill, F. Reinvestigation of Li_2MnO_3 structure: Electron diffraction and high resolution TEM. *Chem. Mater.* **21**, 4216–4222 (2009).
17. Robertson, A. D. & Bruce, P. G. Mechanism of electrochemical activity in Li_2MnO_3. *Chem. Mater.* **15**, 1984–1992 (2003).
18. Ji, X. *et al.* A review on progress of lithium-rich manganese-based cathodes for lithium ion batteries. *Journal of Power Sources* **487**, (2021).
19. Zhao, S., Yan, K., Zhang, J., Sun, B. & Wang, G. Reaction Mechanisms of Layered Lithium-Rich Cathode Materials for High-Energy Lithium-Ion Batteries. *Angewandte Chemie - International Edition* **60**, 2208–2220 (2021).
20. Zuo, W. *et al.* Li-rich cathodes for rechargeable Li-based batteries: Reaction mechanisms and advanced characterization techniques. *Energy and Environmental Science* **13**, 4450–4497 (2020).
21. Arunkumar, T. A., Wu, Y. & Manthiram, A. Factors influencing the irreversible oxygen loss and reversible capacity in layered $Li[Li_{1/3}Mn_{2/3}]O_2$-$Li[M]O_2$ (M = $Mn_{0.5-y}Ni_{0.5-y}Co_{2y}$ and $Ni_{1-y}CO_y$) solid solutions. *Chem. Mater.* **19**, 3067–3073 (2007).
22. Ma, Q., Peng, F., Li, R., Yin, S. & Dai, C. Effect of calcination temperature on microstructure and electrochemical performance of lithium-rich layered oxide cathode materials. *Mater. Sci. Eng. B Solid-State Mater. Adv. Technol.* **213**, 123–130 (2016).
23. Matsunaga, T. *et al.* Dependence of Structural Defects in Li_2MnO_3 on Synthesis Temperature. *Chem. Mater.* **28**, 4143–4150 (2016).
24. Xia, Y. *et al.* Oxygen deficiency, a key factor in controlling the cycle performance of Mn-spinel cathode for lithium-ion batteries. *J. Power Sources* **166**, 485–491 (2007).

25. Jarvis, K. A., Deng, Z., Allard, L. F., Manthiram, A. & Ferreira, P. J. Understanding structural defects in lithium-rich layered oxide cathodes. *J. Mater. Chem.* **22**, 11550–11555 (2012).
26. Shunmugasundaram, R., Arumugam, R. S. & Dahn, J. R. A Study of Stacking Faults and Superlattice Ordering in Some Li-Rich Layered Transition Metal Oxide Positive Electrode Materials. *J. Electrochem. Soc.* **163**, A1394–A1400 (2016).
27. Rebuffi, L., Plaisier, J. R., Abdellatief, M., Lausi, A. & Scardi, A. P. MCX: A synchrotron radiation beamline for X-ray diffraction line profile analysis. *Zeitschrift fur Anorg. und Allg. Chemie* **640**, 3100–3106 (2014).
28. Smith, R. I. *et al.* The upgraded Polaris powder diffractometer at the ISIS neutron source. *Rev. Sci. Instrum.* **90**, (2019).
29. Toby, B. H. & Von Dreele, R. B. GSAS-II: The genesis of a modern open-source all purpose crystallography software package. *J. Appl. Crystallogr.* **46**, 544–549 (2013).
30. Casas-Cabanas, M., Reynaud, M., Rikarte, J., Horbach, P. & Rodríguez-Carvajal, J. FAULTS: A program for refinement of structures with extended defects. *J. Appl. Crystallogr.* **49**, 2259–2269 (2016).
31. Kraus, W. & Nolze, G. POWDER CELL-a program for the representation and manipulation of crystal structures and calculation of the resulting X-ray powder patterns. *J. Appl. Cryst* **29**, 301–303 (1996).
32. Faults, P. *et al.* A General Recursion Method for Calculating Diffracted Intensities from Crystals Containing A general recursion method for calculating diffracted intensities from crystals containing planar faults. *Proc. R. Soc. London. Ser. A Math. Phys. Sci.* **433**, 499–520 (1991).
33. Bareño, J. *et al.* Local structure of layered oxide electrode materials for lithium-ion batteries. *Adv. Mater.* **22**, 1122–1127 (2010).
34. Serrano-Sevillano, J. *et al.* Enhanced electrochemical performance of Li-rich cathode materials through microstructural control. *Phys. Chem. Chem. Phys.* **20**, 23112–23122 (2018).
35. Pimenta, V. *et al.* Synthesis of Li-Rich NMC: A Comprehensive Study. *Chem. Mater.* **29**, 9923–9936 (2017).
36. Van Bomme, A. & Dahn, J. R. Analysis of the growth mechanism of coprecipitated

spherical and dense nickel, manganese, and cobalt-containing hydroxides in the presence of aqueous ammonia. *Chem. Mater.* **21**, 1500–1503 (2009).

37. Luo, K. *et al.* Charge-compensation in 3d-transition-metal-oxide intercalation cathodes through the generation of localized electron holes on oxygen. *Nat. Chem.* **8**, 684–691 (2016).
38. Mohanty, D. *et al.* Neutron diffraction and magnetic susceptibility studies on a high-voltage $Li_{1.2}Mn_{0.55}Ni_{0.15}Co_{0.10}O_2$ lithium ion battery cathode: Insight into the crystal structure. *Chem. Mater.* **25**, 4064–4070 (2013).
39. Serrano-Sevillano, J., Casas-Cabanas, M. & Saracibar, A. Impact of Stacking Faults and Li Substitution in Li_xMnO_3 ($0 \leq x \leq 2$) Structural Transformations upon Delithiation . *J. Phys. Chem. Lett.* **12**, 7474–7481 (2021).

5 IMPROVEMENT OF LIQUID ELECTROLYTES BY ADDITION OF PYRROLIDINIUM-BASED IONIC LIQUIDS

The focus of the chapter is the study of novel electrolytes based on ionic liquids with extended stability window. We characterized the physical-chemical properties of electrolytes with different ionic liquids and correlated their properties to the Li^+ coordination in liquid phase. Furthermore, the applicability of the electrolyte in lithium half-cell and full cells was demonstrated.

5.1 INTRODUCTION

Among the different components of LIBs, the electrolyte represents a critical one that affect both safety and cell performance[1]. Commercially-available electrolytes consist of a mixture of carbonate-based dipolar aprotic solvents dissolving a lithium salt. Concentrated solutions of lithium hexafluorophosphate ($LiPF_6$) dissolved in a mixture of cyclic carbonates like ethylene carbonate (EC) and linear like dimethyl carbonate (DMC) in 1:1 v/v (LP30), are the most commonly used one for commercial LIBs, thanks to the good ionic conductivity, chemical inertness, wide electrochemical stability window and the ability to passivate aluminum current collectors[2,3]. However, the $LiPF_6$ salt is thermally unstable, spontaneously decomposes to form LiF and PF_5 species and easily hydrolyze with water traces forming HF[4,5]. Feasible alternatives to replace $LiPF_6$ are lithium imide salts, like LiTFSI (lithium bis-(trifluoromethanesulfonyl)imide)[6]. Nevertheless, despite LiTFSI is less prone to hydrolysis and possess higher thermal and electrochemical stabilities compared to $LiPF_6$[2,7], it is corrosive toward the aluminum current collector, thus hindering its use in a commercial device.

Turning to solvents, alkyl carbonates used as solvents are highly flammable, volatile and toxic[8,9]. Their substitution with low flammable ionic liquids (ILs) have been proved to reduce the risk of thermal runaway and overall hazard of LIBs[10–13]. ILs are low-temperature molten salts, usually formed by a large ammonium quaternary cation and a charge delocalized anion. They have been intensively studied as potential electrolyte solvents in batteries, thanks to their advantageous properties such as the low vapor pressure, thermal stability in a wide temperature range and high ionic conductivity[14–16]. However, after the addition of lithium salt, IL-based electrolytes show high

viscosity resulting in unsatisfactory ionic conductivity and Li^+ transport number[17–21]. To overcome these issues, a common strategy is the addition of an IL to an organic solvents-based electrolytes[22–26]. Several works demonstrated the synergistic effect of the two components leading to lower viscosity, higher conductivity at room temperature as well as improved safety in terms of thermal stability and flammability[12,13,26–28]. The IL organic solvent-based electrolytes result in a good compromise between safety and conductivity and it represent an advantage in terms of costs, compared to the use of pure ILs.

Here, we investigate the physico-chemical properties of six (6) IL-added electrolytes, obtained adding to the 1M $LiPF_6$ in EC:DMC=1:1 v/v and to the 1M LiTFSI in EC:DMC=1:1 v/v, *N*- alkyl-*N*-methyl pyrrolidinium based-IL with different length of alkyl chain. Our goal is to study the influence of the cation size on their physical-chemical and electrochemical properties.

5.2 MATERIALS AND METHODS

ILs are low temperature molten salts, usually formed by a large ammonium quaternary cation and a charge delocalized anion. We have been taken into account three different ionic liquids belonging to the N-alkyl-N-methylpyrrolidinium bis(trifluoromethanesulfonyl) imides ($Pyr_{1,n}$TFSI with n=4,5,8) and used them as co-solvent to two commonly used electrolytes for Li-ion cells: (a) 1M lithium hexafluorophosphate ($LiPF_6$) in a mixture of ethylene carbonate (EC) and linear like dimethyl carbonate (DMC) in 1:1 v/v and (b) 1M lithium bis-(trifluoromethanesulfonyl)imide (LiTFSI) in EC:DMC 1:1 v/v. The chemical formula and structural representations of solvent molecules as well as ILs constituents' anions and cations are shown in Figure 5.1.

Six electrolyte solutions have been prepared by the addition of $Pyr_{1,n}$TFSI with n=4,5,8 in a 1:1 weight ratio to two carbonates-based electrolytes, *i.e.* 1M LiTFSI in EC:DMC=1:1 v/v and 1M LiPF6 in EC:DMC=1:1 v/v. All the electrolyte solutions are summarized in the table 5.1 with the corresponding coding adopted thereafter.

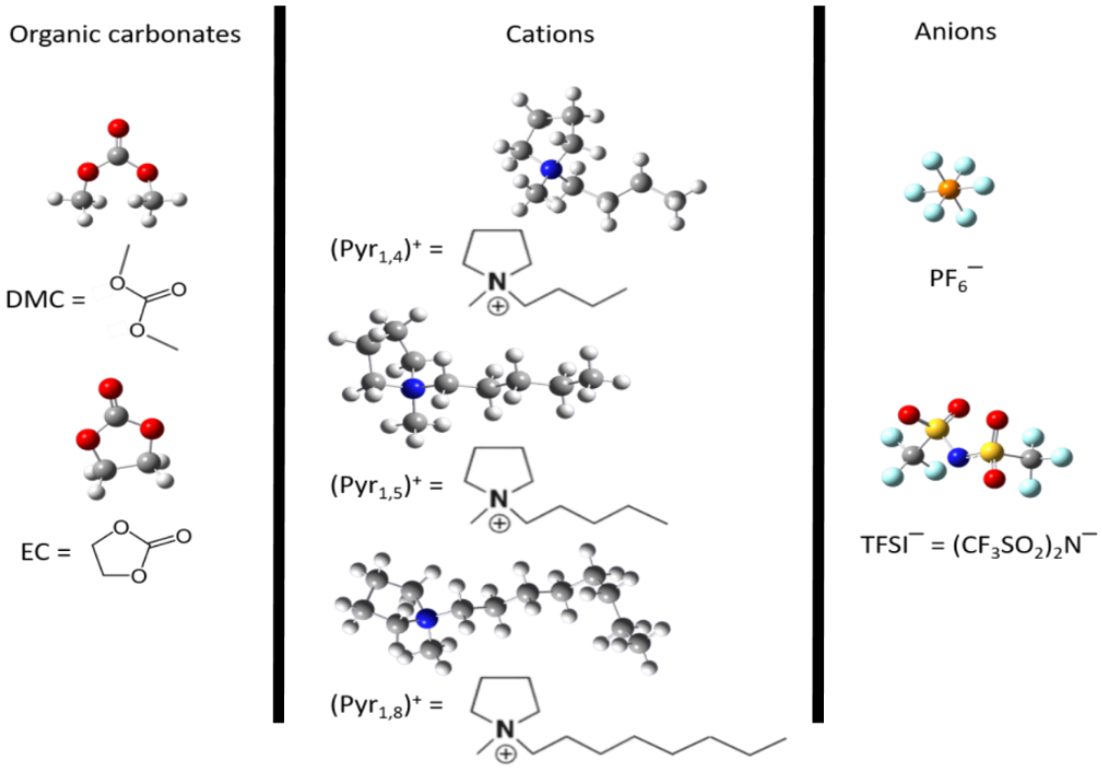

Figure 5.1: Chemical formula and structural representations of solvent molecules and ILs constituents' anions and cations**.**

Table 5.1: Compositions of the electrolyte solutions.

Label	Lithium salt	Solvent	Salt molality	Ionic Liquid	IL wt.%
T	**LiTFSI**	**EC:DMC=1:1 v/v**	**0.98**	**/**	**/**
TA	**LiTFSI**	**EC:DMC=1:1 v/v**	**0.43**	**[Pyr$_{1,4}$]TFSI**	**50**
TB	**LiTFSI**	**EC:DMC=1:1 v/v**	**0.43**	**[Pyr$_{1,5}$]TFSI**	**50**
TC	**LiTFSI**	**EC:DMC=1:1 v/v**	**0.43**	**[Pyr$_{1,8}$]TFSI**	**50**
P	**LiPF$_6$**	**EC:DMC=1:1 v/v**	**0.87**	**/**	**/**
PA	**LiPF$_6$**	**EC:DMC=1:1 v/v**	**0.41**	**[Pyr$_{1,4}$]TFSI**	**50**
PB	**LiPF$_6$**	**EC:DMC=1:1 v/v**	**0.41**	**[Pyr$_{1,5}$]TFSI**	**50**
PC	**LiPF$_6$**	**EC:DMC=1:1 v/v**	**0.41**	**[Pyr$_{1,8}$]TFSI**	**50**

The as obtained six (6) IL-added electrolytes have been studied in terms of ionic conductivities, viscosities, electrochemical stability as well as vibrational properties. Furthermore, the application

of these kind of electrolytes in lithium cell have been performed with a standard cathode material (*i.e.* $LiFePO_4$).

The Flash points of the electrolytes solutions were determined by using a Grabner instrument and according to the measurement protocol D6450. 1ml of sample heated in a closed cup from T(initial) to T(final). To follow the protocol exactly, T(initial) was equal to T(flash) minus 18°C, while the T(final) was kept enough to detect the T(flash) of the solution. The heating rate was 5.5°C/min and the ignition interval of 1 test per °C. The viscosity of the mixed electrolytes was determined by a Lovis 2000 M/ME (Anton Paar) viscosity meter in the temperature range 10°C and 80°C. The temperature was increased in steps of 10°C. The ionic conductivity of the electrolytes solution was determined by dielectric measurements, performed with a Novocontrol GmBH broadband dielectric spectrometer equipped with a Quatro Cryosystem temperature control unit. The measurements were performed in the frequency range of 10^{-1}-10^{7} Hz and temperature range between -10-60°C, respectively. The temperature was increased in steps of 10°C and at each temperature an equilibration time of 30 min was used. The fitting procedure of the temperature dependence of the ionic conductivity has been carried out by assuming either the VTF and the Arrhenius models. The fitting has been performed using a non-linear randomized fitting algorithm programmed on spreadsheet (e.g. Excel): the goal function was the minimum chi-square parameter calculated between experimental and fitted conductivity data.

Room temperature Raman scattering measurements were carried out using a Renishaw inVia micro-Raman spectrometer in backscattering geometry equipped with 785 nm diode laser (power 82 mW) as the excitation light source. The electrolyte was inside a quartz Cuvette and the incident laser was focused by a 5X optical microscope objective with a numerical aperture of 0.14 and then the scattered light was detected in a back-scattering geometry dispersed by 1200 grooves mm^{-1} grating on CCD detector. Acquisition time for a single measurement was 5 sec. Raman spectra were fitted using the Voigt function implemented in the Origin lab. The spectral region between 850-750 cm^{-1} has been deconvoluted into 4 bands, corresponding to the free and coordinated EC and DMC with lithium ions, respectively. In the region between 705-765 cm^{-1}, the spectra have been fitted with 5 Voigt functions that include the free and coordinated EC with Li^{+}, the two conformers (cisoid and transoid) and the coordinated TFSI with Li^{+}. Furthermore, the population ratio of the two conformers has been calculated in the spectral range 250-350 cm^{-1}. According to

Martinelli et al.[7], the integrated intensities of the deconvoluted bands can be used to estimate the [C1]/[C2] ratio, according to the equation (1):

$$r = \frac{[C1]}{[C2]} = \frac{I_{306}+I_{326}+I_{333}}{I_{298}+I_{314}+I_{339}} \quad (1)$$

In the case of P-series electrolytes, we also considered that PF_6^- band at 741 cm^{-1} that overlaps with the TFSI signal. In line with Oldiges et al.[29] we assumed constant the PF_6^- contribution in the composite electrolytes, including in the fitting the pristine peak from LP30 (P electrolyte).

Once obtained the deconvoluted spectra for all the electrolytes, the average coordination number, n, has been calculated by multiplying the ratio of the ligand and Li^+ concentration (indicated as c_{ligand} and c_{Li+}, respectively) with the ratio of integrated peaks area, in according to the equation (2):

$$n = \frac{c_{ligand}}{c_{Li^+}} \frac{A_{coordinated}}{A_{coordinated}+A_{free}} \quad (2)$$

The electrochemical stability window of all the electrolytes were evaluated by LSV for anodic scan and CV for cathodic scan, using SuperP carbon casted on aluminum (cathodic) or copper (anodic) foil as working electrode and a lithium foil as counter electrode. The voltage range used was 0-6 V for LSV and 0.005-2.5 V for CV, while the scan rate was 1 mV/s.

The lithium transference number was determined by potentiostatic-polarization measurements. Following the method proposed by Vincent, Bruce and Evans[30] a small potential of 50 mV has been applied between symmetric lithium/lithium cell for 1 hour or at least potential stabilization. Electrochemical impedance spectroscopy (EIS) has been used to monitor the resistance values before and after polarization. EIS measurements were performed applying a potential of 10 mV in the frequency range 100 kHz-100 mHz. Galvanostatic deposition-stripping tests have been carried out in a symmetric Li/electrolyte/Li cell using a current density of 0.1 $mAcm^2$ with a step duration of 30 minutes.

A Biologic VMP3 multichannel potentiostat was used for all the measurements. All the tests have been carried out in Teflon coated Swagelok cells. A Biologic BCS-805 battery cycler has been used for galvanostatic cycling. Coin cells 2032 were assembled using LiFePO4 (LFP) or Si/graphene as working and lithium foil as counter electrode. A Whatman glass fiber disk soaked with 100 µl of electrolyte was used as separator. For LFP, galvanostatic tests were carried out in a potential range of 2.5-3.8V using a rate of C/10 (1C=170 mAg^{-1}); while for Si-graphene,

galvanostatic tests were performed between 0.01-2V as formation cycle and between 0.1-1V for the other cycles. LiFePO4 electrode sheets with a nominal capacity of 2.3 $mAhcm^{-2}$ were purchased from NEI Corporation. Si-graphene electrodes were prepared following the procedure described in Ref[31].

Finally, for Li-ion, tests were carried out between 2.4-3.6V with a current density of 100 mAg^{-1}. The full cells were balanced considering the nominal capacity of the cathode and the reversible capacity of the anode, obtained from the galvanostatic tests in lithium cells.

5.3 ELECTROLYTES CHARACTERIZATION

5.3.1 Flammability and Electrochemical Stability

The flammability of the electrolytes is a key point for the safety of Lithium-Ion Battery. Here the flammability was studied by the determination of the flash point, showed in figure 5.2. The electrolytes without IL (P and T) are reported for comparison. The experiment has been performed in collaboration with the group of Prof. Alexander Matic at Chalmers University of Technology.

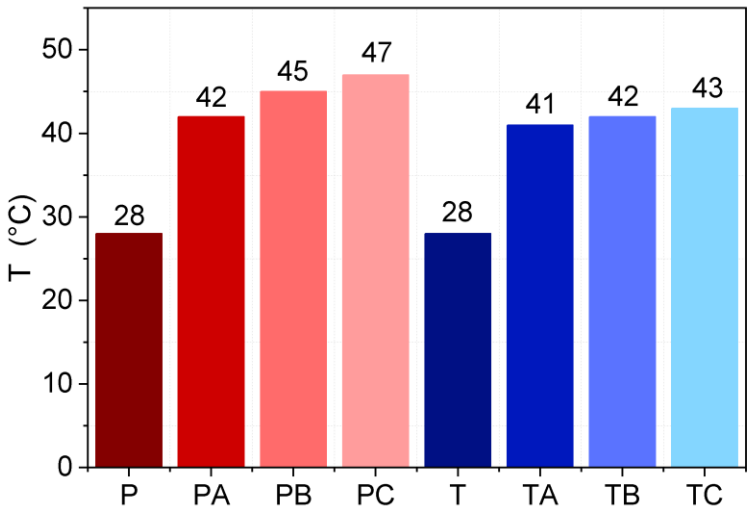

Figure 5.2: Flash points tests for the P and T based electrolytes solutions.

According to "European CLP regulation"[32] the flash point is considered as a determinant parameter to classify the flammable liquids. The pristine P and T electrolytes show a lower flash point, confirming that the addition of ILs mitigated the flammability. All the blended electrolytes show

Table 5.2: Irreversible reaction potentials measured for anodic and cathodic scan.

Label	Anodic scan onset potential (V)	Cathodic irreversible decomposition potentials (V)	
		Onset	Peak edge
P	5.1	0.77	0.37
PA	5.45	0.7	0.35
PB	5.4	0.73	0.49
PC	5.3	0.7	0.45
T	4.9	0.82	0.37
TA	5.4	0.82	0.42
TB	5.2	0.75	0.4
TC	4.6	0.74	0.44

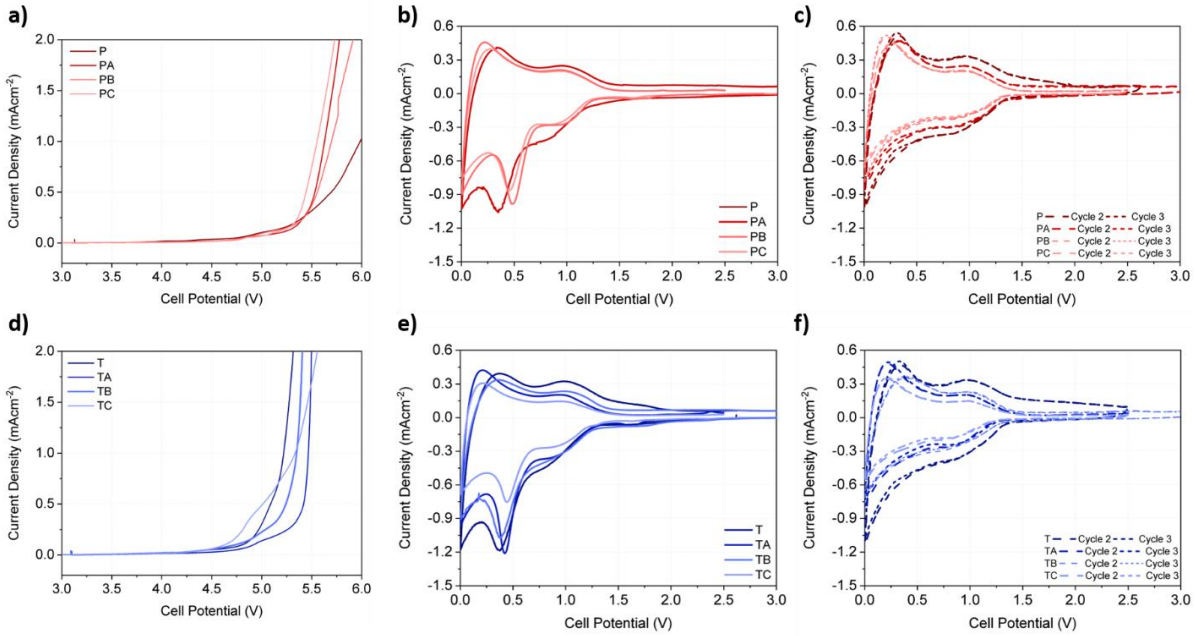

Figure 5.3: Linear Sweep Voltammetry of a) P-series electrolytes and d) T-series electrolytes measured in the voltage range between 3-6V at scan rate of 1 mV s^{-1}. Cyclic Voltammetry of b-c) P-series electrolytes, e-f) T-series electrolytes acquired in the voltage range 0-2.5V at scan rate of 1mV/s.

flash points above 40°C, while the pristine electrolytes are below 30°C. Moreover, the flash point increases with the elongation of alkyl chains.

Electrochemical stability windows of the benchmark and IL-added electrolytes have been evaluated by Linear Sweep Voltammetry (LSV) and Cyclic Voltammetry (CV)[11,12,22,26,33]. Electrochemical stability window represents the voltage range in which the electrolyte should be electrochemically stable. In order to perform these voltammetries, a SuperP Carbon electrode was used, casted on aluminum (anodic scan) or copper (cathodic scan) foil. LSV and CV are shown in figure 5.3 and the calculated anodic/cathodic potentials for the irreversible reactions are summarized in table 5.2. In all the electrolytes, we can observe a small pre decomposition peak above 4.5 V, followed by a current drift above 5 V. All the P-electrolytes exhibit a current drift above 5.2V due to the irreversible degradation of the solvent molecules: however, the addition of IL in the alkyl-carbonates solvent slightly alters anodic stability. In particular, a shift to higher voltages in the onset potential is observed for PA and PB electrolytes, while in the case of PC the onset potential is slightly decrease compared to the P one. As expected, the T electrolyte exhibits a lower anodic stability compared to P electrolyte[34] being the onset potential shifted to lower voltages, but it has the same trend of P series. Turning to the cathodic branch (figure 5.3b), as expected, the P electrolyte shows multiple electro-active processes[8]: (a) a small current drift starting at around 1.3V, followed by other signals with onset potentials at (b) 0.77, (c) 0.54 and (d) ~0.2 V in the first voltammetric cycle. Generally speaking, the addition of ILs shifts the reduction onset potentials downward to lower voltages, thus enlarging the cathodic stability windows. In all P-electrolytes, in the second voltammetry cycle, the peak centered at ~0.5V disappears (figure 5.3c), being originated by the decomposition of the electrolyte components on electrode surface and the formation of an electrochemically stable solid-electrolyte interface (SEI). A very similar behaviour is observed also with T- electrolytes (figure 5.3e-f). In summary the addition of ILs to both P and T electrolytes extends the electrochemical stability window achieving a remarkable 0.75-5.2 V vs. Li and 0.75-5.4 V vs. Li stability ranges for TB and PB, respectively.

5.3.2 Transport Properties

The ionic conductivity and dynamic viscosities were also investigated and the results are shown in figure 5.4. As reported in literature[12,13,25,26,28,35], the ionic conductivity decreases with the addition of ILs, for both two series, as showed in figures 5.4a and 5.4c, with a decreasing trend that follows the size of the alkyl chain being TC<TB<TA<T and PC<PB<PA<P.

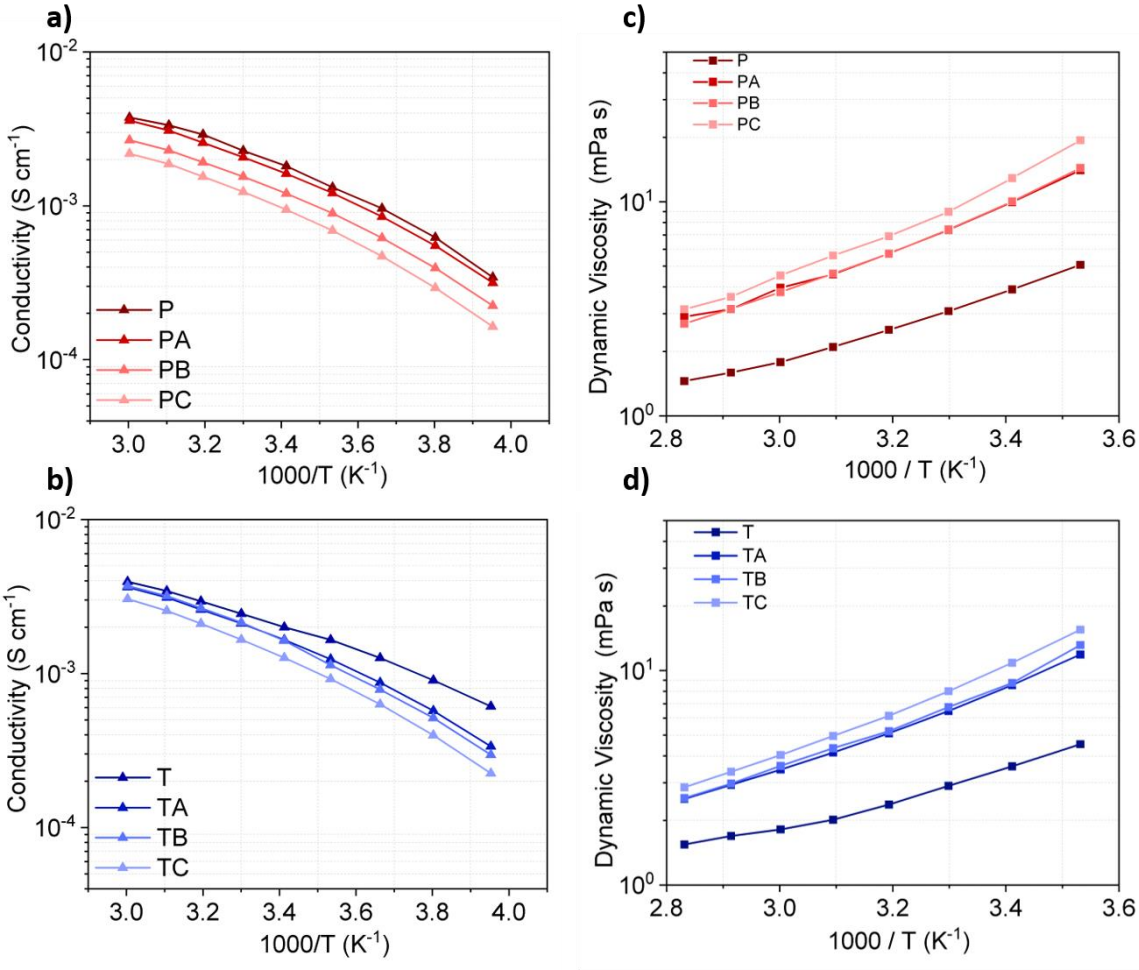

Figure 5.4: Arrhenius plots of the P-series electrolytes (a) and T-series electrolytes (b) and Dynamic viscosity as function of the temperature for the P-series electrolytes (c) and T-series electrolytes (d).

This trend is connected to the viscosity of ILs, because the ionic conductivity, in the mixture of ionic liquids/organic solvent, is affected mostly by the increasing of viscosity. ILs with long alkyl chain are intrinsically more viscous than ILs with short alkyl chain and the dynamic viscosity showed a reverse trend in respect to conductivity as shown in figures 5.4b and 5.4d. Furthermore,

the alteration in both viscosity and conductivity roots in the alteration of the lithium coordination in the solution induced by the addition of ILs (see the following section). The evolution in temperature of the ionic conductivity (σ) of the two series of novel electrolytes is well fitted with the Vogel-Tammann-Fulcher (VTF) equation [Eq.(1)][36,37], commonly used for IL-based liquids:

$$Eq.(1)\quad \sigma = \sigma_0 \cdot exp\{-E_a/[R \cdot (T - T_0)]\}$$

Where the pre-exponential term σ_0 corresponds to the ionic conductivity at infinite temperature, E_a is a pseudo-activation energy for the ion hopping and T_0 is defined as the ideal glass transition temperature below which the ion mobility is zero. Besides the VTF model, also the Arrhenius equation can be used to fit the temperature dependence of the ionic conductivity in liquids[38]. The comparison among the fitting convergence parameters (R^2 and chi-square sums) obtained for the two models for all the eight electrolytes are summarized in the table 5.3.

Table 5.3: Convergence parameters (correlation coefficient R^2 and chi-square sums χ^2) of the three adopted fitting models for the temperature dependence of the conductivities of the six electrolytes.

Electrolyte	**Arrhenius model** $\sigma = A \cdot e^{-E(\frac{a}{RT})}$		**Vogel-Tammann-Fulcher (VTF) model** $\sigma = A \cdot e^{-E(\frac{a}{R(T-T0)})}$	
	R^2	**χ^2**	**R^2**	**χ^2**
P	0.98901	0.01284	0.99965	0.00041
PA	0.99214	0.00941	0.99995	0.00006
PB	0.99153	0.01059	0.99996	0.00005
PC	0.99183	0.01120	0.99994	0.00008
T	0.99540	0.00322	0.99975	0.00017
TA	0.99273	0.00840	0.99998	0.00003
TB	0.99336	0.00884	0.99968	0.00043
TC	0.99360	0.00887	0.99998	0.00003

Overall, the VTF model outperform the fitting by the Arrhenius equation of more than one order of magnitude in convergences for all cases. Therefore, we discarded the fittings by the Arrhenius

model and assumed the VTF one in line with the standard literature. The parameters obtained by the VTF linear fits for the conductivity trends with temperature are shown in table 5.4.

Table 5.4: Conductivity fitting coefficients calculated for the electrolyte solutions under investigation adopting a VTF model equation.

Label	Activation energy [kJ/mol]	Ideal glass transition temperature [Ke]
P	35	**186**
PA	44	**176**
PB	43	**179**
PC	47	**177**
T	47	**157**
TA	45	**174**
TB	54	**168**
TC	**54**	**167**

The pseudo-activation energies increase while adding the ILs to both P and T electrolytes, apart for the TA case. On the other hand, the ideal glass transition temperatures decrease for the IL-added P-electrolytes while increase for the IL-added T-ones. One may speculate that the addition of ionic liquids may lead to a stronger binding energy between solvated ionic couples thus slightly hinders their individual mobility. Less clear is the missing matching between the evolution of the ideal glass transition temperatures and the trend of standard entropies of mixing for the various electrolytes (T: 9.3 $JK^{-1}mol^{-1}$; T: 9.4 $JK^{-1}mol^{-1}$; PA, PB, PC: ~14 $JK^{-1}mol^{-1}$; TA, TB, TC: ~12 $JK^{-1}mol^{-1}$). The increase in the disorder of the liquid solution induced by the increase of the constituent species apparently extend the liquid range only in the case of the PA, PB and PC whereas the VTF fits suggest that TA, TB and TC electrolytes glassify at higher temperatures, from 10 to 15 degrees, compared to the benchmark T-one.

The ionicity of the IL-added electrolytes has been qualitatively checked by Walden rule in line with the majority of the literature approaches (see Eq.(2))[39–41]:

$$Eq.(2) \quad \Lambda\eta = k$$

Where Λ is the molar conductivity, η the viscosity and k is a constant dependent from temperature.

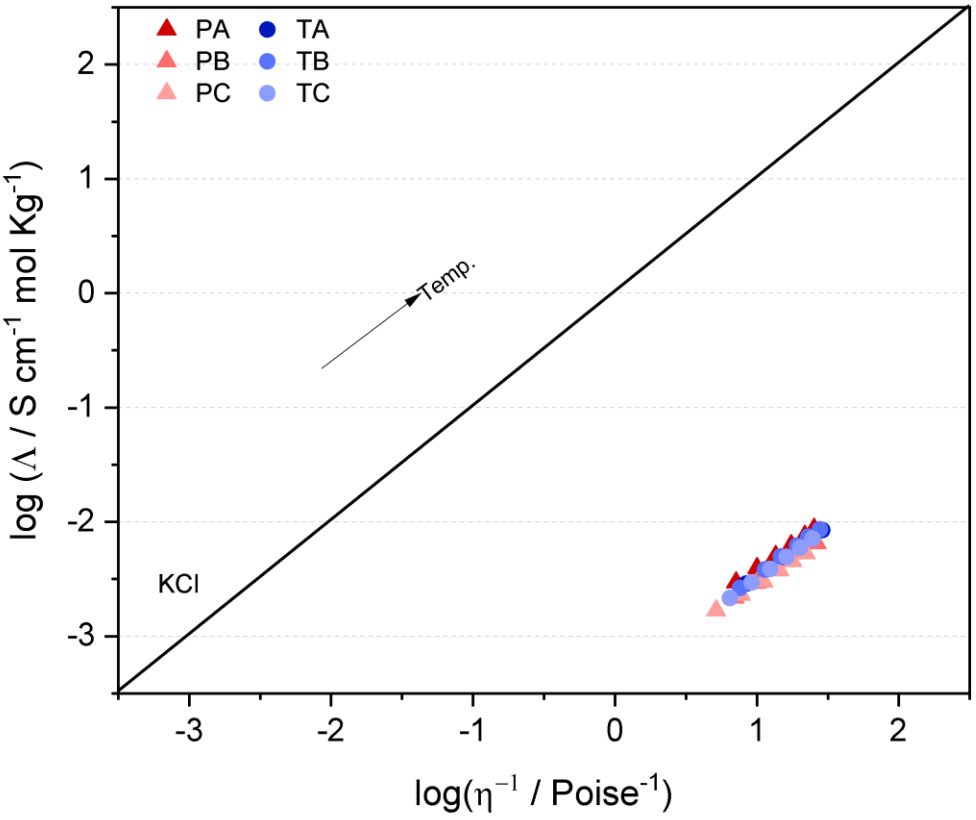

Figure 5.5: Walden plot for the IL-electrolyte mixtures.

The lithium transference numbers calculated in according to the method developed by Vincent, Bruce and Evans[30] are listed in table 5.5. The Nyquist plot before and after polarization obtained for all the electrolytes under investigation and the corresponding polarization curves are shown in figure 5.6 for all the 8 electrolytes. Despite the use of this method is not verified in literature for ternary/quaternary electrolytes, it was used to have a semiquantitative determination of the transport number being all currents originated by the motion of all charged species in the electrolyte: thus, the larger the complexity of the solution the larger the occurrence of unexpected transport phenomena. Values of 0.32 and 0.36 have been obtained for carbonate-based electrolytes P and T, respectively, in line with the literature values.

Table 5.5: Li transference number calculated for the electrolyte solution.

Label	Li transference number
P	0.32
PA	0.18
PB	0.23
PC	0.23
T	0.36
TA	0.08
TB	0.13
TC	0.06

Overall in both the ILs-added P-and T-electrolytes the transport numbers are smaller due to smaller concentration of the salt (see table 5.1). However, values for the P-series systematically overcome those of the corresponding T-electrolytes although the Li^+ concentration are comparable. In fact, in parallel with the reduction of the Li^+ content of 50% in both cases due to dilution, the lithium transport number decreases of about 33% in the P-series whereas it drops of approximately 76% for the T-electrolytes. Such asymmetric variations may be the clue of a more structured coordination environment in the T-electrolytes around the Li^+ cations.

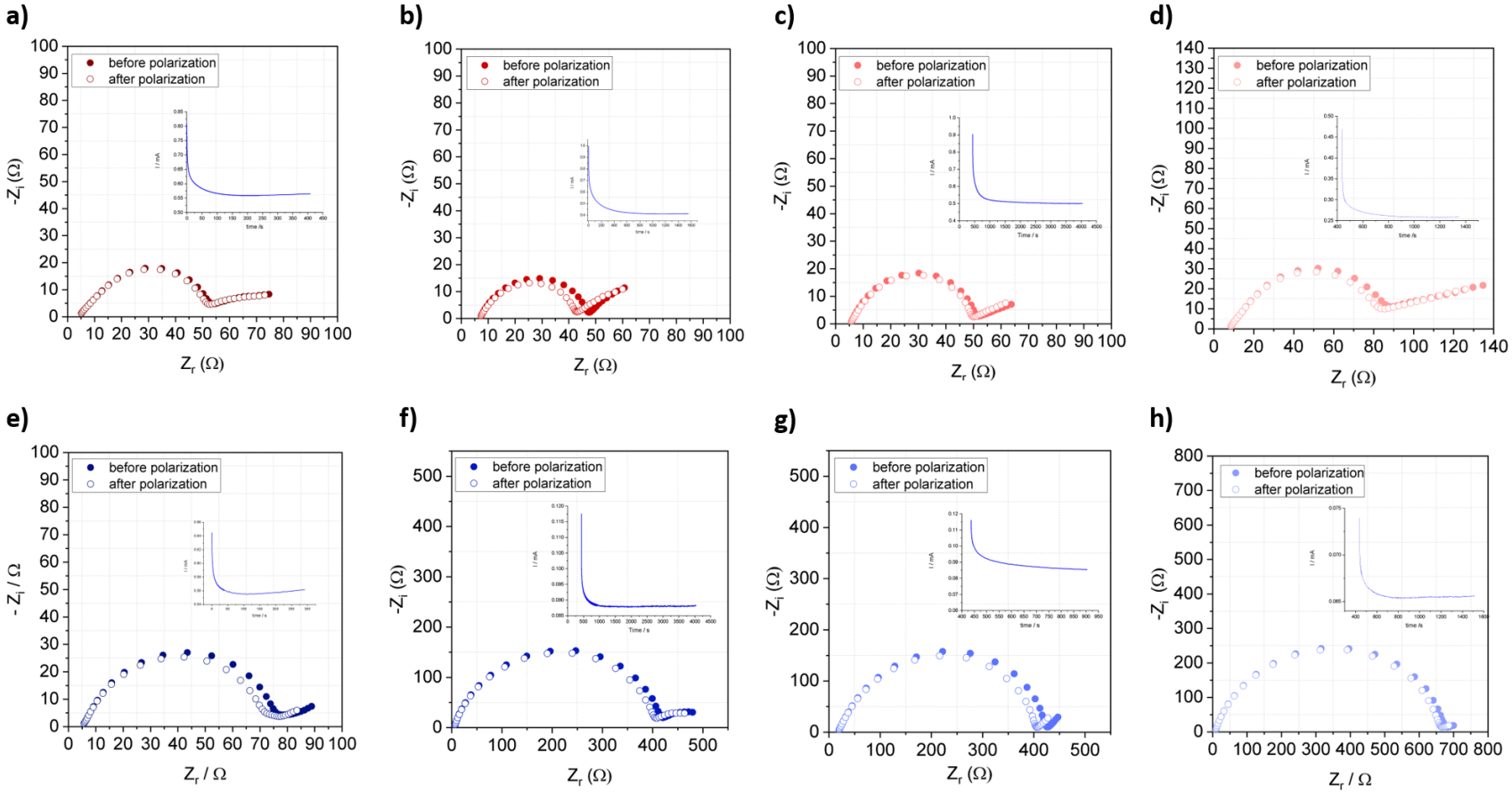

Figure 5.6: Potentiostatic-polarization measurements of a) P, b) PA, c) PB, d) PC, e) T, f) TA, g) TB, and h) TC

5.3.3 Raman Spectroscopy

Raman spectroscopy has been used to investigate the interaction of lithium with TFSI anion of ionic liquid. Preliminary analysis has been made on pure ionic liquids, in order to identify any changes due to the different alkyl chains. Figure 5.7 shows the Raman spectra acquired in 3 different spectral regions: 2700-3200 cm^{-1}, 725-755 cm^{-1} and 200-450 cm^{-1}. In the region between 2700-3200 cm^{-1} (Figure 5.7a) it is possible to detect the C-H vibrational modes derived from cation.

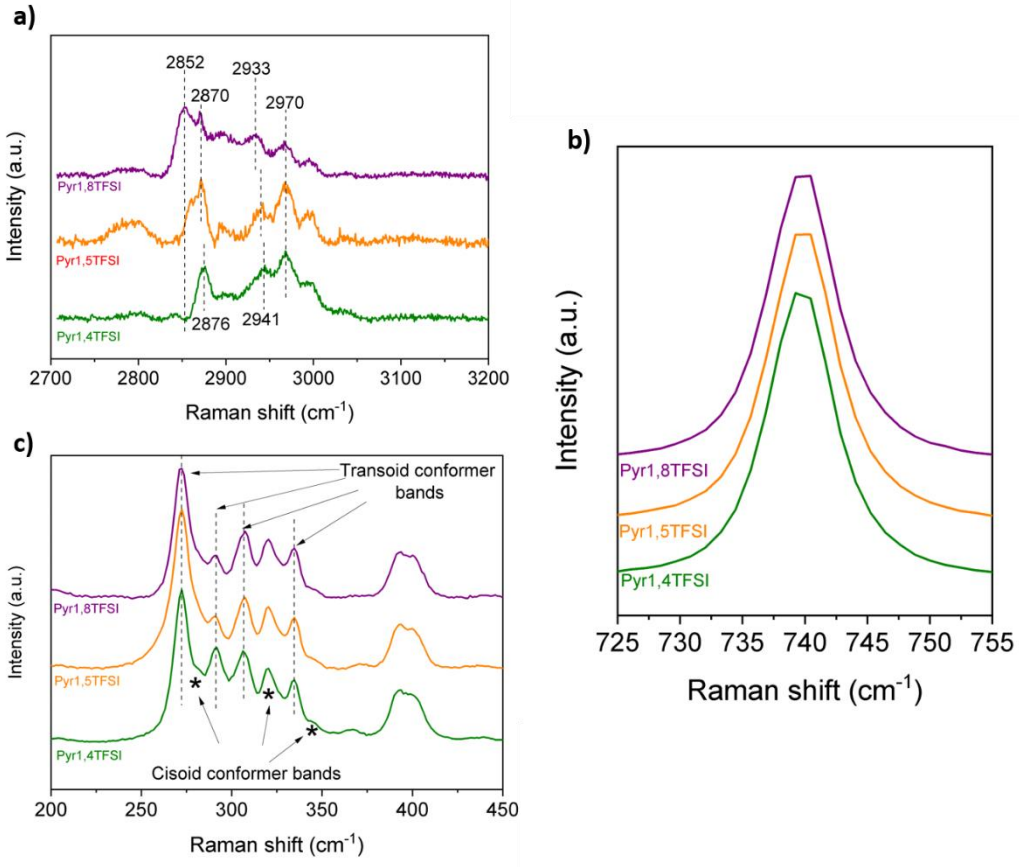

Figure 5.7: Raman spectra of the pure ionic liquids in the range a) 2700-3200 cm^{-1}, b) 725-755 cm^{-1} and c) 200-450 cm^{-1}.

As consequence of the increasing of alkyl chain, the peak at 2970 cm^{-1} exhibits modifications in the intensity of the vibrational modes, being this band associated to the modes of the alkyl chain[42]. Further differences can be observed at 2852 cm^{-1} where $Pyr_{1,8}TFSI$ exhibit a strong peak. The modes at 2876 and 2941 cm^{-1} in $Pyr_{1,4}TFSI$ are shifted to lower wave numbers in $Pyr_{1,8}TFSI$, respectively to 2870 and 2933 cm^{-1}. These bands are associated to the vibrational mode of CH_2 in

ring. The shifts observed is indirectly correlated to the length of alkyl chain; but they depend more from the different position of TFSI anion respect to the pyrrolidinic ring when the alkyl chain of cation increase. Furthermore, other bands with weak relative intensity can be detected at 3000 and 3031 cm^{-1} and related to the anti-symmetric stretching mode of C-H in $C\text{-}CH_3$ and $N^+\text{-}CH_3$, respectively.

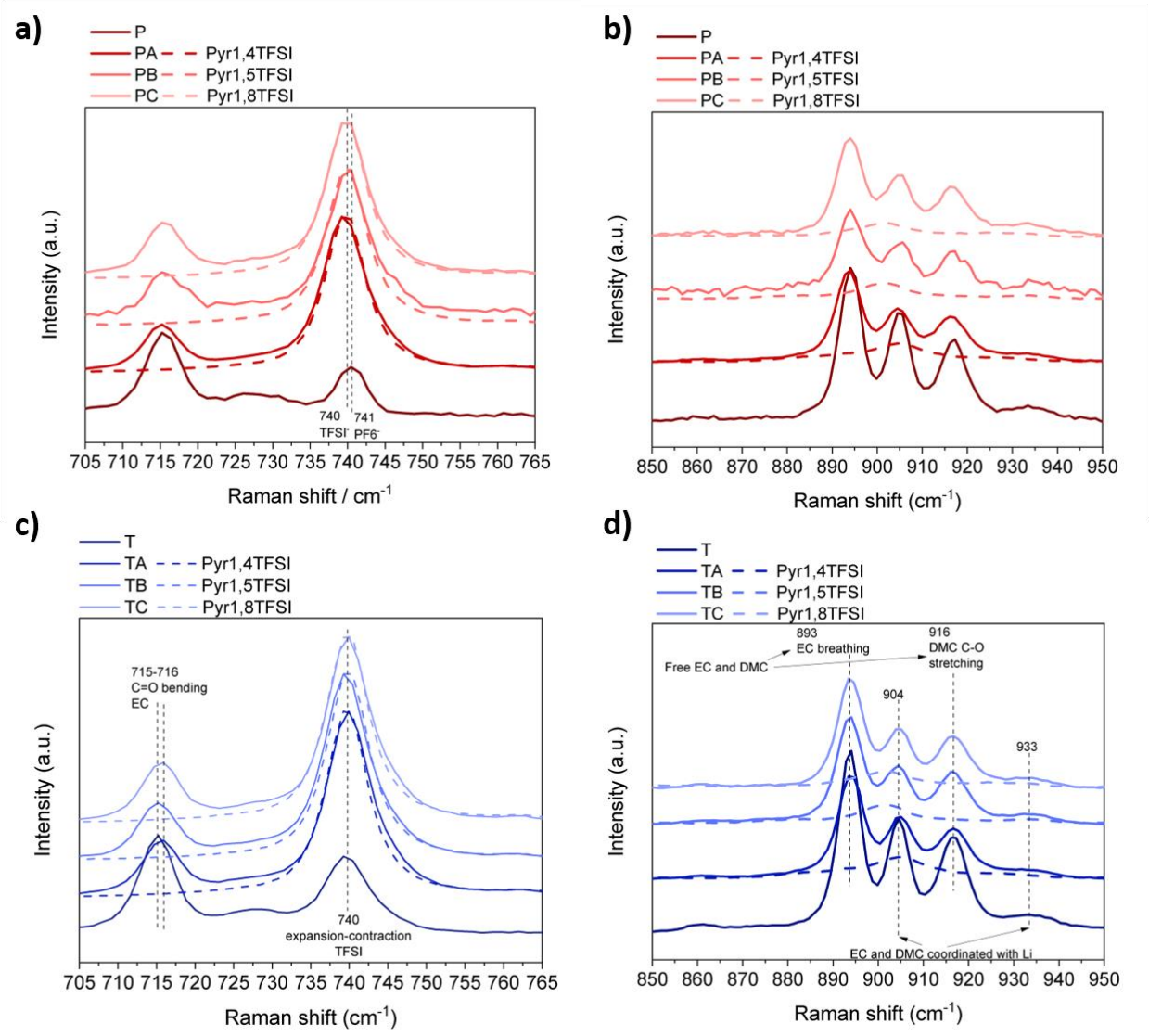

Figure 5.8: Raman spectra of the P-series electrolytes (a,b) and T-series electrolytes (c,d). Dotted lines correspond to the spectra acquired for the pure ionic liquids.

The other two regions showed in figures 5.7b and 5.7c, are related to the vibrational mode of TFSI anion[43,44]. The 3 ionic liquids exhibit a strong peak at 740 cm^{-1} corresponding to the expansion-contraction modes of the whole anion. As expected, negligible differences are detected in the three

samples. Finally, the bands in the region 250-350 cm^{-1} showed in figure 5.7c can be assigned to the twisting and rocking modes of SO_2 and CF_3 groups in the TFSI anion and are sensitive to the two stable conformers (cisoid and transoid).

In figure 5.8 magnifications of the Raman spectra for all the electrolytes are shown in the ranges 850-950 cm^{-1} and 705-765 cm^{-1}. These spectral regions are typically used to investigate the coordination of Li^+ with TFSI anion and with the organic solvents[44–46], respectively. The region between 850-950 cm^{-1}, showed in Figures 5.8b and 5.8d, exhibits a series of bands assigned to the vibrational modes of carbonate molecules.

According to literature, the peaks at 893 and 916 cm^{-1} correspond to the EC breathing and C-O stretching of DMC for the free solvents, respectively. These bands are shifted respectively at 904 and 933 cm^{-1} when solvent molecules coordinate lithium ions. In the case of electrolytes without ionic liquids, the three bands at 893, 904 and 916 cm^{-1} are sharp. On the contrary in all IL-added electrolytes the intensity of the bands in the 850-950 cm^{-1} region is reduced and all peaks are broader, especially in the band at 893 cm^{-1}. Furthermore, the peak broadening is more extended in all P-series electrolytes compared to the T-series, possibly suggesting a more disordered Li^+ coordination environment. In Figures 5.8a and 5.8c, two major vibrational modes are found at 715 cm^{-1} and 740 cm^{-1}, corresponding to the C=O bending of EC and the expansion-contraction mode of the whole PF_6^- or TFSI anions, respectively. After the addition of ionic liquids for all the electrolyte solutions the band at 715 cm^{-1} decreases in relative intensity, broadens and slightly shifts to higher wave numbers. Regarding the vibrational mode at 740 cm^{-1}, in the P-electrolytes the small peak corresponding to PF_6^- anion in the EC/DMC $LiPF_6$ is completely overlapped with the strong band of the TFSI anion. On the contrary, in the T-electrolyte this peak increases in intensity and remains centered without relevant shifts. The strong band at 740 cm^{-1}, fingerprint of TFSI anion bending, is not affected by the presence of lithium salts, either LiTFSI or $LiPF_6$, nor by the length of the alkyl chain of the pyrrolydinium cation. These vibrational features suggest that Li^+ is preferentially coordinated by the C=O groups of the carbonate molecules, whereas TFSI is present as free anion. These spectral regions have been also used to perform a quantitative analysis about the coordination of Li^+ by a fitting procedure. The details of fitting procedure can be found in Materials and Methods section. Specifically, the range 850—950 cm^{-1} was deconvoluted in 4 bands, accounting the free and coordinated EC and DMC. Considering that in this region few

vibrational features due to pyrrolidinium cation are also present and according to the previous works[29], these contributions have been subtracted.

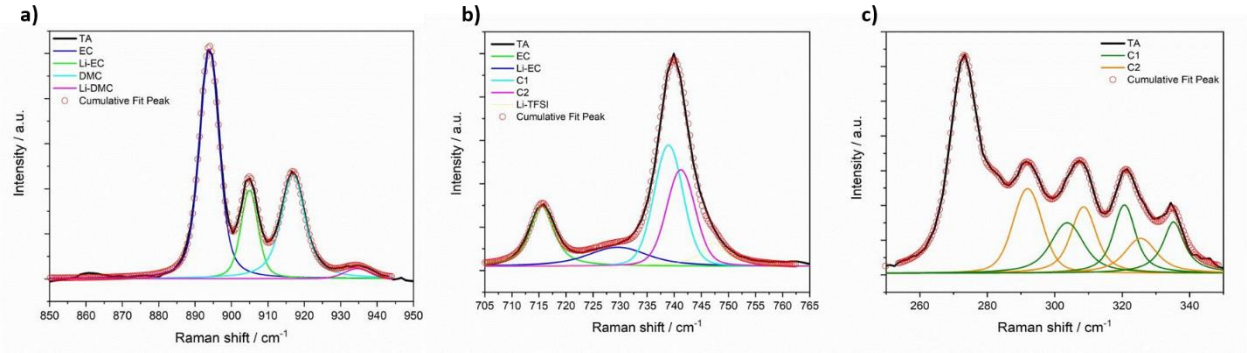

Figure 5.9: TA fitted Raman spectra of: a) between 850-950 cm^{-1} and b) between 705-765 cm^{-1}, the region of interest for the coordination of Li^+ with the carbonates; and c) between 250-350 cm^{-1}, the region used to evaluate the population ratio of the two conformers of TFSI.

In the range 705-765 cm^{-1} five bands have been included in the fitting, considering the free and coordinated EC and TFSI and the two conformers (cisoid and transoid) of TFSI[29,47]. In order to evaluate the population ratio of the two conformers of TFSI, *i.e.* cisoid and transoid, the spectral range 250-350 cm^{-1} was used. An example of these fitting is reported in figure 5.9.

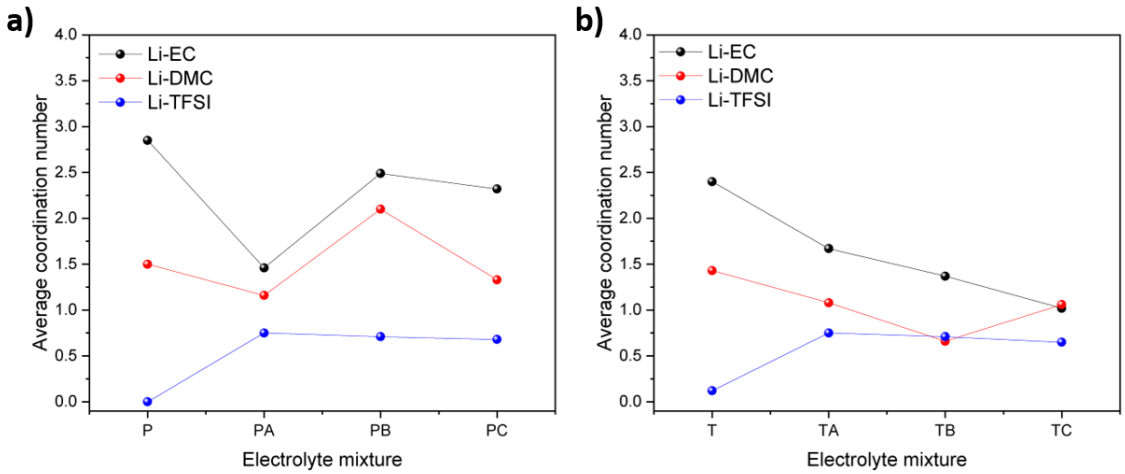

Figure 5.10: Lithium average coordination number for a)P and b)T electrolytes.

Figure 5.10 reports the quantitative analysis as average coordination number of EC, DMC and TFSI with Li^+. In the IL free P electrolyte, lithium ions are coordinated by 2.8 EC and 1.5 DMC molecules. Similar is the behavior for T, where EC and DMC coordinates 2.4 and 1.7 Li-ions,

respectively. Furthermore, TFSI anion in T electrolyte is mostly found as free anion, demonstrating a weak interaction with lithium ions. When IL is added, the interaction between TFSI anion and Li^+ is around 0.75 either for PA and TA and it is only slightly modified changing the IL. Overall T-electrolytes show a weaker lithium coordination trend with the lengthening of alkyl chain, whereas in P-electrolytes the coordination numbers appear scattered.

5.4 ELECTROCHEMICAL CHARACTERIZATION

5.4.1 Lithium half-cell analysis

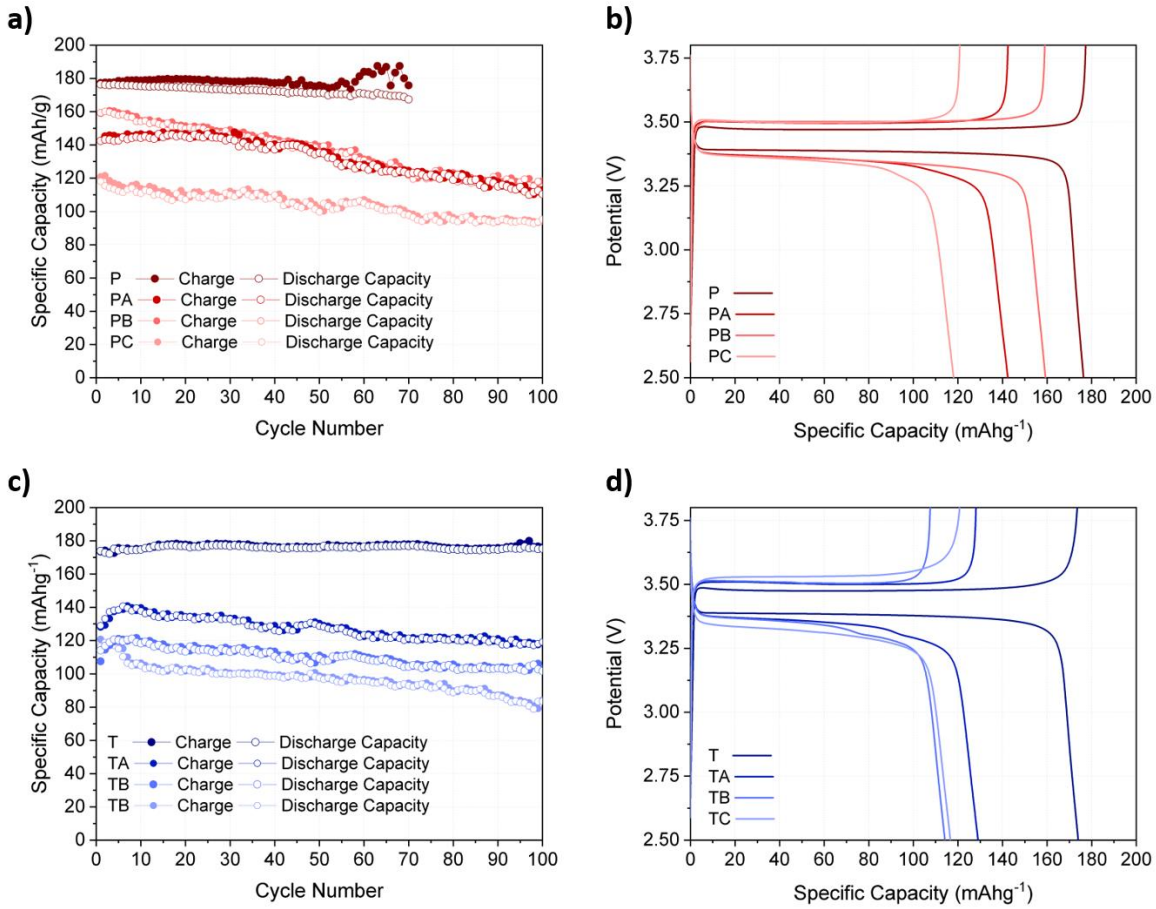

Figure 5.11: Room temperature galvanostatic charge-discharge measurements of Li/LFP cells at C/5 (1C= 170 mA g^{-1}): a) cycling performance with P-series electrolytes and b) 1st cycle voltage profile; c) cycling performance with T-series electrolytes and d) 1st cycle voltage profile.

The applicability in lithium cell of all these new electrolytes have been proved using a well-known cathode material such as $LiFePO_4$ (LFP) as shown in figure 5.11. When P is used as electrolyte, LFP shows a stable cycling along the first 60 cycles, developing a specific capacity of about 175 $mAhg^{-1}$. Nevertheless, prolonging cycling leads to failure of the cell with irreversible loss of capacity.

Despite capacity values are slightly decreased compared to the pure carbonate electrolytes, the IL solutions show good cycling stability in discharge-recharge tests and, more remarkably, the reversibility resulted improved, as demonstrated by cumulative irreversible capacity plots (see figure 5.12). In fact, while for P electrolyte after 40 cycles, a cumulative irreversible capacity of almost 120 $mAhg^{-1}$ is achieved, the latter doesn't exceed 75 $mAhg^{-1}$ when IL is added. This effect is particularly evident for the PB electrolyte, in which the Coulombic Irreversible Capacity (CIC) is less than 45 $mAhg^{-1}$ after 40 cycles. Moving to the T-series electrolytes, Figures 5.11c-d showed the electrochemical performance obtained in Li/LFP cell. The performance of LFP with T electrolyte shows a stable capacity of ≈180 $mAhg^{-1}$. Similarly to P-series electrolytes, the addition of ionic liquids leads to decrease of capacity values. However, by the analysis of the plot in Figure 5.12, cumulative irreversible capacity present further decrease in comparison to P-based electrolytes and this is particularly evident in TA and TB electrolytes, with a CIC of only 15 $mAhg^{-1}$ after 40 cycles. From the analysis reported above, PB and TB resulted the best choice to verify the applicability of these kind of IL-added electrolytes in a Li-ion cell.

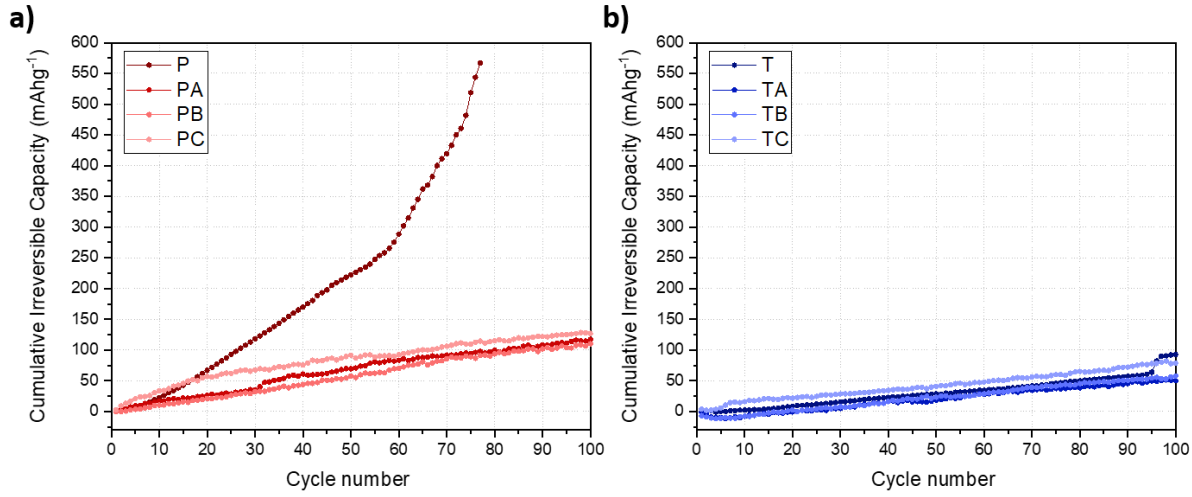

Figure 5.12: Room temperature cumulative irreversible capacities of Li/LFP cells at C/5 (1C= 170 mA g^{-1}).

Before tests in full cell, also the electrochemical behavior of Si-graphene composite[31] electrodes with PB and TB electrolytes have been evaluated and the results are reported in figure 5.13. According to the reference[31], galvanostatic discharge-recharge tests were carried out using a current density of ≈C/10 (1C=350 mAg^{-1}) in a potential range of 0.1-1 V. A formation cycle between 0.01-2V was added before any cycling to stabilize electrode-electrolyte interphase. Potential profiles of the electrodes obtained during the formation cycle are reported in Figure 5.13b-d. The performance with P and T electrolytes has been added as reference. During formation, the typical voltage profile of silicon-based anodes is visible with all the electrolytes: a long plateau below 0.1V upon discharge followed by a slope around 0.2V and a small plateau at 0.4V. With both PB and TB electrolytes, Si-graphene anode achieved more than 2000 $mAhg^{-1}$ at end of first discharge with a Coulombic efficiency of more than 80%. Upon cycling, capacity drops rapidly and after 50 cycles it is around 67% of initial capacity. Nevertheless, it should be noted that without the addition of IL, capacity drops down to 55% after 50 cycles.

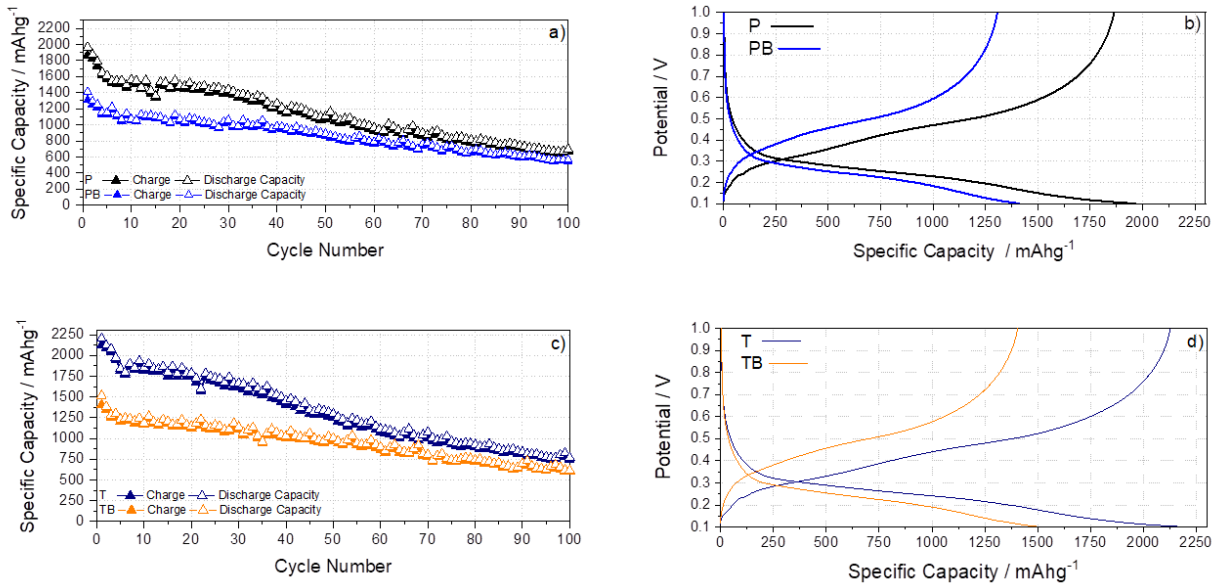

Figure 5.13: Room temperature galvanostatic charge-discharge measurements of Li/Si-graphene cells at ≈C/10 (1C= 350 mA g^{-1}): a) cycling performance with P and PB electrolytes and b) 1st cycle voltage profile; c) cycling performance with T and TB electrolytes and d) 1st cycle voltage profile.

5.4.2 Full Li-Ion proof of concept

Based on the electrochemical characterization as well as the performance in lithium cell, the electrolyte based on $Pyr_{1,5}TFSI$ resulted to be the most promising among the three ionic liquids analyzed. So, both PB and TB have been used to prove the feasibility to use this kind of electrolytes in a complete Li-ion by facing a commercial LFP cathode to a high-capacity anode such as Si-graphene composite. Overall satisfactory performance has been obtained thus confirming the applicability of the novel electrolyte blends here proposed, as you can see from the figure 5.14.

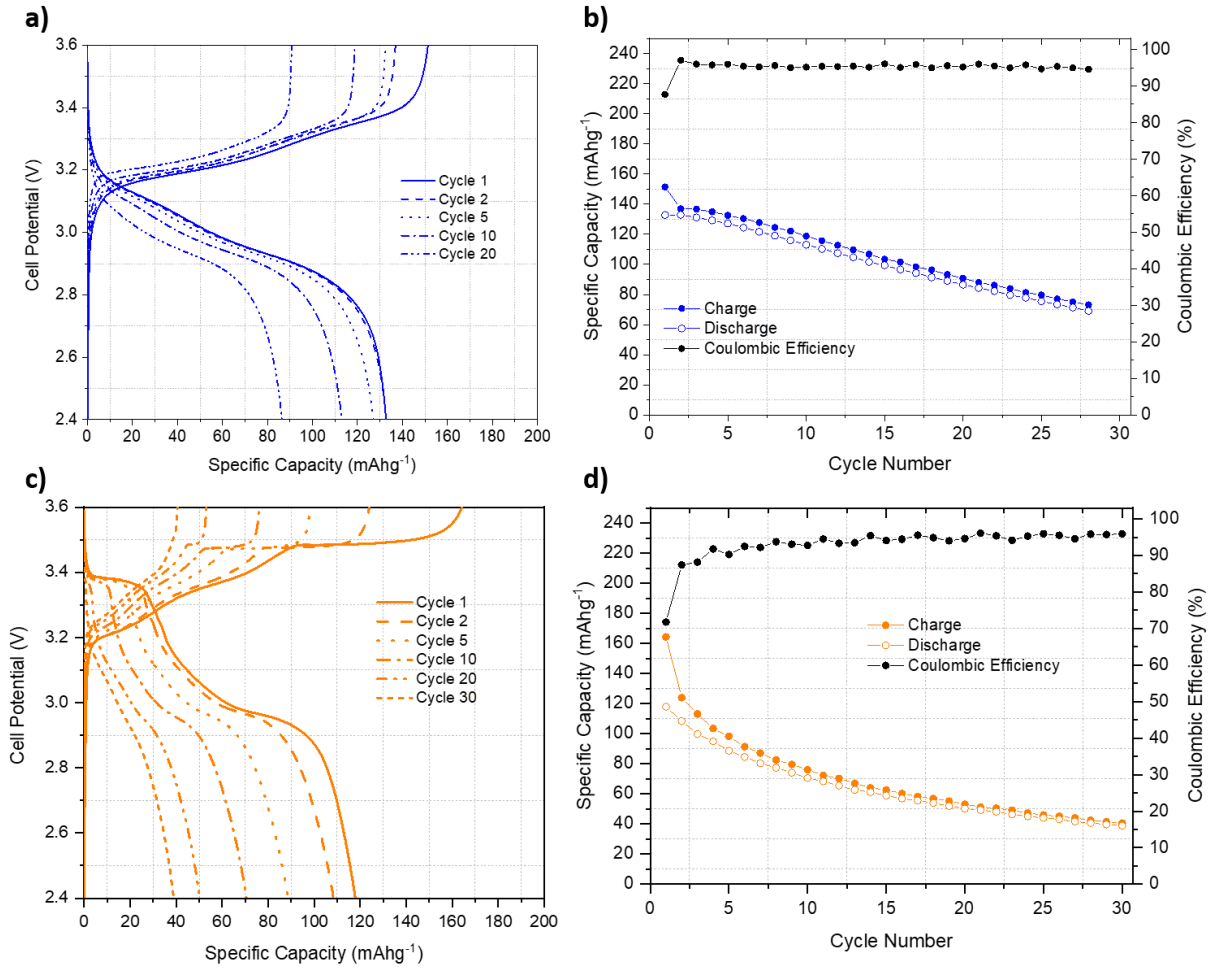

Figure 5.14: Room temperature galvanostatic charge-discharge measurements of LFP/Si-graphene cells at 100 mAg^{-1}: a) representative voltage profiles and b) cycling performance with PB electrolyte; c) representative voltage profiles and d) cycling performance with TB electrolyte.

5.5 CONCLUSION

Six different electrolytes have been prepared by adding the 50 wt.% of pyrrolidinium-based ionic liquids with 3 different alkyl chains, *i.e.* butyl- pentyl- and octyl- to 2 alkylcarbonate-based electrolytes, *i.e.* 1M $LiPF_6$ in DMC:EC (P-series) and 1M LiTFSI in DMC:EC (T-series). The influence of the length of the alkyl chain on the two series of electrolytes (*i.e.*, P and T) have been studied. The IL-added solutions proved to have higher flash points than the pristine electrolytes, that increase with the length of alkyl chain. The latter is mostly evident in the P-series electrolytes, while in the T-series only moderate difference are noticeable. In the same way, viscosity increase with the cation size, due to the higher steric hindrance of octyl- group compared to butyl-. This is in line with the values observed for ionic conductivity, where the elongation of alkyl chain affects negatively the conductivity. Nevertheless, the value remains comparable to the pure carbonate-based electrolytes. The increase of the values of viscosity and ionic conductivity with the alkyl chain do not affect the ionicity, as showed in the Walden plot. The physical-chemical properties of the six electrolytes have been related to microscopic changes in the local coordination in the liquid phase by Raman Spectroscopy. Differences in the vibrational modes, due to the pyrrolidinium cation can be detected only in the spectra of pure ionic liquids; while, in the electrolyte mixtures such vibrational modes are completely covered by the signals associated to organic solvents. By quantitative analysis, information about the average coordination number revealed that for all the electrolytes, Li^+ is coordinated mostly by EC and DMC anion; while only a small quantity, which is not influenced by the length of alkyl chain and remain constant, is coordinated by TFSI. As expected, Li^+ is coordinated preferentially by EC molecules, even though the P- and T-series electrolytes show some differences. In fact, it is evident that in the case of IL-added T-electrolytes we can observe that the Li-EC and Li-DMC coordination number decrease with the length of alkyl chain. This correlation is not obvious in the case of P-electrolytes. Probably, the presence of PF_6^- in addition to TFSI anion can influence the degree of coordination with Li-ions. From the electrochemical point of view, all the electrolytes showed an electrochemical stability window above 5V. For both series, a slight increase of electrochemical stability is visible passing from butyl to pentyl- while decrease with octyl- side chain. Also, IL added P electrolytes with shorter alkyl chain exhibited (PA and PB) enhanced properties compared to pure P as well as to T-series electrolytes. Once assembled in lithium half-cells vs. LFP, all

electrolytes supplied reversible and stable cycling: PB and PT electrolytes outperform the other formulations and have been further investigated in lithium half cells vs. silicon-graphene composite electrodes. Furthermore, both electrolytes have been tested in full Li-ion configurations (LFP/Si-Graphene) to demonstrate the applicability of these new electrolyte solutions at lab scale in complete devices.

REFERENCES

1. Kalhoff, J., Gebrekidan,], Eshetu, G., Bresser, D. & Asserini, S. Safer Electrolytes for Lithium-Ion Batteries:State of the Art and Perspectives. *ChemSusChem* **8**, 2154–2175 (2015).
2. Zhang, X., Winget, B., Doeff, M., Evans, J. W. & Devine, T. M. Corrosion of Aluminum Current Collectors in Lithium-Ion Batteries with Electrolytes Containing LiPF[sub 6]. *J. Electrochem. Soc.* **152**, B448 (2005).
3. Ue, M. & Mori, S. Mobility and Ionic Association of Lithium Salts in a Propylene Carbonate-Ethyl Methyl Carbonate Mixed Solvent. *J. Electrochem. Soc.* **142**, 2577 (1995).
4. Kawamura, T., Okada, S. & Yamaki, J. ichi. Decomposition reaction of LiPF6-based electrolytes for lithium ion cells. *J. Power Sources* **156**, 547–554 (2006).
5. Lux, S. F. *et al.* The mechanism of HF formation in $LiPF_6$ based organic carbonate electrolytes. *Electrochem. commun.* **14**, 47–50 (2012).
6. Sylla, S., Sanchez, J.-Y. & Armand, M. ELECTROCHEMICAL STUDY OF LINEAR AND CROSSLINKED POE-BASED POLYMER ELECTROLYTES. *Electrochim. Acta* **37**, 1699–1701 (1992).
7. Sharova, V. *et al.* Comparative study of imide-based Li salts as electrolyte additives for Li-ion batteries. *J. Power Sources* **375**, 43–52 (2018).
8. Aurbach, D. *et al.* Design of electrolyte solutions for Li and Li-ion batteries: A review. in *Electrochimica Acta* **50**, 247–254 (2004).
9. Xu, K. Nonaqueous liquid electrolytes for lithium-based rechargeable batteries. *Chem. Rev.* **104**, 4303–4417 (2004).
10. Lewandowski, A. & Świderska-Mocek, A. Ionic liquids as electrolytes for Li-ion batteries-An overview of electrochemical studies. *Journal of Power Sources* **194**, 601–609 (2009).
11. Galiński, M., Lewandowski, A. & Stepniak, I. Ionic liquids as electrolytes. *Electrochimica Acta* **51**, 5567–5580 (2006).
12. Agostini, M. *et al.* A high-power and fast charging Li-ion battery with outstanding cycle-life. *Sci. Rep.* **7**, (2017).
13. Agostini, M. *et al.* A mixed mechanochemical-ceramic solid-state synthesis as simple and

cost effective route to high-performance LiNi0.5Mn1.5O4 spinels. *Electrochim. Acta* **235**, 262–269 (2017).

14. Seki, S. *et al.* Lithium secondary batteries using modified-imidazolium room-temperature ionic liquid. *J. Phys. Chem. B* **110**, 10228–10230 (2006).
15. Armand, M., Endres, F., MacFarlane, D. R., Ohno, H. & Scrosati, B. Ionic-liquid materials for the electrochemical challenges of the future. *Nature Materials* **8**, 621–629 (2009).
16. Appetecchi, G. B., Scaccia, S., Tizzani, C., Alessandrini, F. & Passerini, S. Synthesis of Hydrophobic Ionic Liquids for Electrochemical Applications. *J. Electrochem. Soc.* **153**, A1685 (2006).
17. Garcia, B., Lavallée, S., Perron, G., Michot, C. & Armand, M. Room temperature molten salts as lithium battery electrolyte. *Electrochim. Acta* **49**, 4583–4588 (2004).
18. Matsumoto, H. *et al.* Fast cycling of Li/$LiCoO_2$ cell with low-viscosity ionic liquids based on bis(fluorosulfonyl)imide $[FSI]^-$. *J. Power Sources* **160**, 1308–1313 (2006).
19. Sakaebe, H., Matsumoto, H. & Tatsumi, K. Discharge-charge properties of Li/$LiCoO_2$ cell using room temperature ionic liquids (RTILs) based on quaternary ammonium cation - Effect of the structure. in *Journal of Power Sources* **146**, 693–697 (2005).
20. Xiang, H. F. *et al.* Improving electrochemical properties of room temperature ionic liquid (RTIL) based electrolyte for Li-ion batteries. *Electrochim. Acta* **55**, 5204–5209 (2010).
21. Larush, L. *et al.* On the thermal behavior of model Li-Li_xCoO_2 systems containing ionic liquids in standard electrolyte solutions. *J. Power Sources* **189**, 217–223 (2009).
22. Lalia, B. S., Yoshimoto, N., Egashira, M. & Morita, M. A mixture of triethylphosphate and ethylene carbonate as a safe additive for ionic liquid-based electrolytes of lithium ion batteries. *J. Power Sources* **195**, 7426–7431 (2010).
23. Kunze, M. *et al.* Mixtures of ionic liquids for low temperature electrolytes. in *Electrochimica Acta* **82**, 69–74 (2012).
24. Montanino, M. *et al.* Mixed organic compound-ionic liquid electrolytes for lithium battery electrolyte systems. *J. Power Sources* **269**, 608–615 (2014).
25. Guerfi, A. *et al.* Improved electrolytes for Li-ion batteries: Mixtures of ionic liquid and organic electrolyte with enhanced safety and electrochemical performance. *J. Power Sources* **195**, 845–852 (2010).
26. Quinzeni, I. *et al.* Li-doped mixtures of alkoxy-N-methylpyrrolidinium

bis(trifluoromethanesulfonyl)-imide and organic carbonates as safe liquid electrolytes for lithium batteries. *J. Power Sources* **237**, 204–209 (2013).

27. Yang, B., Li, C., Zhou, J., Liu, J. & Zhang, Q. Pyrrolidinium-based ionic liquid electrolyte with organic additive and LiTFSI for high-safety lithium-ion batteries. *Electrochim. Acta* **148**, 39–45 (2014).
28. Kim, K., Cho, Y. H. & Shin, H. C. 1-Ethyl-1-methyl piperidinium bis(trifluoromethanesulfonyl)imide as a co-solvent in Li-ion batteries. *J. Power Sources* **225**, 113–118 (2013).
29. Oldiges, K. *et al.* Understanding transport mechanisms in ionic liquid/carbonate solvent electrolyte blends. *Phys. Chem. Chem. Phys.* **20**, 16579–16591 (2018).
30. Evans, J., Vincent, C. A. & Bruce, P. G. Electrochemical measurement of transference numbers in polymer electrolytes. *Polymer (Guildf).* **28**, 2324–2328 (1987).
31. Greco, E. *et al.* Few-layer graphene improves silicon performance in Li-ion battery anodes. *J. Mater. Chem. A* **5**, 19306–19315 (2017).
32. *The European Parliament and the Council of the European Union,REGULATION (EC) No 1272/2008 OF THE EUROPEAN PARLIAMENT andOF THE COUNCIL of 16 December 2008 on Classification, Labelling andPackaging of Substances and Mixtures, Amending and RepealingDirectives 67/548/EEC and 1999/45/EC, and Amending Regulation (EC)2008*. (2008).
33. Taggougui, M., Diaw, M., Carré, B., Willmann, P. & Lemordant, D. Solvents in salt electrolyte: Benefits and possible use as electrolyte for lithium-ion battery. *Electrochim. Acta* **53**, 5496–5502 (2008).
34. Dahbi, M., Ghamouss, F., Tran-Van, F., Lemordant, D. & Anouti, M. Comparative study of EC/DMC LiTFSI and $LiPF_6$ electrolytes for electrochemical storage. *J. Power Sources* **196**, 9743–9750 (2011).
35. Tsurumaki, A., Navarra, M. A., Panero, S., Scrosati, B. & Ohno, H. N-n-Butyl-N-methylpyrrolidinium hexafluorophosphate-added electrolyte solutions and membranes for lithium-secondary batteries. *J. Power Sources* **233**, 104–109 (2013).
36. Dagousset, L., Nguyen, G. T. M., Vidal, F., Galindo, C. & Aubert, P. H. Ionic liquids and γ-butyrolactone mixtures as electrolytes for supercapacitors operating over extended temperature ranges. *RSC Adv.* **5**, 13095–13101 (2015).

37. Martinelli, A. *et al.* Phase behavior and ionic conductivity in lithium bis(trifluoromethanesulfonyl)imide-doped ionic liquids of the pyrrolidinium cation and bis(trifluoromethanesulfonyl)imide anion. *J. Phys. Chem. B* **113**, 11247–11251 (2009).
38. Diederichsen, K. M., Buss, H. G. & McCloskey, B. D. The Compensation Effect in the Vogel-Tammann-Fulcher (VTF) Equation for Polymer-Based Electrolytes. *Macromolecules* **50**, 3831–3840 (2017).
39. Xu, W., Cooper, E. I. & Angell, C. A. Ionic liquids: Ion mobilities, glass temperatures, and fragilities. *J. Phys. Chem. B* **107**, 6170–6178 (2003).
40. MacFarlane, D. R. *et al.* On the concept of ionicity in ionic liquids. *Phys. Chem. Chem. Phys.* **11**, 4962–4967 (2009).
41. Schreiner, C., Zugmann, S., Hartl, R. & Gores, H. J. Fractional walden rule for ionic liquids: Examples from recent measurements and a critique of the so-called ideal KCl line for the walden plot. *J. Chem. Eng. Data* **55**, 1784–1788 (2010).
42. Kunze, M. *et al.* New insights to self-aggregation in ionic liquid electrolytes for high-energy electrochemical devices. *Adv. Energy Mater.* **1**, 274–281 (2011).
43. Lassègues, J. C., Grondin, J., Holomb, R. & Johansson, P. Raman and ab initio study of the conformational isomerism in the 1-ethyl-3-methyl-imidazolium bis(trifluoromethanesulfonyl)imide ionic liquid. *J. Raman Spectrosc.* **38**, 551–558 (2007).
44. Castriota, M. *et al.* Raman investigation of the ionic liquid N-methyl-N-propylpyrrolidinium bis(trifluoromethanesulfonyl)imide and its mixture with LiN(SO $_2$CF$_3$)$_2$. *J. Phys. Chem. A* **109**, 92–96 (2005).
45. Paschoal, V. H., Faria, L. F. O. & Ribeiro, M. C. C. Vibrational Spectroscopy of Ionic Liquids. *Chemical Reviews* **117**, 7053–7112 (2017).
46. Martinelli, A. *et al.* Conformational evolution of TFSI- in protic and aprotic ionic liquids. *J. Raman Spectrosc.* **42**, 522–528 (2011).
47. Aguilera, L., Scheers, J. & Matic, A. Enhanced low-temperature ionic conductivity via different Li^+ solvated clusters in organic solvent/ionic liquid mixed electrolytes. *Phys. Chem. Chem. Phys.* **18**, 25458–25464 (2016).

FINAL REMARKS

One of the key challenge for the next generation of LIBs is the development of high energy and low-cost positive electrode materials. Lithium-Rich Layered Oxides (LRLOs) are currently the best option to reach this objective. Another hot topic in the field is the formulation of innovative electrolytes offering improved thermal and voltage stability.

In this work we have tacked both topics with a particular focus to develop and characterized a variety of novel LRLO.

All materials have been synthesized following a highly reproducible route: preparation parameters were optimized and controlled to optimize purity, morphology and performance. In particular, we proposed and demonstrate a new series of over-lithiated and Al-doped LRLOs with general formula $Li_{1.2+x}Mn_{0.54}Ni_{0.13}Co_{0.13-x-y}Al_yO_2$, with improved electrochemical performance and reduced cobalt content. The well-known prototypal stoichiometry $Li_{1.2}Mn_{0.54}Ni_{0.13}Co_{0.13}O_2$ has been used as a starting point and benchmark. The effect of the doping has been systematically investigated with several techniques, including XRD, SEM, TEM, XAS, RAMAN, and with different electrochemical methods.

The structure of the synthetized materials is in line with literature. From a crystallographic point of view, they show the coexistence of rhombohedral and monoclinic phases, confirming the structural ambiguity of LRLOs. We demonstrated (see chapter 2) the benefits of over-lithiation and Al doping as synergistic strategy to mitigate the cobalt content without compromises the performance. The specific capacities of the $Li_{1.2+x}Mn_{0.54}Ni_{0.13}Co_{0.13-x-y}Al_yO_2$ series are beyond 200 $mAhg^{-1}$, despite the reduction of cobalt. Moreover, the voltage decay is largely mitigated after 200 cycles along the series, suggesting a better stability during prolonged cycling.

One stoichiometry, $Li_{1.28}Mn_{0.54}Ni_{0.13}Co_{0.02}Al_{0.03}O_2$, has shown outstanding performance. To further investigate the sample, additional experiments at a synchrotron radiation beamline facility, were carried out. Apparently, the co-doping with Li and Al lead to the formation of extended oxygen vacancies and has a direct impact on the electronic structure and disorder. Moreover, post-mortem analysis confirmed the enhancement of structural stability upon cycling in lithium half-cells: both synchrotron X-Ray diffraction and Raman spectroscopy showed a better structural

retention after 100 cycles. The layered structure is better maintained in the doped material compared the benchmark Co-rich both in the bulk and in the surface.

Additionally, the over-lithiation has been used in combination with Mn doping to obtain a Co-free material, $Li_{1.25}Mn_{0.625}Ni_{0.125}O_2$. The material has a layered structure as confirmed by XRD and Raman and very promising electrochemical performance. It can supply an excellent electrochemical performance either at low and high currents (230 $mAhg^{-1}$ at C/10 and 118 $mAhg^{-1}$ at 2C). Post-mortem analysis showed minor structural rearrangements and remarkable morphological retention. The novelty of this thesis work lies in the demonstration of a novel strategy to replace the cobalt into LRLO without hindering the electrochemical performance and the realization, for the first time to the best of our knowledge, of over-lithiated materials combined with Al and Mn co-doping. Their remarkable electrochemical performance, described in the chapter 2, roots in the improved structural resilience upon cycling compared to $Li_{1.2}Mn_{0.54}Ni_{0.13}Co_{0.13}O_2$.

Some additional insights into the structure of LRLOs represents another innovative achievement of this work. Differently from stoichiometric layered materials, LRLOs can be indexed with both R-3m and C2/m unit cells with possible superstructures, stacking defects and anti-sites. In this work, we demonstrated that both the above structures are not able to describe all features of collected pattern. Different approaches were used to push the description beyond the state of the art. Supercells approach showed improvements in the convergences of Rietveld refinement, in particular with a structure named R_C_3b. This unit cell has a monoclinic structure where the *b* parameter is 3 times bigger than the conventional structure. It is able to fit better both Neutron and XRD patterns compared to the classical R-3m, C2/m and C2/m with Li-TM mixing. However, the region of superstructure XRD peaks is still poorly described. To push further our analysis, the simulation of stacking faults within the material was considered. The FAULTS software allowed us to refine the degree of stacking faults leading to an improvement in the XRD refinement of superstructure region. Furthermore, the explicit modelling of the Li-TM mixing defects in the TM layers led to additional improvement in the structural refinement. Our work showed that supercells and defects are important elements in the description of the pristine structures.

Finally, the last part of this thesis tackled the study of novel electrolytes that can be used with high-voltage cathode materials. LRLOs work in very large potential windows, between 2 and 4.8V. The standard electrolytes, based on organic solvent, are not completely stable at this high potential. Therefore, we investigated several electrolytes blends with different ionic liquids and lithium salts. In particular, pyrrolidinium-based ionic liquids with 3 different alkyl chains, *i.e.* butyl- pentyl- and octyl- to 2 alkylcarbonate have been used, as well as two different salts, *i.e.* $LiPF_6$ and LiTFSI.
All electrolytes have been analyzed in terms of physical-chemical properties, such as flash point, viscosity, ionic conductivity and Raman Spectroscopy. Moreover, the electrochemical stability has been investigated with the use of linear sweep voltammetry and cyclic voltammetry. The best electrolyte formulations have been successfully used in full cell device with a Silicon-graphene composite as the negative counterpart.

Future perspectives will concern the optimization of the electrode technology, *i.e.* different synthetic routes, surface coating and the electrolytes. A more scalable process is the crucial objective in order to obtain an electrode material easily and at low price. Moreover, the choice of a particular synthesis can lead to an optimized morphology and have an impact on the electrochemical performance. Instead, the surface coating can help to improve the stability cycling and the conductivity of the material. Regarding the electrolytes, future works will be devoted to the study of the applicability of the electrolytes reported in the chapter 5 with the over-lithiated materials of the chapter 2.